

# **A COMPUTATIONAL APPROACH TO CURTAIN COATING**

A.A. Jansen  
July 10, 1997  
Avery Dennison

**Mentors:**

Drs. B.R. Potjer (Avery Dennison)  
Dr. J. Derksen(TU Delft)

**Avery Dennison**

Lammenschansweg 140

2321 JX Leiden

Tel: +(31) 71 5793309

Fax: +(31) 71 5793407

E-mail: JansenAlexander@AveryDennison.com



## Summary

In curtain coating, a falling liquid film impinges on a substrate that traverses underneath. In this thesis the flow in the area of impact, the so-called impingement zone, was investigated using the commercially available code NEKTON -Release 3.0-. The computational method used in this code is the spectral-element method and belongs to the class of variational methods. Since the flow is bounded by free surfaces, not only velocity and pressure have to be calculated but also the nodal position. Therefore, the following strategy has been implemented in NEKTON: the free surface boundary is fixed and the flow field is solved until convergence; then the geometry is updated. These steps are repeated till convergence.

The simulations in this thesis cover two areas:

- the influence of numerical parameters on the accuracy of the solution: the direct and iterative solvers in NEKTON were compared with regard to consistency, the polynomial order of the basis functions in the spectral-element method has been increased, and, finally, the grid in the heel zone has been refined.
- the influence of physical parameters, such as web speed and dynamic contact angle, on the flow field. The outcome is compared to theoretical models found in the literature.

Simulations have been complemented by experimental work covering four different areas. First, characterisation of the coating fluid; the data obtained has been used as input to the simulations. Second, both static as well as dynamic off-line experiments have been done to get a feel for the process and to study the achievable coating window. Third, results obtained in the off-line set-up have been verified with pilot coater experiments, to judge their consistency. Finally, the design of the edge guides, needed to maintain the curtain at full width, and related edge effects have been studied more closely.



---

## Conclusions & Recommendations

### *Conclusions*

Analysis of curtain coating by dividing the flow into seven zones makes it possible to model parts of the flow domain rather than the entire domain, thus reducing computational time and difficulty. The seven zones can be sub-divided into two types of zones: so-called forming zones, where the flow rearranges very quickly and upstream influence, through capillary pressure and normal viscous stress, is abundant; and flow-developing zones, where the flow is close to/or fully developed and the liquid undergoes predominantly shearing or extensional deformation. The latter regimes are much simpler types of flow, which are easily solved analytically.

The forming zones, however, can only be solved realistically by using numerical techniques. In curtain coating, details of flow in the film-forming zone and in the sheet-forming zone significantly affect uniformity of the coated layers, while flow in the impingement zone to a large degree affects the range of process operation conditions.

When comparing the relative wetting line position to Blake's theoretical predictions, the same trend is observed as in the simulations.

Comparison of simulation results as to the relative wetting line position, with a theoretical model by Blake et al, which take into account surface tension effects, showed the same trend for varying coating speed. There is, however, a large discrepancy between the simulations and the theoretical predictions. There are several possible reasons for this difference: the constants in Blake's model are dependent on the similarity velocity profile chosen and may vary by as much as 30%. Furthermore, the solution was shown to be grid dependent.

If, however, submicroscopic details near the dynamic contact point need to be resolved,  $O(< 0.01 \mu\text{m})$ , the governing equations and boundary conditions should be adapted to account for the physics at these small length scales which no longer fall in the domain of continuum theory.

Investigation into the consistency of the solvers showed that, for the simulations done here, the direct and the iterative solver yield the same solution. According to NEKTON, this will be the case as long as the aspect ratio of the elements does not exceed 50:1.

Variation of the polynomial order showed changes in the solution, but only within the bounds of the initial grid. When more detail is required, the grid should be refined. Excessive grid refinement does not lead to mathematically incorrect solutions, but it may not give insight into microscopic mechanisms either, since continuum theory does not apply at these levels.

The predicted pressure distribution on the web turned out to be very low; hence, paper used with curtain coating can be more porous than with e.g., slot coating.



### *Recommendations*

In future, work simulations of the impingement zone should be extended to find a more complete coating window: liquid properties should be varied as well. The 2-D simulations may also be coupled with air flow. Furthermore, simulations on curtain coating should be extended to 3D situations.

Experiments should focus on the angle of web inclination, which is said to have a positive influence on coatability, though theory suggests otherwise, and on better control of edge effects.



---

## Table of Contents

Summary .....	I
Conclusions & Recommendations .....	II
1. Introduction .....	1
2. Mathematical Description of Fluid Flow .....	4
2.1 Conservation Equations .....	4
2.1.1 Conservation of Mass.....	4
2.1.2 Conservation of Momentum .....	4
2.1.3 Dimensionless Formulation .....	6
2.2 Boundary Conditions.....	6
2.2.1 The Kinematic Boundary Condition .....	6
2.2.2 The No-slip Condition .....	7
2.2.3 The Slip Condition .....	7
2.2.4 The Dynamic Boundary Condition .....	8
2.2.5 Contact Angles & Lines .....	9
2.2.6 Inlet & Outflow Boundary Conditions.....	10
3. Dynamic Wetting Parameters.....	11
3.1 The Contact Angle .....	11
3.1.1 Experimental Methods .....	11
3.1.2 Theories.....	12
3.1.3 Empirical Correlations .....	14
3.2 Slip .....	14
4. Numerics .....	16
4.1 Discretisation.....	16
4.1.1 v-p formulation.....	16
4.1.2 Imposition of Boundary Conditions .....	18
4.2 Mesh Generation .....	18
4.3 Iteration Procedures.....	19
4.3.1 Solution of Linear Equations .....	19
4.3.2 Picard Iteration .....	19
4.3.3 Newton Iteration.....	21
4.3.4 Convergence Criteria.....	22
4.3.5 Contact Angles & Slip .....	22



---

5. Division of the Flow into Seven Zones.....	24
5.1 Feed Zone.....	24
5.2 Film-forming Zone.....	25
5.3 Film-flow Zone.....	26
5.4 Sheet-forming Zone.....	27
5.4.1 Purely Hydrodynamic Deflection - Pinned Contact Line.....	28
5.4.2 Contact Angle Hysteresis - Migrating Contact Line.....	28
5.4.3 Hydrodynamic Hysteresis.....	29
5.5 Curtain-flow Zone.....	30
5.6 Impingement Zone.....	30
5.6.1 Boundary Layer Analysis of the Impingement Flow.....	31
5.7 Take-away Zone.....	33
6. Operability - Coating Window.....	34
7. Area to be Investigated Through Simulations.....	36
7.1 General Simulation Conditions.....	36
7.2 Parameter Studies Of the Curtain Coating Process.....	43
7.3 Effect of Imposed Dynamic Contact Angle.....	46
7.4 Comparison of the Solvers.....	46
7.5 Increasing the Polynomial Order.....	47
7.6 Grid Refinement.....	47
7.7 Pressure Distribution.....	47
7.8 Figures.....	49
8. Experimental Study of Curtain Coating.....	56
8.1 Fluid Characterisation.....	56
8.2 Off-line Experiments.....	58
8.2.1 Static Off-line Set-up.....	58
8.2.2 Dynamic Off-line Set-up.....	60
8.3 Pilot Experiments.....	62
8.4 Edge Guiding.....	65
9. Nomenclature.....	66
10. References.....	69



## 1. Introduction

### *History*

To coat means to displace from a solid surface one fluid, typically air, by another, often liquid, in order to deposit a continuous uniform film that can be maintained until dried, solidified, or transferred. There are various methods of creating a coherent film: a liquid phase can displace a gas phase either continuously by dynamic wetting or as a spray by wetting, spreading and coalescence; a continuous vapour phase can displace gas by condensation; and a solid phase as a powder can displace gas by attachment, softening, spreading and fusion. Coating operations are essential process steps in the manufacture of paper and allied products, photosensitive films, magnetic tapes and various other products. Owing to competition and technological advance, the current trends in the coating industry include higher coating speeds, thinner films, more stringent uniformity requirements, more complex functional components in coated layers, and multi-layered coatings. In this thesis a coating technique called curtain coating, which incorporates above mentioned trends, is investigated.

In curtain coating, a liquid film formed on an inclined slide, as shown in figure 1.1, or extruded through a narrow vertical slit, falls as an unsupported sheet under the action of gravity onto a moving substrate being coated. The zone where the curtain impacts on the substrate is called the impingement zone.

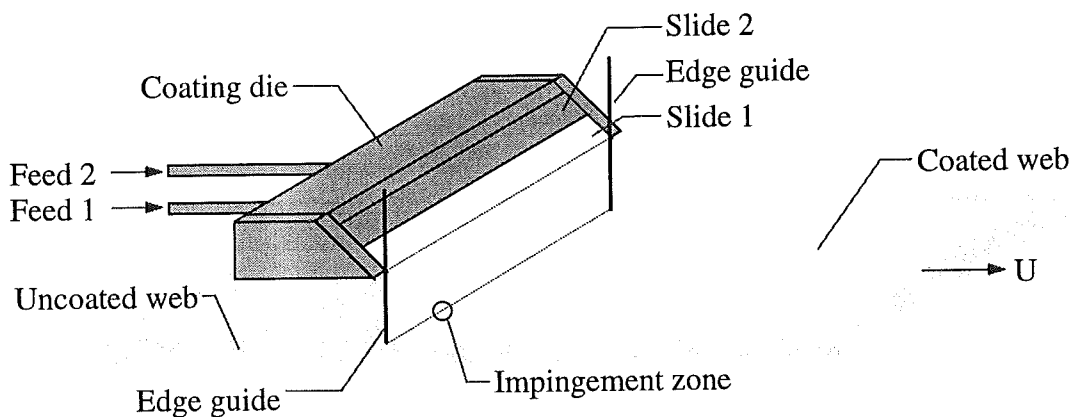


Figure 1.1: Schematic of a slide curtain coater for two layer coating.

So-called edge guides, preferably made out of a wettable material, are needed to maintain a specific width of the falling curtain. Without edge-guides the curtain tends to neck-in, surface tension concentrates liquid into edges of roughly cylindrical shape that fall toward each other and so produce a liquid sheet that is far from being uniform (figure 1.2).

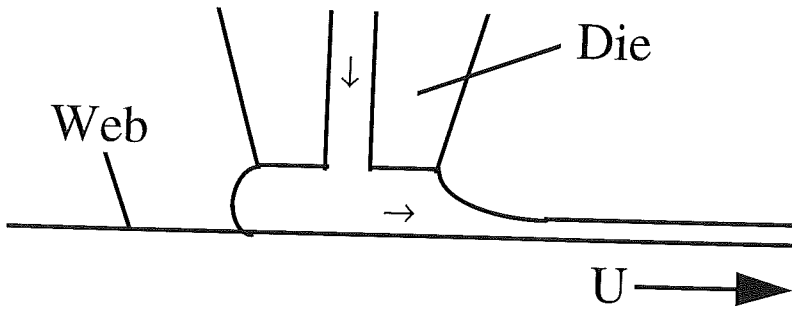


Figure 1.3: Extrusion coating.

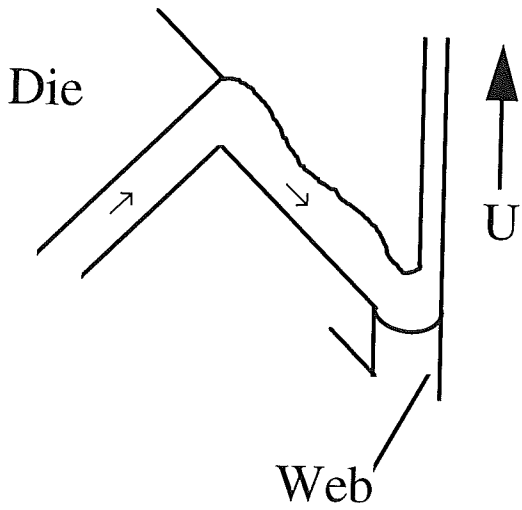


Figure 1.4: Slide coating

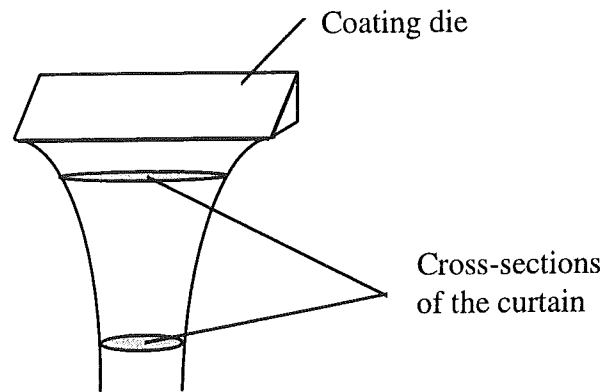


Figure 1.2: Curtain neck-in when no edge guides are applied.

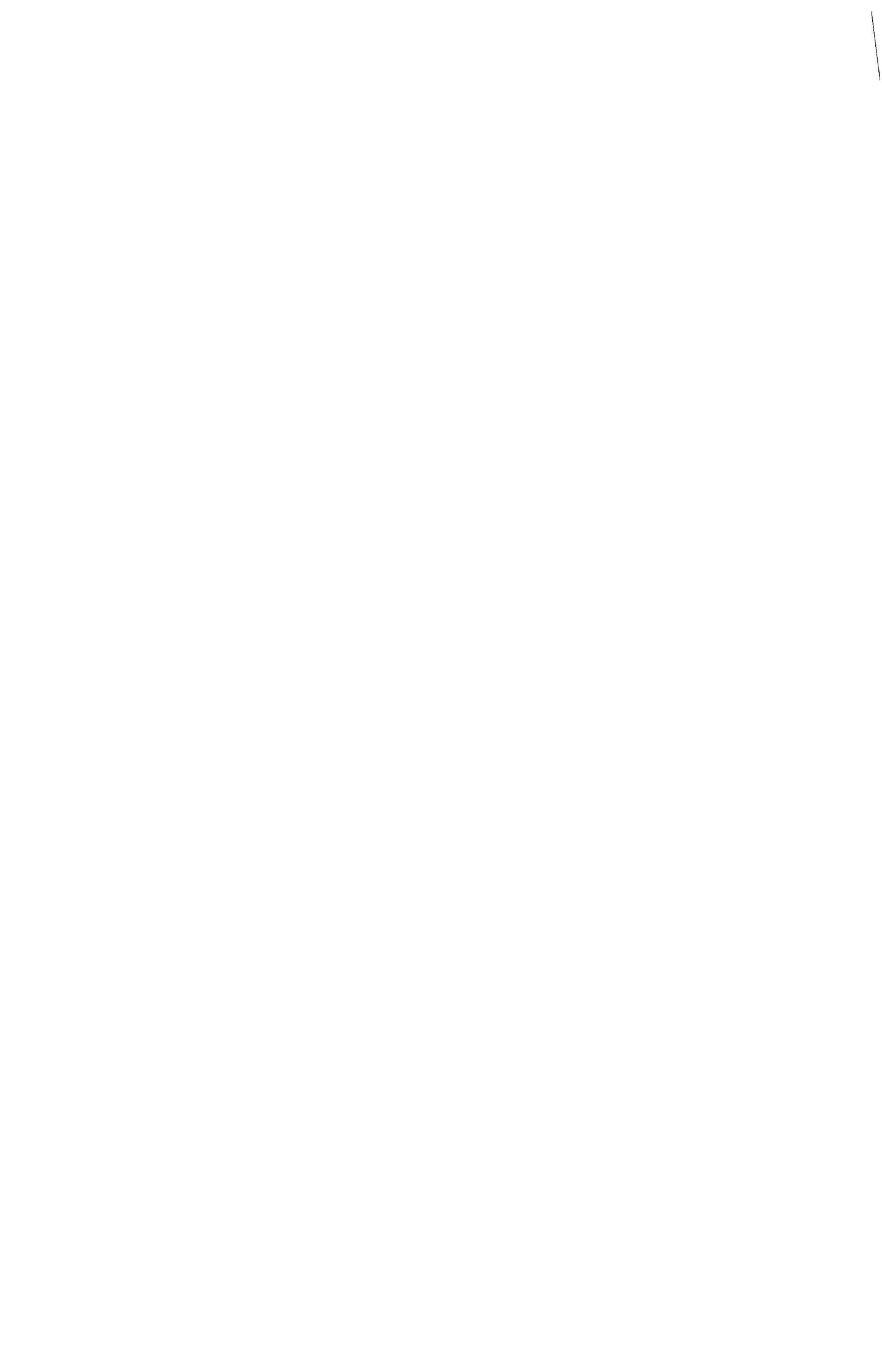
Curtain coating has long been used to deposit comparatively crude coatings such as wax melts and protective polymer packaging materials (Willis, 1962) as well as lacquer solutions on sheet metal and furniture boards (Kinzelmann, 1965). Over a decade ago, however, curtain coating emerged as a technology for high-precision coating of thin layers at high speeds (Hughes 1970, Greiller 1972).

Operating conditions representative of those in the photographic industry are listed in table 1.1.

Table 1.1: Typical coating conditions used in the photographic industry (Greiller, 1972).

Viscosity of coating compositions	5-200 mPa·s
Surface tension of coating compositions	0.02-0.06 N/m
Wet thickness of applied film	10-150 $\mu\text{m}$
Tolerated thickness variation	1-5 %
Height of free falling curtain	50-500 mm
Coating width	1-3 m
Substrate speed	up to 10 m/s

In comparison to other coating operations, in particular bead-coating methods such as extrusion coating (figure 1.3) and slide coating (figure 1.4), curtain coating has some distinct advantages beyond the higher speeds it brings. Because there is no narrow clearance between coating die and moving substrate, precise mechanical alignment is not critical, film uniformity is less sensitive to variations in substrate thickness, splices in the substrate can pass freely, and particles or bubbles cannot get trapped as easily. The curtain coating method permits coating to the edge of the substrate, thereby reducing the amount of scrap; it is readily adapted to multi-layer coating; it is suitable for coating both discrete sheets as well as continuous substrates; and finally opens the possibility to coat porous substrates, because of the low pressure in the impingement zone,  $O(0.1 \text{ bar})$ , compared to bead-coating,  $O(1 \text{ bar})$ .



## *Simulations*

In the quest to identify the mechanisms by which defects form or coating processes fail, scientifically designed experiments are indispensable, for they are the ultimate test for any hypothesis or theory. Experiments alone, however, often fail to elucidate fully cause-and-effect relationships. Furthermore they can be very costly.

Computer-aided analysis can explain many hydrodynamic mechanisms that control the outcome of coating processes; suggest design of process and product for improved coatability; visualise details of the flow field that are inaccessible to the experimentalist due to geometric constraints or non-transparent liquids; evaluate many more configurations than could realistically be tested in experiments, thereby saving cost and time; and permit exploration of parameter ranges that may be inaccessible with existing pilot equipment.

## *Objectives*

In this thesis the different flow zones in curtain coating are identified and analysed. The analysis can be exact for simple flows, such as the fully developed flow in the feed-slot; for so-called forming zones, however, where the flow undergoes rapid changes, numerical, two-dimensional, steady state simulations are required.

The impingement zone is the determining zone for process operability and is therefore the focus of the simulations presented in this thesis. Using the commercially available code NEKTON -Release 3.0- the influence of physical parameters, such as web speed and dynamic contact angle, on the flow field is investigated. The outcome is compared to models and correlations found in literature. Next to purely physical parameters, the influence of numerical parameters on the accuracy of the solution is studied: the direct and iterative solvers are compared, the polynomial order of the basis functions is increased and finally the grid in the heel zone is refined.

As a complement of the simulations experimental work is done covering four different areas. First, the coating fluid is characterised; the obtained data is used as an input in the simulations. Second, both static as well as dynamic off-line experiments are done to study the so-called teapot effect and to determine the minimal flow rate per meter die width required to maintain a stable curtain. Third, results obtained from the off-line set-up are verified with pilot coater experiments. Finally the design of the edge guides and related edge effects are studied more closely.

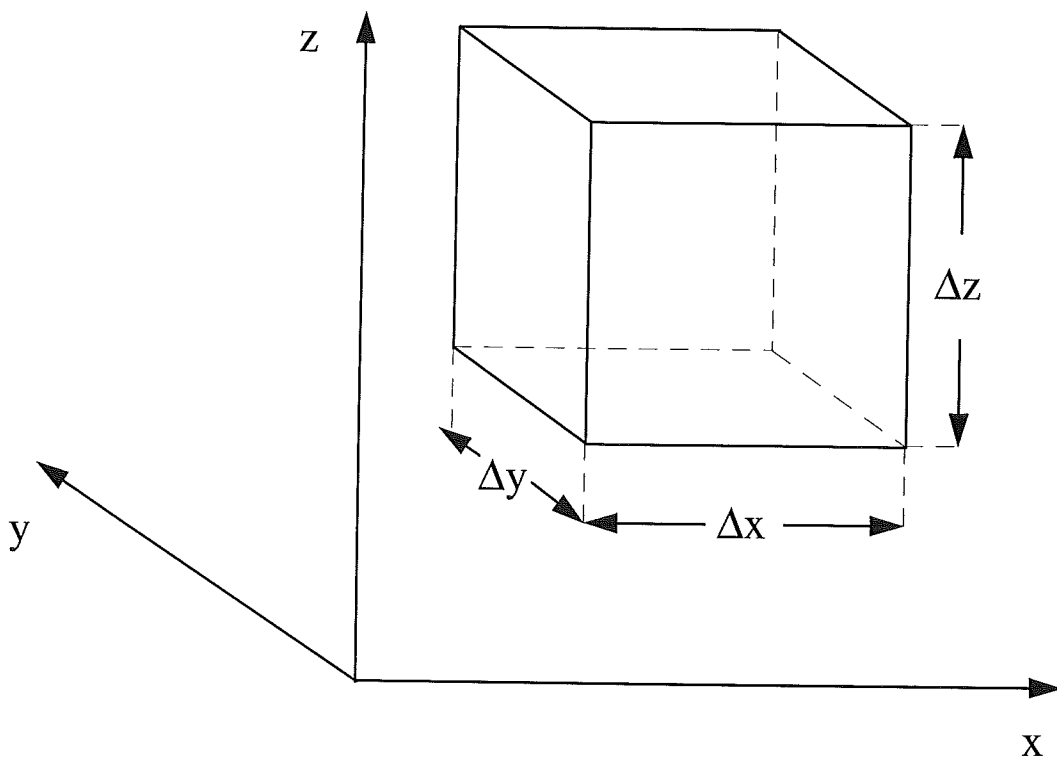


Figure 2.1: Stationary volume element through which a fluid is flowing.

## 2. Mathematical Description of Fluid Flow

In this chapter, the underlying physics of fluid flow is discussed, and the associated governing equations and boundary conditions are presented.

### 2.1 Conservation Equations

Before considering the conservation laws which govern fluid flow, it is necessary to dwell on the fact that fluid mechanics provides a macroscopic description of fluid motion. Once the length scale of a flow field is reduced to approximately ten times the distance between the molecules comprising a material, the appropriateness of modelling the material as a continuum is in question. The smallest 'body' of fluid which can be envisioned, but still within the constraints of a macroscopic continuum, is called a fluid point (Weinstein, 1997). The equations of fluid mechanics govern the motion of fluid points.

#### 2.1.1 Conservation of Mass

This equation is derived by writing a mass balance over a *stationary* volume element through which the fluid is flowing (figure 2.1). After rewriting into vector form the following equation is found (Bird, 1960):

$$\frac{D\rho}{Dt} + \rho \nabla \cdot \mathbf{v} = 0$$

2.1

where  $\rho$  is the fluid density,  $\mathbf{v}$  is the velocity vector and  $t$  is time. Equation 2.1 is commonly referred to as the continuity equation.

For coating flows, the density of the fluids involved can be considered to be constant (incompressible fluid). In this case equation 2.1 reduces to:

$$\nabla \cdot \mathbf{v} = 0$$

2.2

#### 2.1.2 Conservation of Momentum

Conservation of mass places one constraint on fluid motion, but to achieve flow there must be some driving force. The relation between applied force and fluid flow is described by Newton's second law of motion, which states that the rate of change of the momentum of a body,  $\mathbf{L}$ , is equal to the net force on the body,  $\mathbf{F}_{\text{net}}$ .

$$\frac{d\mathbf{L}}{dt} = \mathbf{F}_{\text{net}}$$

2.3



Setting up a momentum balance over the volume element in figure 2.1 therefore yields (Bird, 1960):

$$\rho \frac{D\mathbf{v}}{Dt} = -\nabla p - \nabla \cdot \boldsymbol{\tau} + \rho \mathbf{g}$$
2.4

here  $p$  denotes the pressure,  $\boldsymbol{\tau}$  the stress tensor and  $\mathbf{g}$  the gravitational acceleration vector.

In order to use the above equation, it is necessary to relate the stress tensor  $\boldsymbol{\tau}$  to the type of fluid and its motion. Such a relationship is called a *constitutive* relation. The starting point for most of the analytical as well as numerical calculations to be discussed later will be the linear viscous, or Newtonian, fluid model for which (Pearson, 1983):

$$\boldsymbol{\tau} = \frac{2}{3} \eta (\nabla \cdot \mathbf{v}) \mathbf{I} - 2\eta \mathbf{D}$$
2.5

where  $\eta$  is the dynamic viscosity,  $\mathbf{I}$  the unit tensor and  $\mathbf{D}$ , the 'rate of deformation tensor', which is given as:

$$\mathbf{D} = \frac{1}{2} [\nabla \mathbf{v} + (\nabla \mathbf{v})^T]$$
2.6

When substituted into equation 2.4, assuming incompressibility of the fluid, this yields the Navier-Stokes equations:

$$\rho \frac{D\mathbf{v}}{Dt} = -\nabla p + \eta \nabla^2 \mathbf{v} + \rho \mathbf{g}$$
2.7

The Newtonian model might, however, not be a satisfactory description of the coated fluid. In most cases the viscosity itself is dependent on the magnitude of the local rate of strain. A simple model frequently used for describing these types of fluids is the so called Ostwald-de Waele model (Pearson, 1983):

$$\boldsymbol{\tau} = -2 \left[ K |2(\mathbf{D}:\mathbf{D})|^{\frac{n-1}{2}} \right] \mathbf{D}$$
2.8

where  $K$  is the consistency and  $n$  the power-law index.

An equally important characteristic is that of elasticity, whereby part of the deformation of the fluid is reversible, and the work done by the deforming stress is stored as elastic (recoverable) energy. This last case however, is not considered in this thesis; neither are temperature effects taken into account.



### 2.1.3 Dimensionless Formulation

It is often convenient to express the conservation equations in dimensionless form. For this a characteristic length scale,  $L$ , and velocity,  $U$ , are required. A characteristic length scale of the flow is e.g. the final thickness of the coating,  $\delta_{co}$ ; a characteristic velocity of the flow is e.g. coating speed. Both pressure and stress are measured in units of  $\eta U/L$ , where  $\eta$  is the viscosity of the fluid. For steady coating flows considered in this thesis equation 2.4 reduces to:

$$\text{Re } \mathbf{v}^* \cdot \nabla^* \cdot \mathbf{v}^* = -\nabla^* p^* - \nabla^* \cdot \boldsymbol{\tau}^* + \text{St } \mathbf{f} \quad 2.9$$

where  $\mathbf{f}$  is a unit vector in the direction of the gravitational force.

Two dimensionless groups can be identified in equation 2.9, the Reynolds number,  $\text{Re}$ , and the Stokes number,  $\text{St}$ .  $\text{Re}$  and  $\text{St}$  measure the relative importance to viscous force of inertia and gravity respectively. They are defined in table 2.1.

Table 2.1: Dimensionless groups measuring ratios of competing forces in coating flows.

Dimensionless Group	Definition	Ratio of
Reynolds Number	$\text{Re} \equiv \frac{\rho U L}{\eta}$	$\frac{\text{Inertial force}}{\text{Viscous force}}$
Stokes Number	$\text{St} \equiv \frac{\rho g L^2}{\eta U}$	$\frac{\text{Gravity force}}{\text{Viscous force}}$
Capillary Number	$\text{Ca} \equiv \frac{\eta U}{\sigma}$	$\frac{\text{Viscous force}}{\text{Surface tension forces}}$
Weber Number	$\text{We} \equiv \frac{\rho L U^2}{\sigma}$	$\frac{\text{Surface tension forces}}{\text{Inertial force}}$

## 2.2 Boundary Conditions

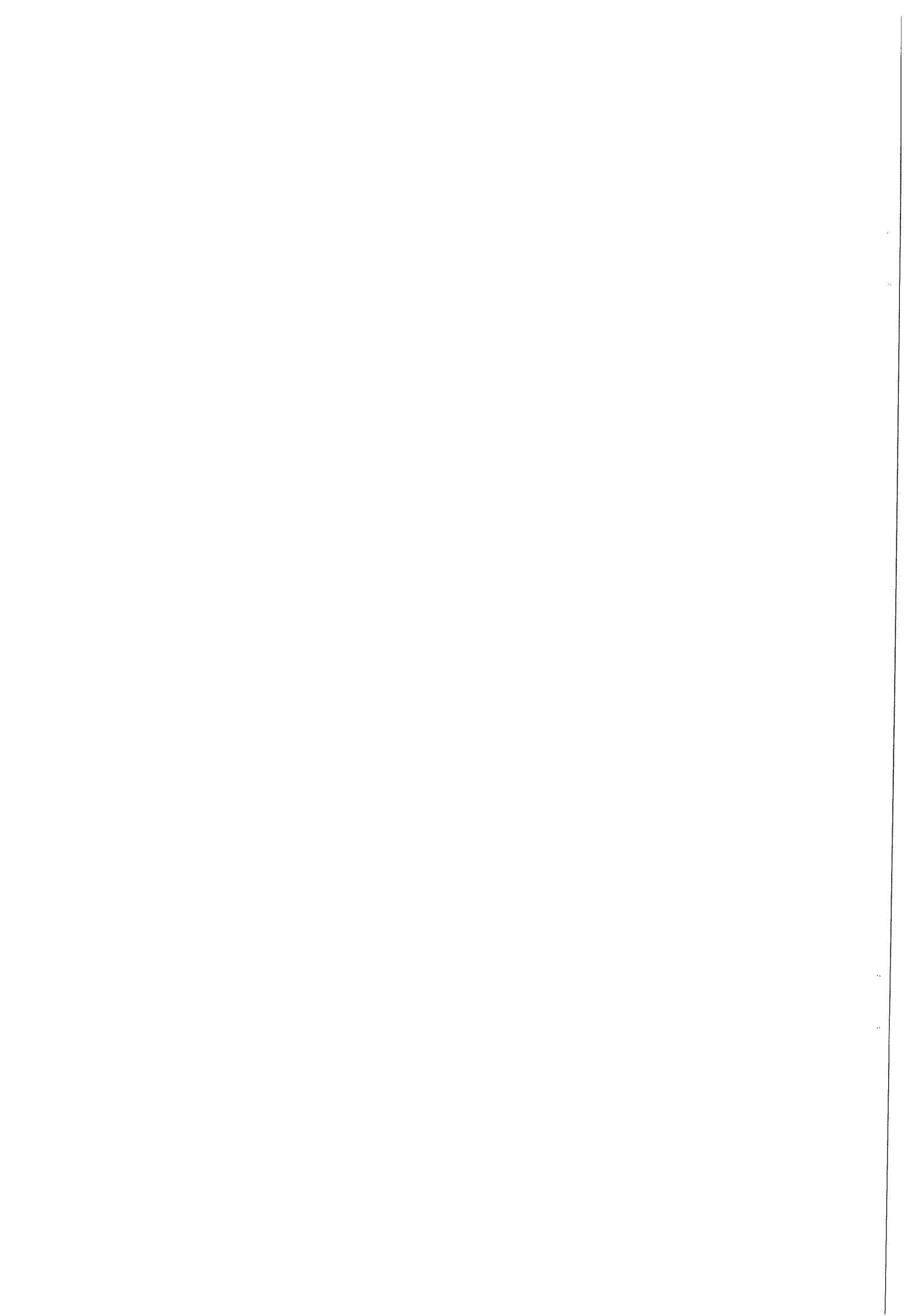
The boundary conditions introduce the physical information necessary to uniquely solve the governing equations of fluid dynamics. In what follows the boundary conditions applicable to coating flows are considered.

### 2.2.1 The Kinematic Boundary Condition

The kinematic boundary condition provides a constraint on fluid flow such that conservation of mass is satisfied across the boundaries of the flow domain. In this thesis the boundaries are considered impermeable, i.e. there is no mass transfer across a fluid/solid or a fluid/fluid interface, e.g. a free surface:

$$\mathbf{n}_i \cdot \mathbf{v}_i = 0 \quad 2.10$$

where  $\mathbf{n}_i$  is the outward unit normal of phase  $i$  to the interface.



## 2.2.2 The No-slip Condition

There is also a need to constrain the motion of fluid points in each phase along an interface. A widely used assumption in viscous flows is that the tangential component of velocity is continuous across bounding surfaces; this assumption is applied to both solid surfaces and fluids alike (Stokes, 1851):

$$\mathbf{v}_1 \cdot \mathbf{t} = \mathbf{v}_2 \cdot \mathbf{t} \quad 2.11$$

where  $\mathbf{t}$  is a unit tangent to the interface.

At an interface equations 2.10 and 2.11 together therefore necessitate that the velocities on either side be the same.

## 2.2.3 The Slip Condition

In the neighbourhood of contact lines (discussed below), however, where fluid interfaces intersect solid boundaries (figure 2.2) conventional fluid mechanical analysis, based on the no-slip hypothesis, indicates that stresses would become indefinitely high (Huh and Scriven, 1971).

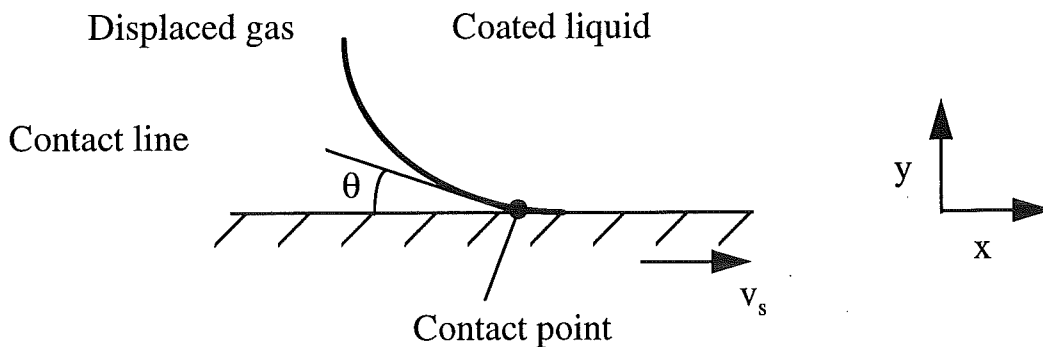


Figure 2.2: The intersection of two fluids and a solid surface in the dynamic contact point.

Currently the method of choice for avoiding this apparent stress singularity, which is physically inadmissible, is to replace the no-slip condition near the contact line with some type of slip condition (Silliman and Scriven, 1980). A simple expedient is to specify (or to allow to enter through discretisation) a slip velocity distribution of the form:

$$\mathbf{v} - \mathbf{v}_s = f(\mathbf{x})(\mathbf{v}_c - \mathbf{v}_s) \quad 2.12$$

where  $\mathbf{v}_s$  is the velocity of the solid boundary,  $\mathbf{v}_c$  the velocity of the contact line, which is mostly set equal to  $\mathbf{0}$  and  $\mathbf{v}$  is the velocity at some point  $\mathbf{x}$ .

In case of two dimensional flow,  $f(x)$  is a function of the distance,  $x$ , measured from the contact line along the solid surface so that:

$$0 \leq f(x) \leq 1 \quad \forall 0 \leq x \leq \Delta x$$

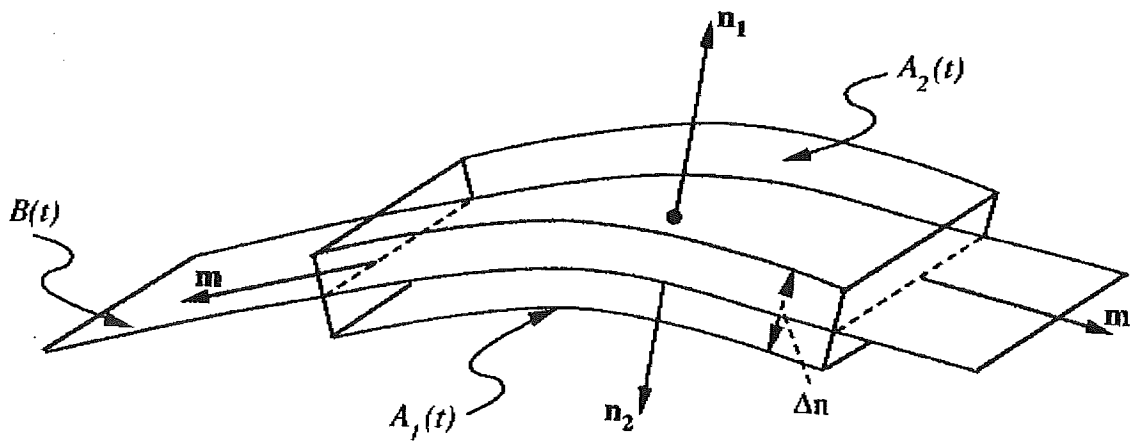


Figure 2.3: Material body used to derive the dynamic boundary condition.

Here  $\Delta x$  is the distance over which the liquid is allowed to slip. Physically more plausible however is Navier's boundary condition, which makes the flux of tangential momentum normal to the wall proportional to the velocity discontinuity (Navier, 1827):

$$\beta^{-1} \mathbf{t}_s \cdot (\mathbf{v} - \mathbf{v}_s) = \mathbf{t}_s \mathbf{n}_s : \mathbf{T} \quad 2.13$$

where  $\beta$  is the slip coefficient,  $\mathbf{t}_s$  and  $\mathbf{n}_s$  are the unit tangent and normal to the solid surface and  $\mathbf{T}$ , the total stress tensor, which is given as:

$$\mathbf{T} = -p \mathbf{I} - \boldsymbol{\tau} \quad 2.14$$

Both types of slip conditions involve a length parameter, e.g.  $\beta\eta$ , that measures the extent of the region where slip is significant. At present this parameter remains an empirical input.

Though figure 2.2 may suggest differently, a slip condition can be applied at both static as well as dynamic contact lines. However, usually no-slip appears to be an adequate boundary condition on liquid motion (Chang et al., 1979), when static contact lines are considered.

#### 2.2.4 The Dynamic Boundary Condition

Thus far, the boundary conditions discussed have addressed purely kinematic (motion) considerations. The way in which stresses transmit across an interface, or equivalently, the way in which forces balance on an interface needs to be considered as well. Therefore a force balance is set up over a material body containing two distinct fluid phases (figure 2.3), which yields (Palmer, 1997):

$$\mathbf{n}_1 \cdot (\mathbf{T}_2 - \mathbf{T}_1) + [\nabla - \mathbf{n}_1 (\mathbf{n}_1 \cdot \nabla)] \cdot \mathbf{T}_\sigma = 0 \quad 2.15$$

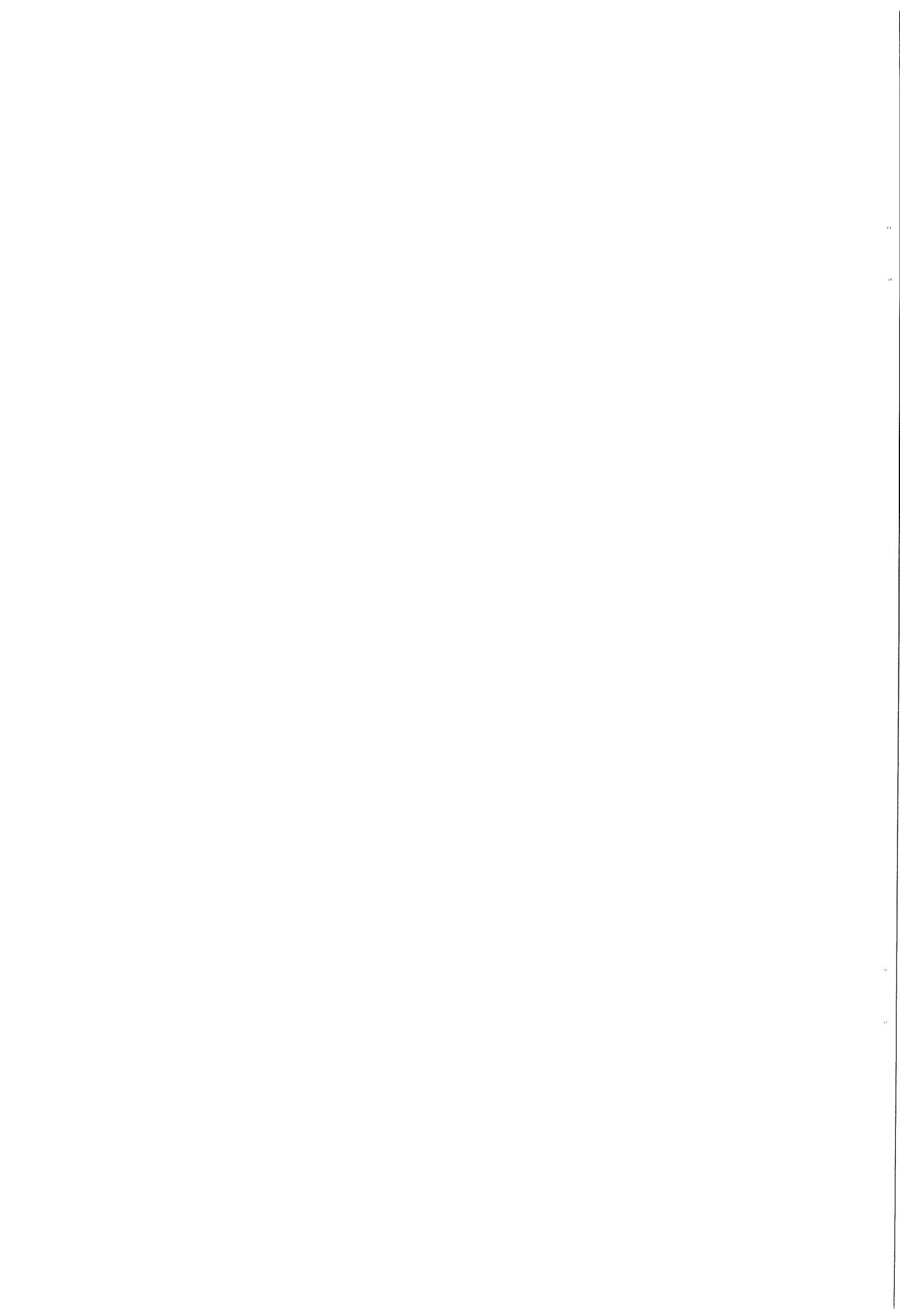
As in the case of the total stress tensor  $\mathbf{T}$ , a *constitutive* relation must be defined to relate  $\mathbf{T}_\sigma$ , the interfacial stress tensor, to physical quantities associated with the interface. The simplest of such constitutive relations, used exclusively in this thesis, is given by:

$$\mathbf{T}_\sigma = \sigma (\mathbf{I} - \mathbf{n}_1 \mathbf{n}_1) \quad 2.16$$

Substituting equation 2.16 into 2.15 and applying various tensor identities yields, for a two dimensional geometry (Palmer, 1997):

$$\mathbf{n}_1 \cdot (\mathbf{T}_2 - \mathbf{T}_1) = -[\nabla - \mathbf{n}_1 (\mathbf{n}_1 \cdot \nabla)] \sigma + \sigma \frac{d\mathbf{t}}{ds} \quad 2.17$$

where  $\sigma$  is the surface tension of the liquid,  $\mathbf{t}$  the unit tangent to the interface and  $s$  the arc length along the free surface.



For the purpose of this thesis only free surfaces between a liquid and any gas, that to good approximation is inviscid and inertialess, are considered. Furthermore surface tension is assumed to be a constant. The dynamic boundary condition is then given in dimensionless form as:

$$\mathbf{n} \cdot \mathbf{T}^* = \frac{1}{Ca} \frac{dt}{ds^*} - \mathbf{n} p_a^*$$

2.18

It relates the total normal stress  $\mathbf{nn}:\mathbf{T}$  on the liquid side to the curvature  $dt/ds$  by which surface tension generates a normal resultant, and requires the tangential or shear stress  $\mathbf{tn}:\mathbf{T}$  on the liquid side to vanish. The importance of surface tension forces to viscous stress is measured by the capillary number,  $Ca$ , defined in table 2.1.

### 2.2.5 Contact Angles & Lines

The mathematical expression for the curvature, the interfacial derivative, implies that additional boundary conditions are needed to determine the interfacial parametrisation. In coating processes it is common for one or more fluid-fluid interface to come in contact with a solid boundary. The line of such contact is called a contact line, and the angle of intersection,  $\theta$ , is called the *apparent* contact angle; both of these are shown for an air-liquid system in figure 2.2.  $\theta$  is an *apparent* contact angle, since it is merely the angle at which the liquid-gas meniscus at macroscopically observable distance from the solid appears to intersect the solid surface (Mohanty, 1981).

There are two types of contact lines, static and dynamic or wetting lines. These types can be subdivided into three possible configurations. Either the contact line is free to slide along the wall, in which case the apparent (dynamic) contact angle has to be specified as a boundary condition,

$$\mathbf{n}_\theta \cdot \mathbf{n}_s = \cos(\theta)$$

2.19

this is the case for static separation lines. Here  $\mathbf{n}_\theta$  is the unit normal to the visible free surface at the contact line.

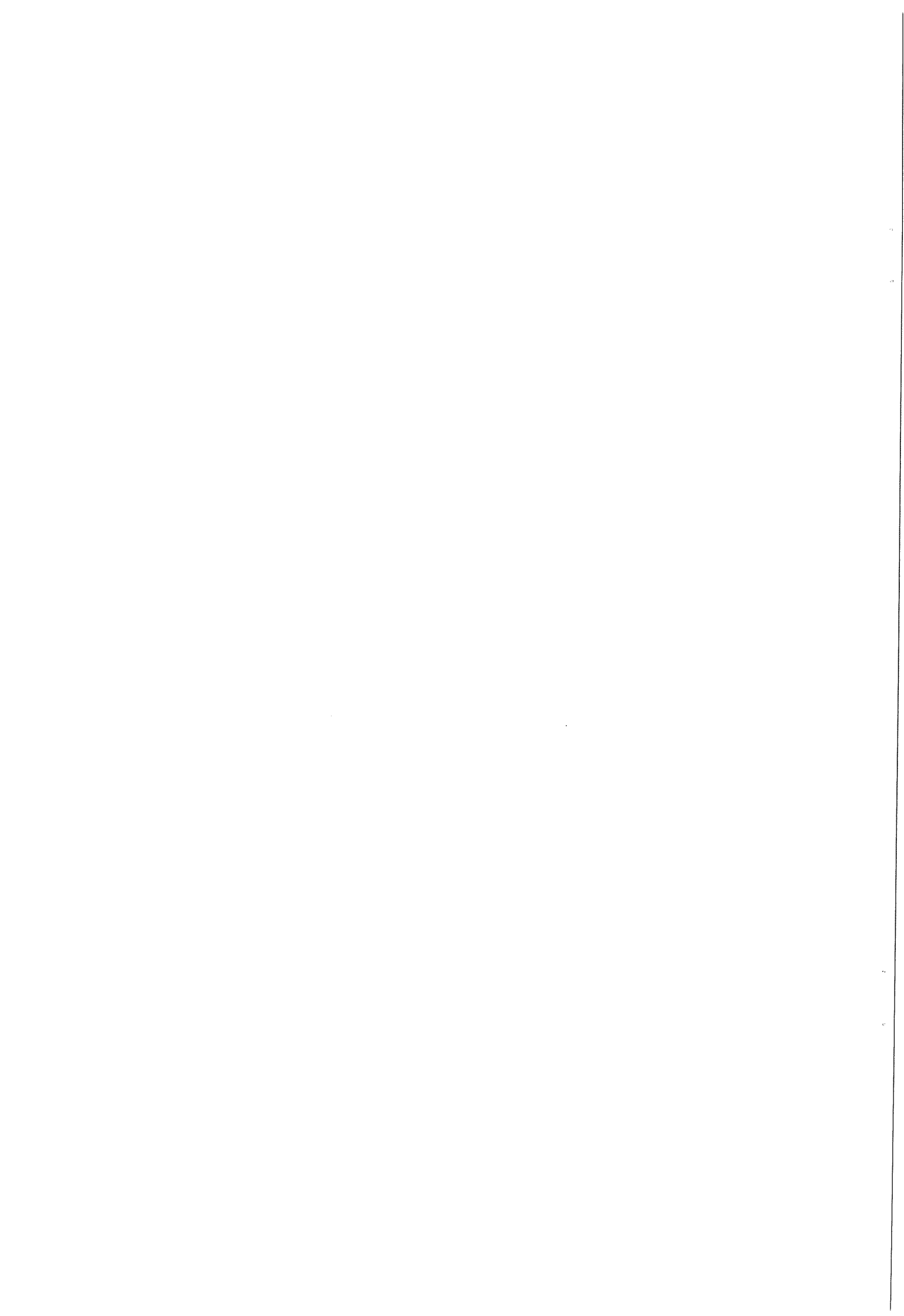
The contact line may also remain pinned, in which case the location of the apparent contact line must be prescribed,

$$\mathbf{x} = \mathbf{x}_c$$

2.20

This is the case for static attachment lines, for instance along a corner or compositional discontinuity. Finally the contact angle may remain pinned until the contact angle exceeds a critical value and then slides along the solid surface.

In the limiting regime of high enough capillary number the apparent dynamic contact angle and the wetting line position can be made dependent variables rather than parameters to be specified (Kistler, 1984). In practice capillary numbers are of  $O(1)$  and either condition (2.19) or (2.20) is used.



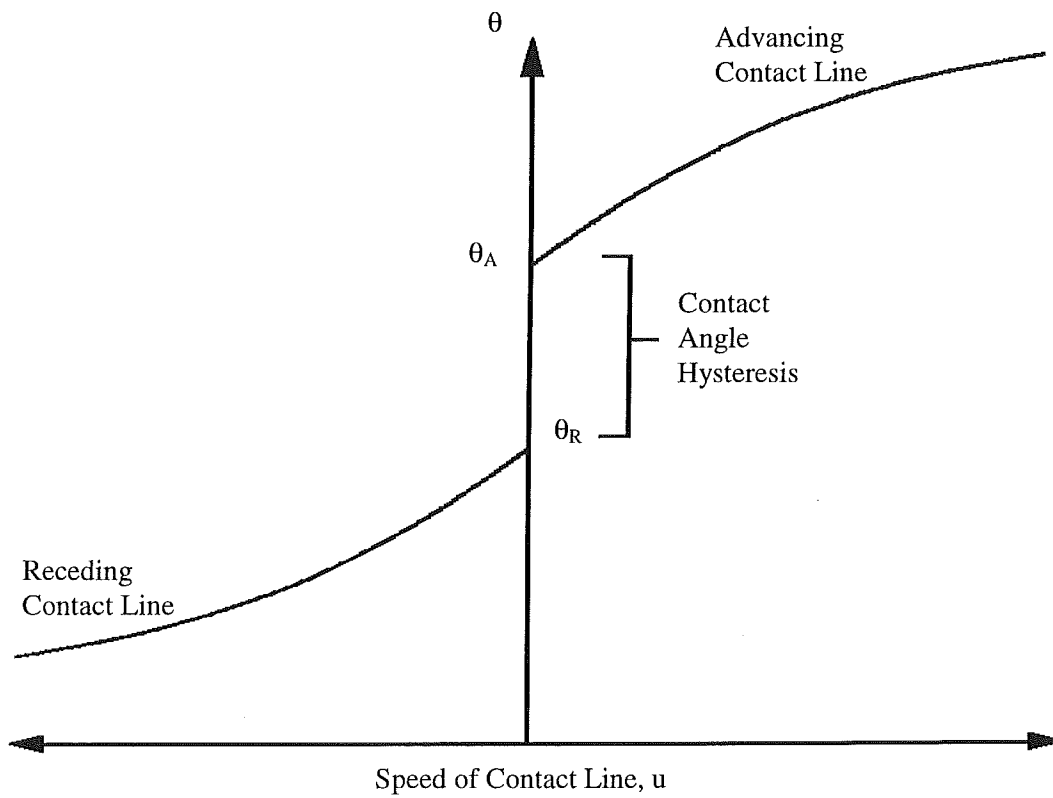


Figure 3.1: The dependence of the contact angle on the speed of the contact line.

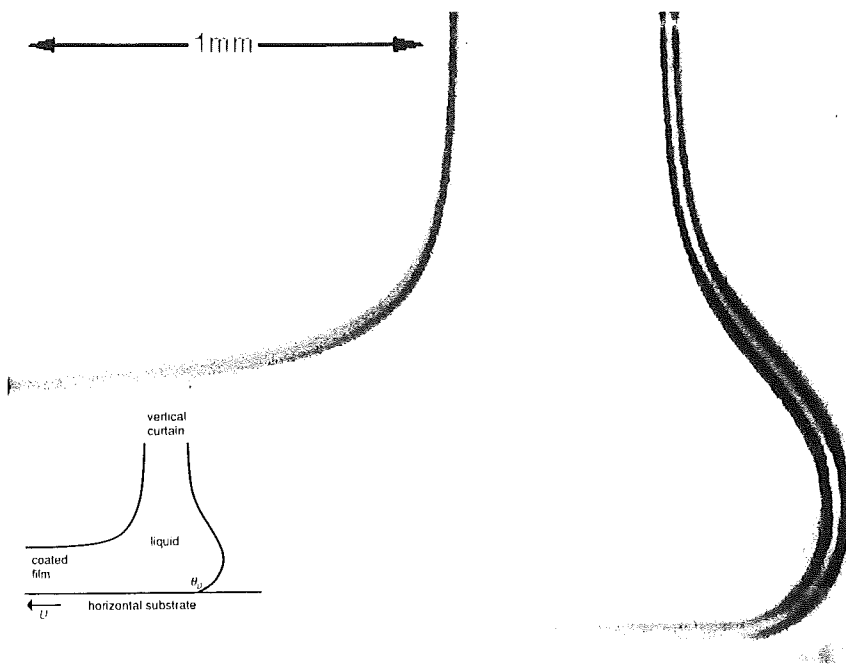


Figure 3.2: Visualisation of the dynamic contact angle.

---

## 2.2.6 Inlet & Outflow Boundary Conditions

Far enough upstream and downstream of the forming zones in many, if not most, coating operations the flow is well approximated by simple fully developed regimes. If inflow and outflow boundaries are placed there, the appropriate Dirichlet or Neumann boundary conditions are easy to specify. Typically the velocity distribution at an inflow plane is plug-like or (semi-)parabolic. If a free surface reaches there, the position of the meniscus is known. These are *essential* or Dirichlet boundary conditions.

At the outflow plane it is preferable to specify *natural* or Neumann conditions, in order to avoid conflicts with overall mass and momentum conservation. In NEKTON the following natural conditions are used: the slopes of interfaces (i.e. unit tangents) are given indirectly through imposition of the angles of the free surface with the outflow plane. Furthermore, at the outflow plane a zero gradient is assumed for all variables except pressure, which is defined there.

Solutions for which either regimes of fully developed flow are imposed at a finite distance upstream or downstream, have to be tested by changing the position of inflow and outflow planes.

### 3. Dynamic Wetting Parameters

In chapter 2 it was shown that numerical simulations of coating flows require two parameters, the apparent dynamic contact angle,  $\theta$ , and the slip coefficient,  $\beta$ . At present their appropriate values must be conjectured, however considerable research has been done to understand the mechanism by which a liquid wets a solid. In this chapter an overview is given of the presently available methods, both theoretical as well as empirical, for determining both parameters.

#### 3.1 The Contact Angle

The only observation universally accepted is that, for a given material system and flow geometry, the contact angle is related to the speed of the contact line,  $u$ , by a curve as shown in figure 3.1; and that the contact angle increases more rapidly for low viscosity liquids. In figure 3.1 three regions can be distinguished: for positive values of  $u$  wetting takes place (advancing contact line) and for negative values dewetting (receding contact line). Both curves, however, do not coincide at zero velocity of the contact line; due to contact angle hysteresis there is a range of static angles. In order to achieve a static contact line, it is necessary that all contact angles along the contact line lie within the hysteresis range; if they do not, then there will be contact line motion in those sections whose contact angles lie outside the hysteresis region.

##### 3.1.1 Experimental Methods

There are several methods for measuring apparent dynamic contact angles, e.g. *capillary displacement*; used for fundamental study; the *plunge-tank* and the *plunge-tape* configuration, used for 'coatability' and maximum wetting studies; and more recently *syringe-needle extrusion coating* (Zvan et al., 1992), which replicates essential aspects of the dynamics in industrial coating processes, while requiring only small samples of coating solutions.

In many experiments  $\theta$ , is measured directly through low-resolution optics. Through such observations, the contact angle can be determined at a distance of, at best, about 0.01 mm from the solid. Since many authors have not specified this distance at all, comparison of measured values of  $\theta$  remains dubious. Figure 3.2 shows an example of the dynamic contact angle measurement for a liquid curtain impinging on a horizontal tape, the free surface is visualised by using hydrogen bubbles (Blake et al. 1994).



### 3.1.2 Theories

Contact-angle variation with speed is usually attributed to one or both of two general theories: molecular-kinetic theory or hydrodynamic theory.

#### 3.1.2.1 Molecular-kinetic Theory

The molecular-kinetic theory of dynamic wetting is based upon the methods developed by Eyring and others (Glasstone, Laidler and Eyring, 1941). The theory views wetting-line movement statistically as a stress-modified rate process composed of individual molecular displacements (Blake, 1993); the dynamic contact angle is considered to be the actual contact angle.

According to Blake, the primary driving force for wetting-line motion is shear stress, which is provided by the out-of-balance interfacial tension forces acting at the wetting line and arising from the change in the contact angle from its equilibrium value  $\theta_0$  to some dynamic value. Per unit length of the wetting line, these forces will amount to:

$$F = \sigma (\cos(\theta_0) - \cos(\theta))$$

3.1

Since there are no experimental data of the microscopic contact angle, the macroscopic apparent dynamic contact angle is used. According to Blake (1993), this should not be a serious limitation since equation 3.1 will always provide a good measure of the irreversible work done by surface tension forces.

Although molecular interactions between the liquid and solid provide a major barrier to wetting line movement, the retarding influence of the viscosities of the advancing and retreating fluids on the motion of the molecules (Cherry and Holmes, 1969) can also be taken into account. The final expression relating the wetting line speed,  $u$ , to the dynamic contact angle is:

$$u = 2 \kappa_s \lambda \left( \frac{h^2}{\eta_1 \nu_1 \eta_2 \nu_2} \right) \sinh \left[ \frac{\sigma (\cos(\theta_0) - \cos(\theta))}{2 N k T} \right]$$

3.2

where  $\kappa_s$  is the frequency of molecular displacements at equilibrium when retarded only by surface forces;  $N$  the number of adsorption sites per unit area;  $h$  Planck's constant;  $k$  Boltzmann's constant;  $\nu_i$  the molecular flow volume of phase  $i$ ; and  $T$  the temperature.

Since the average distance between two adsorption sites,  $\lambda$ , is estimated as  $\sqrt{N}$ , there are effectively just two parameters,  $\kappa_s$  and  $N$ , that are determined by fitting experimental data. Typical values of  $\kappa_s$  and  $N$  at room temperature, for wetting of a PET tape with aqueous glycerol solutions of differing viscosities, are  $O(10^{11} \text{ s}^{-1})$  and  $O(10^{18} \text{ m}^{-2})$  respectively (Blake, 1993).

An important property of equation 3.2 is that it predicts  $u$  to have maximum and minimum values corresponding to dynamic contact angles of  $180^\circ$  and zero,

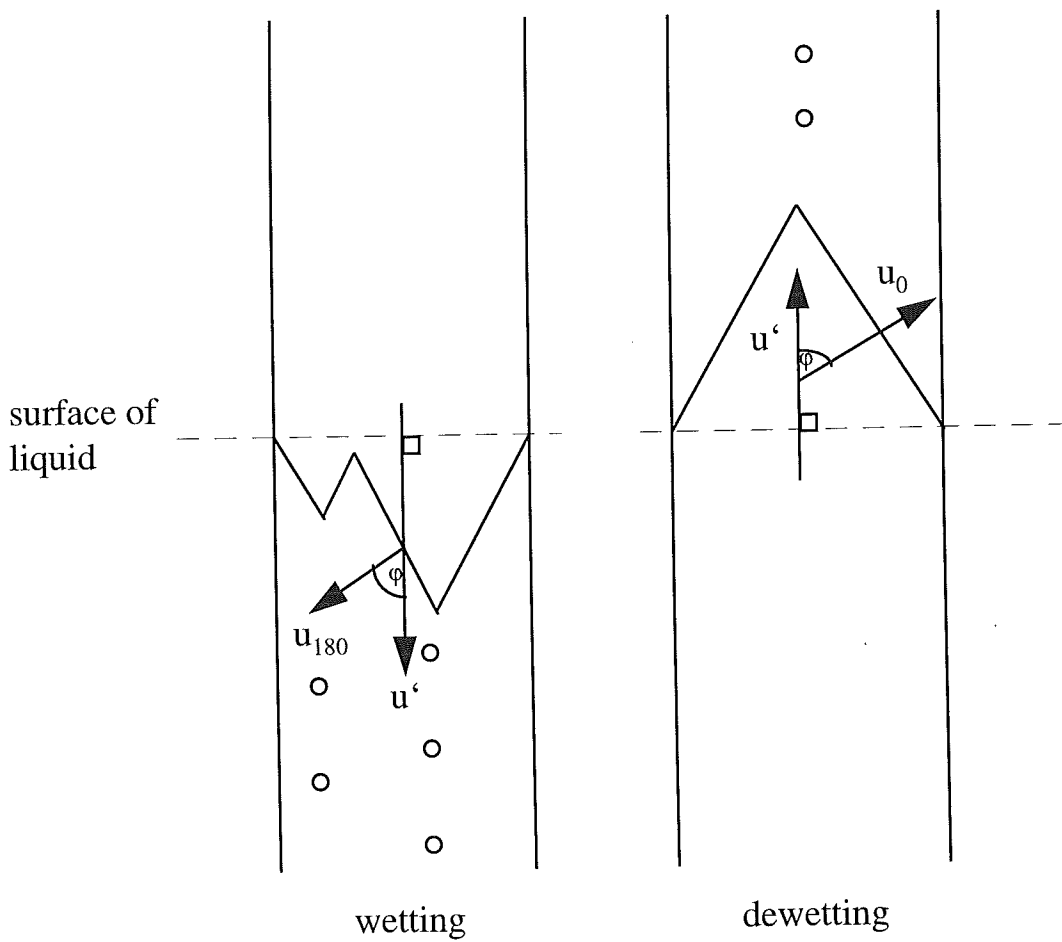


Figure 3.3: Formation of sawtooth wetting lines when a flat, solid surface is drawn into or out of a pool of liquid at velocities exceeding  $u_{180}$  and  $-u_0$ .

respectively. Beyond these values wetting will fail. Attempts to exceed these velocities cause the wetting line to lengthen and adopt a sawtooth configuration such that the component of the overall velocity of wetting  $u'$ , normal to each straight-line segment, remains constant at the limiting value (figure 3.3).

If  $\varphi$  is the angle between the normal to the wetting line and the overall direction of wetting, then:

$$\cos(\varphi) = \frac{u_{180}}{u'}$$

3.3

At sufficiently high velocities, the displaced phase is entrained from the trailing vertices of the sawteeth. Since  $\cos(\theta_0)$  can vary only between  $\pm 1$ , any substantial decrease in  $\sigma$  will increase the risk of entrainment. Thus, the addition of surfactants as "wetting agents" may sometimes be counterproductive.

### 3.1.2.2 Hydrodynamic Theory

A second approach, first investigated by Hansen and Toong (1971), is to account for much or all of the change in the dynamic contact angle through hydrodynamic bending of the meniscus at distances so close to the wetting line as not to be visible; the dynamic contact angle differs from the actual angle on the submicroscopic scale. Voinov (1976) developed the mathematics of this approach for a liquid displacing air. He considered conditions for which the slope of the meniscus changes slowly with distance from the solid. The flow field local to a point on the interface can then be approximated by flow in a wedge with an angle determined by the solid surface and the local meniscus slope. An integration of these wedge flows yields the meniscus shape. Voinov avoids the wetting line singularity by truncating the solution at molecular dimensions. Tanner (1979) eliminated the singularity by permitting local slip. Both found a similar relation for the dynamic contact angle:

$$\theta^3 - \theta_0^3 = c_T Ca \quad \theta < \frac{3}{4}\pi$$

3.4

The term  $c_T$  is basically an adjustable parameter and usually depends on the macroscopic scale of the flow,  $L$ . Sometimes, the so-called *capillary length*:

$$L_\sigma \equiv \sqrt{\frac{\sigma}{\rho_1 g}}$$

3.5

is appropriate (the subscript 1 denotes the advancing fluid). Because of contact angle hysteresis the value of static contact angle is uncertain and sometimes even considered to be an adjustable parameter. A systematic deviation from the universal curve (3.4) sets in above  $Ca \geq 0.1$ , or equivalently  $\theta \geq 135^\circ$ . It is most pronounced for low-viscosity liquids for which  $\theta$  rapidly increases toward  $180^\circ$ . For high-viscosity liquids, in contrast,  $\theta$  data approach  $180^\circ$  asymptotically. Two-phase-flow theory (Cox, 1986) suggests that the difference in dynamic wetting behaviour arises primarily from



viscous effects in the receding gas phase. Which are more pronounced when low viscosity liquids are used. The influence of the receding phase is commonly overlooked when that phase is air, but can affect the flow in the advancing liquid quite strongly when  $\theta$  is near  $180^\circ$  and the liquid viscosity is low.

### 3.1.3 Empirical Correlations

Empirical correlations can be divided into two groups. Those based on dimensional analysis and those aimed at capturing the universal behaviour  $\theta = f(\text{Ca}, \theta_0)$  discussed in paragraph 3.1.2.1. A representative example of such a dimensionless correlation is the one by Gutoff and Kendrick (1982):

$$\theta(u) = 6.24 \text{Ca}^{0.22} N_p^{-0.099} \left( \frac{\eta}{\eta_{\text{air}}} \right)^{0.36} \quad 3.6$$

In which  $N_p$  is the so-called property number:

$$N_p = \frac{g \eta^4}{\rho \sigma^3} \quad 3.7$$

Though successful in unifying data that appear widely scattered in unprocessed form, these type of correlations fail to shed light on the key mechanisms that control dynamic wetting.

Many of the "universal" models are special cases of the form:

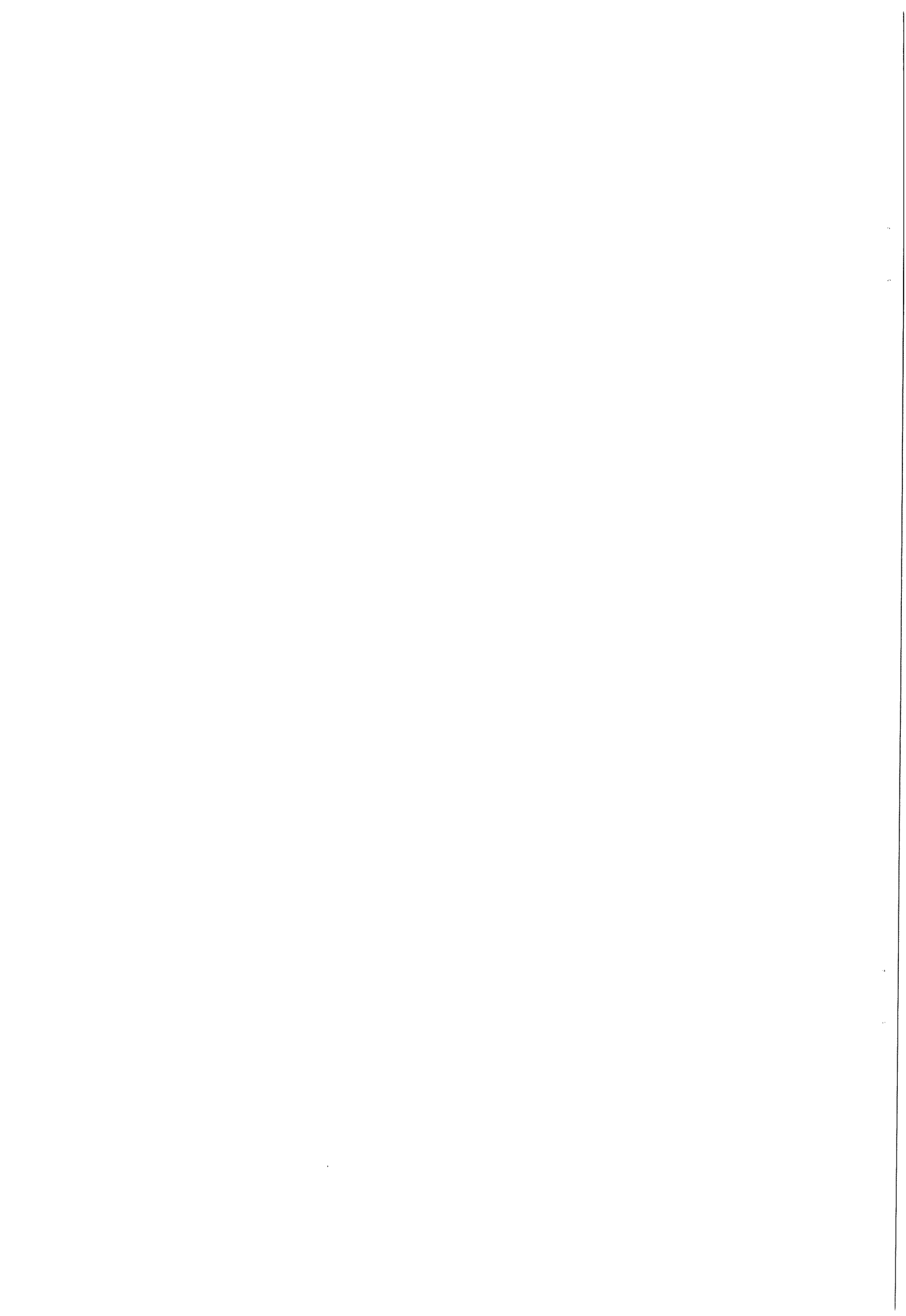
$$\Delta \cos(\theta) = \cos(\theta_0) - \cos(\theta) = f(\theta_0, \text{Ca}) \quad 3.8$$

The term  $\Delta \cos(\theta)$  is again the out-of-balance Young's force which is also used in the molecular-kinetic theory as a driving force for dynamic wetting. For convenience  $H$  is defined, which normalises dynamic contact angle data between 0 and 1:

$$H = \frac{\cos(\theta_0) - \cos(\theta)}{\cos(\theta_0) + 1} = f(\theta_0, \text{Ca}) \quad 3.9$$

## 3.2 Slip

Slip is probably an essential mechanism in dynamic wetting; at least at molecular length scales at which dynamic motions of individual molecules can combine to advance a liquid front over a dry solid or a solid covered by a few adsorbed layers. Specific molecular processes that have been invoked to rationalise slippage include a time delay required to complete liquid bonding to the surface (Huh and Mason, 1977), cohesive failure of liquid/liquid bonds between molecular layers



parallel to the solid (Durbin, 1988), and surface diffusion induced by a gradient of the fluid/solid interaction potential (Neogi and Miller, 1982). The last model for slip results from the molecular-dynamic theory (eq. 3.2). Although slip near advancing wetting lines is plausible for several reasons, hydrodynamics models that rely on slip as an ad hoc boundary condition predict several unphysical characteristics of the flow within the cut-off region. One such characteristic is the pressure field that remains singular at the wetting line even when the liquid is allowed to slip over the solid. The singularity, which is now integrable, stems from the discontinuity in shear stress where the fluid/fluid interface intersects the solid. It is analogous to the singularity encountered in flow calculations at static contact lines.

Another disconcerting feature predicted by hydrodynamic theories is the notion that the wetting line always consists of the same material points. This contradicts the basic concept of coating a fluid on a solid while displacing another.

The unphysical features of flow fields calculated with the help of slip-flow models arise because hydrodynamic analyses of dynamic wetting are refined at inordinately small length scales. The slip length is often less than  $0.1 \mu\text{m}$  and sometimes even of molecular scale. At these length scales conventional continuum theory ought to be augmented to account for microstructural forces, but will break down eventually at molecular scales.



## 4. Numerics

Practically relevant analyses of realistic coating processes often require advanced numerical methods that solve the full set of Navier-Stokes equations and associated boundary conditions. For this purpose the commercially available code NEKTON -Release 3.0-, marketed by Fluent Inc., was used. The computational method used in this code is called the *spectral-element* method and belongs to the class of the *variational* methods. In this chapter the basics of this method: discretisation, imposition of boundary conditions, mesh generation, solution of the linear equations, iteration and convergence criteria, as implemented in the code are discussed. Furthermore attention is paid to the numerical imposition of dynamic contact angles and slip.

### 4.1 Discretisation

In flow regions of viscous free surface flows where the flow domain fits no standard co-ordinate system, the variational methods are the technique of choice for finding steady and transient solutions of the governing equations and their boundary conditions. The main idea is to approximate the unknown flow field (i.e., velocity, pressure, flow geometry, etc.) in terms of a collection of particularly simple, polynomial *basis* functions. These are non-zero only on a single subdomain of the flow domain, in contrast to the traditional functions of mathematical physics, which span the entire domain.

Spectral-element analysis of free-surface flows can start from several formulations of the governing equations depending on the treatment of the compressibility constraint (Gresho, 1991): the primitive-variable or velocity-pressure (v-p) formulation; and the penalty function formulation, which is very attractive because it allows elimination of the pressure unknowns and thereby significantly reduces the dimension of the discretised equation set. For solving the Navier-Stokes equations, NEKTON exclusively uses the v-p formulation.

#### 4.1.1 v-p formulation

In the v-p formulation, the system of governing equations with its associated boundary conditions is discretised as is, using a so called mixed interpolation. Velocity, pressure and nodal position are expanded in terms of Legendre polynomial (3<sup>rd</sup> -14<sup>th</sup> order) basis functions  $\phi^i(\xi, \eta)$ ,  $\psi^k(\xi, \eta)$  and  $\phi^j(\xi, \eta)$  which are constructed on a standard element, for instance a square with local  $\xi$  and  $\eta$  co-ordinates in the range  $-1 \leq \xi \leq 1$  and  $-1 \leq \eta \leq 1$ :

$$\mathbf{v} = \sum_i \mathbf{v}_i(t) \phi^i(\xi, \eta)$$

$$p = \sum_k p_k(t) \psi^k(\xi, \eta)$$

$$\mathbf{x} = \sum_j \mathbf{x}_j(t) \phi^j(\xi, \eta)$$

4.1

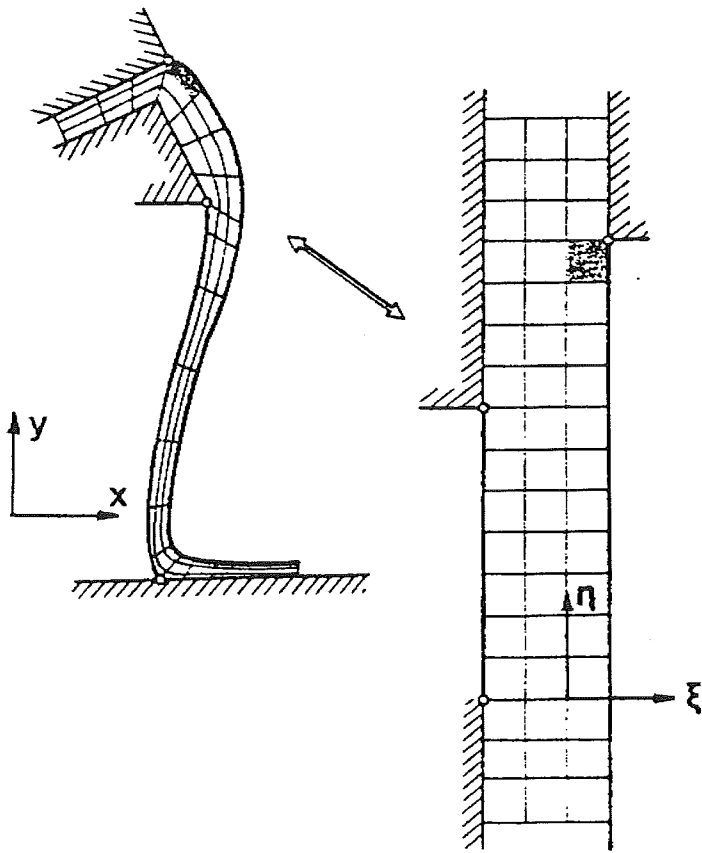


Figure 4.1: Translation of the physical domain to the computational domain (Kistler, 1984).

As mentioned earlier these basis functions are defined only locally (i.e., within each element) and need only have limited continuity between elements. The coefficients  $v_i$ ,  $p_k$  and  $x_j$  are the unknowns. With the exception of those variables for which the basis functions are discontinuous at inter-element boundaries, the coefficients represent nodal values of the flow field and flow geometry. They are time dependent in transient analyses and constant in steady-state analyses.

In order to ensure that the discrete pressure field is not polluted by non-physical oscillations - so called spurious pressure modes - NEKTON uses different degrees of polynomials to approximate the velocity terms (N order) and the pressure terms (N-2) order. Pressure is not being computed on element boundaries nor is continuity of pressure enforced there; instead it is an indication of convergence.

Equal-order interpolation is most commonly used for nodal position and velocity, as in equation 4.1. The mapping of each element of the mesh in the physical domain onto the standard domain  $(\xi, \eta)$  on a rectangular grid is then called *iso-parametric* (figure 4.1).

The governing equations are transformed into a discretised system of ordinary differential equations by multiplying with the appropriate basis functions, integrating over the computational domain, and applying the divergence theorem to the momentum equation (in dimensionless form for steady state, two dimensional flow) (Kistler, 1983):

$$\mathbf{R}_i^M \equiv \int_A \left[ \mathbf{T}^* \cdot \nabla \phi^i + \left( \text{Re}(\mathbf{v}^* \cdot \nabla^* \mathbf{v}^*) - \text{St} \mathbf{f} \right) \phi^i \right] dA - \int_{\partial A} (\mathbf{n} \cdot \mathbf{T}^* \phi^i) ds^* = 0$$

$$\mathbf{R}_k^C \equiv \int_A (\psi^k \nabla^* \cdot \mathbf{v}^*) dA = 0$$

$$\mathbf{R}_m^K \equiv \int_{\partial A_f} [\mathbf{n} \cdot (\mathbf{v}^*) \phi^m] ds^* = 0$$

4.2

Here  $\mathbf{R}^M$ ,  $\mathbf{R}^C$  and  $\mathbf{R}^K$  denote momentum, continuity and kinematic residuals;  $A$  denotes the computational domain,  $\partial A$  its entire boundary, and  $\partial A_f$  all free-surface boundaries. Introducing the expansions (4.1) into the integrals (4.2) turns the latter into a system of algebraic and ordinary differential equations -or just algebraic equations in the case of steady state calculations- for the unknown coefficients in the basis function expansions. The integrals are sometimes referred to as the *weak* form because the original set of governing equations and boundary conditions is satisfied only in an average, integral sense rather than being exactly valid at every point in the domain.



## 4.1.2 Imposition of Boundary Conditions

Essential boundary conditions, usually at solid or inflow boundaries, are imposed by replacing the corresponding weighted residual equations 4.2a or 4.2c with the desired velocity specifications. Natural boundary conditions, usually at free surfaces and outflow boundaries, are imposed through the boundary integral

$$\int_{\partial A} (\mathbf{n} \cdot \mathbf{T}^* \phi^i) ds \text{ in (4.2a).}$$

For example, the stress boundary condition at the free surface is imposed by substituting the right-hand side of (2.18) into the traction boundary integral of (4.2a) and applying the surface divergence theorem (Ruschak, 1980). For two-dimensional problems equation 4.2a becomes:

$$\mathbf{R}_i^M \equiv \int_A \left[ \left( \text{Re}(\mathbf{v}^* \cdot \nabla^* \mathbf{v}^*) - \text{St} \mathbf{f} \right) \phi^i + \nabla \phi^i \cdot \mathbf{T}^* \right] dA - \frac{1}{\text{Ca}} \int_{\partial A_r} \left( \mathbf{t} \frac{d\phi^i}{ds^*} \right) ds^* - \frac{1}{\text{Ca}} (\phi^i \mathbf{t}_1 - \phi^i \mathbf{t}_0) = \mathbf{0} \quad 4.3$$

The end-point terms in (4.3) can be interpreted physically as shell forces due to surface tension. Their directions  $\mathbf{t}_0$  and  $\mathbf{t}_1$  have to be specified at the inflow and outflow boundaries, and also at contact lines. This procedure works where a free surface intersects an inflow or outflow plane. At (dynamic) contact lines, however, the specified contact angle is imposed by discarding the kinematic boundary residual (4.2c) at the contact line node and replacing it by the normal component of the momentum residual (Kistler and Scriven, 1983).

Evaluating the integrals in the weighted residuals takes a numerical integration procedure; for this NEKTON uses Gauss quadrature.

## 4.2 Mesh Generation

The system of weighted residuals (4.2a)-(4.2c) is closed by suitable mesh generation equations. For an accurate solution of free-surface problems, so-called boundary conforming meshes that adapt to changes in the free-boundary shape independently of the underlying liquid flow are particularly well suited. This mesh movement strategy, which accurately tracks the irregular flow domain, is sometimes called *arbitrary Lagrangian-Eulerian* (ALE) because the mesh is neither fixed (Eulerian frame of reference), nor are all nodes (including free surface nodes) relocated with their local velocities (Lagrangian frame of reference).

Instead only the free surface nodes are relocated; the values of the nodal coordinates in the interior of the computational flow domain are then calculated from the values at the boundaries. There are currently three different approaches to mesh generation: algebraic mesh generation, e.g. spine-based deformation (Kistler and Scriven, 1984), differential mesh generation, e.g. elliptic mesh generation (Thompson et al., 1982) and NEKTON's *elastostatic mesh deformation* (Ho and Patera, 1990). In the latter, the evolution of the free surface is tracked with a mesh whose motion is tied to the fluid velocity normal to the free surface. The internal nodes are adjusted by solving the equations for an elastically deforming solid.

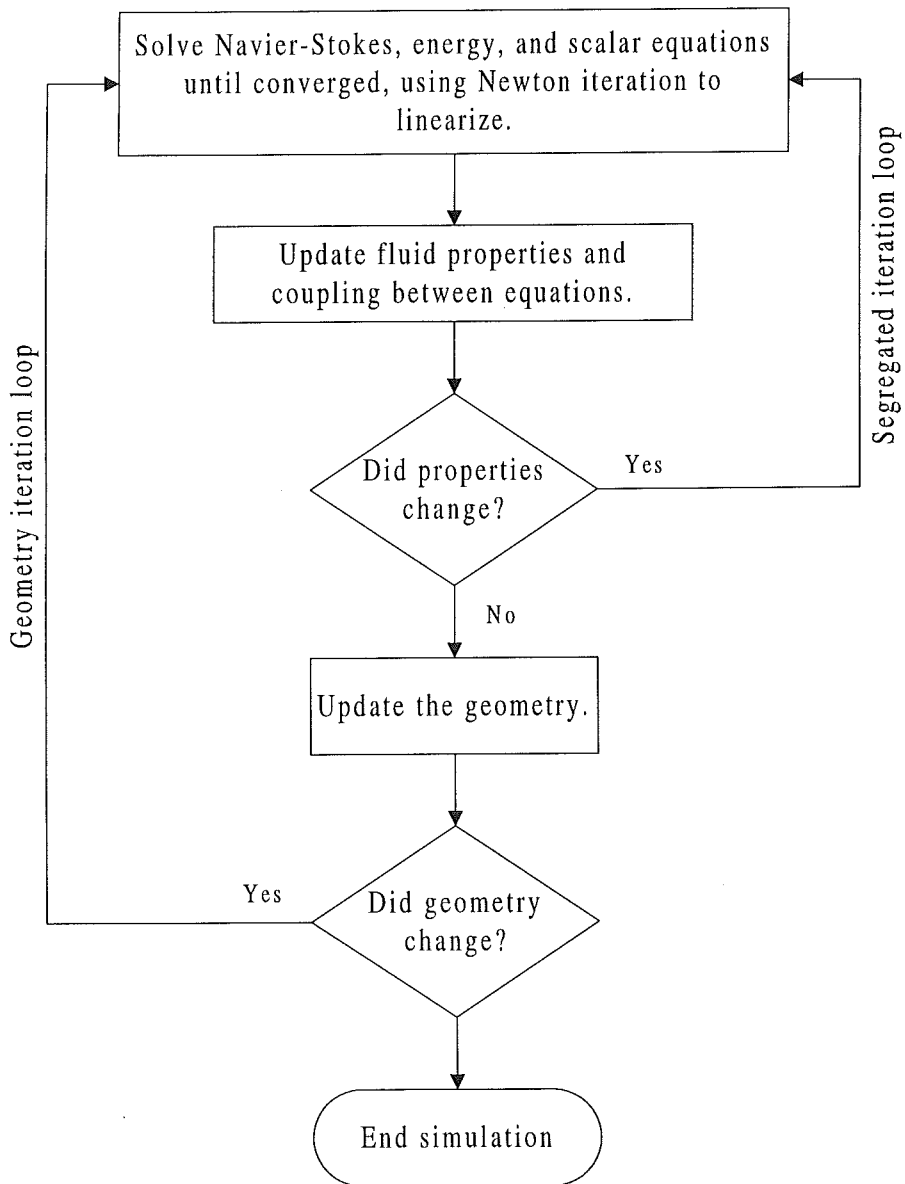


Figure 4.2: Iteration scheme for the direct and iterative coupled solvers.

### 4.3 Iteration Procedures

The discretised system of governing equations combined with the mesh generation equations is severely non-linear. Finding steady-state solutions therefore requires iteration. Figure 4.2 shows the iteration scheme followed by the direct and iterative coupled velocity-pressure solvers. First the discretised equations are linearised, using Newton iteration, and solved, directly or iteratively, till convergence on a fixed domain. Second the fluid properties are updated and the coupling between equations is established. When the properties change a segregated iteration is done; if not the geometry is updated using a picard iteration. The latest version of NEKTON -Release 3.1- uses two types of solvers to handle the Navier-Stokes equations, the coupled velocity-pressure and the coupled velocity-pressure-geometry solver. The latter solver is based on a different iteration scheme, wherein all flow variables and the nodal position are solved at the same time, using a Newton iteration.

#### 4.3.1 Solution of Linear Equations

The linearised discretised system of governing equations combined with the mesh generation equations produce one or more matrix equations of the form  $\mathbf{Ax} = \mathbf{b}$  that have to be solved at each iteration, i.e. segregated and geometry iteration. There are two methods for solving these matrices: *direct* matrix solvers and *iterative* matrix solvers. The main advantage of an iterative solver is that a much smaller amount of computer memory is required, compared to the direct solver. The main drawback of the iterative method in NEKTON is the sensitivity of the used GMRES algorithm to high aspect ratio elements.

#### 4.3.2 Picard Iteration

In two-dimensional viscous free-surface flows like coating flows, the traction condition (2.15) and the kinematic boundary condition (2.11) furnish three scalar boundary conditions, one more than would be required to solve the Navier-Stokes equations on a fixed domain. The third boundary condition - sometimes referred to as the *distinguished condition* - is necessary to determine the unknown position of the free surface. This is the principle of the so-called *trial method* used in the coupled velocity-pressure solver.

The trial method assigns, at each iteration step, a fixed shape to the free surface and computes the flow field, ignoring the distinguished boundary condition. Next, that boundary condition, along with the current estimate of the flow field, is used to update the free-surface location, and the cycle is repeated to convergence. The key advantages of this Picard iteration are its simplicity and, compared with the other method discussed below, its large radius of convergence. Its main drawback is the slow, linear rate of convergence and even worse the possibility that the method fails to converge depending on the choice of the boundary condition used to update the free surface and the value of the capillary number. Therefore there are three different steady free surface *solution algorithms* available in NEKTON. Two algorithms are based on the stress balance conditions: surface tension dominant and surface tension negligible. The other algorithm is based on the kinematic condition. Table 4.1 gives an indication of which algorithm to use for given combinations of Reynolds and capillary or Weber number.



Table 4.1: Choice of solution algorithm based on dimensionless numbers.

	Surface Tension Dominant	Surface Tension Negligible	Kinematic
Re < 1	Ca < 0.1	Ca > 10	0.1 ≤ Ca ≤ 10
Re > 1	We < 0.1	We > 10	0.1 ≤ We ≤ 10

#### 4.3.2.1 Surface Tension Dominant Algorithm

The Navier-Stokes equations are solved subject to a symmetry-like boundary condition on the free surface:

$$\mathbf{n}_i \cdot \mathbf{v}_i = 0$$

$$\mathbf{t}_i \mathbf{n}_i : \mathbf{T}_{ij} = 0$$

4.4

The resulting traction force vector is called  $\mathbf{n}_j \cdot \mathbf{T}_{ij}^{ss}$ . Based on the current velocity field, a point-by-point force balance is computed:

$$\mathbf{r}_i = \mathbf{n}_j \cdot \mathbf{T}_{ij}^{ss} - \sigma \frac{d\mathbf{t}}{ds}$$

4.5

The residual traction,  $\mathbf{r}_i$ , which is only zero at steady state, is now used as a driving force in the variational statement for the curvature operator. The resulting change in mesh co-ordinates on the free surface is then extended into the domain interior using an elliptic operator. Now all operators are updated, based on the new geometry and the process is repeated until convergence.

#### 4.3.2.2 Surface Tension Negligible Algorithm

The Navier-Stokes equations are solved subject to both tangential and normal traction boundary conditions:

$$\mathbf{n}_i \mathbf{n}_i : \mathbf{T}_{ij} = \sigma \frac{d\mathbf{t}}{ds}$$

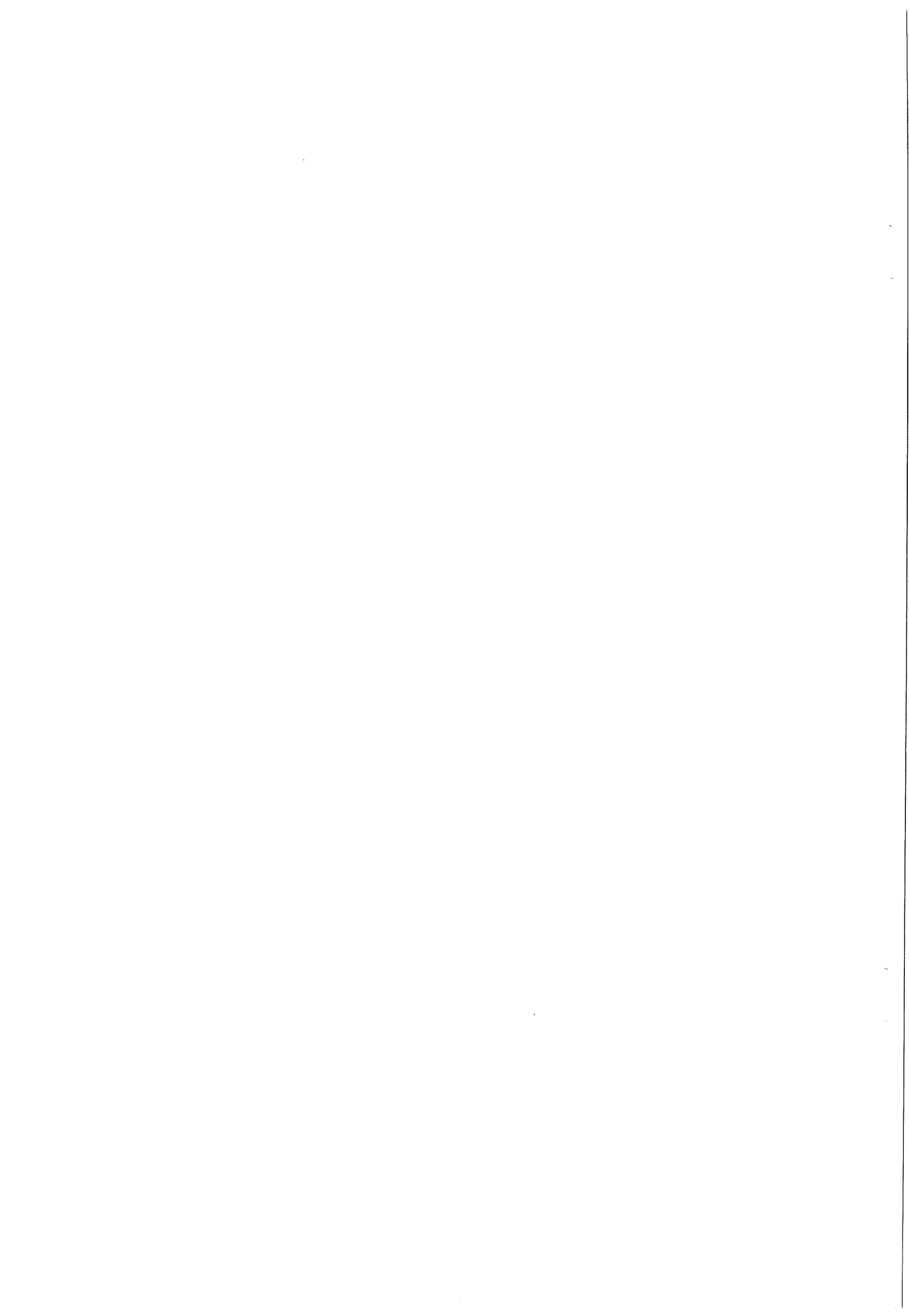
$$\mathbf{t}_i \mathbf{n}_i : \mathbf{T}_{ij} = 0$$

4.6

on the free surface. In general the normal component of velocity on the free surface is non-zero, so construct a source term,  $\mathbf{r}_i$ :

$$\mathbf{r}_i = (\mathbf{u}_k \cdot \mathbf{n}_k) \mathbf{n}_i$$

4.7



This source term, with appropriate scaling is then used to update the position of the free surface. Again the change in mesh co-ordinates is extended into the domain interior using an elliptic operator.

### 4.3.2.3 Kinematic Scheme

The kinematic scheme closely resembles the surface tension negligible algorithm in the first two steps. The resulting source term, however, is now called the mesh velocity,  $w_i$ . The change in mesh co-ordinates on the free surface is now solved for according to:

$$\frac{\Delta x_i}{\Delta \tau} = w_i$$

4.8

where  $\Delta \tau$  is a (pseudo) time step computed from the fluid velocity and the mesh spacing on the fixed free surface. Since there is no curvature solve, this method does not require iteration. Hence the computational effort for the kinematic scheme is lower than for the other two schemes.

The pseudo-time step used in this scheme does not honour the time step required for free surface stability. Thus, the solution may begin to oscillate, depending on the importance of surface tension effects. In this case, the time step can be reduced by setting the relaxation parameter to a value less than unity. In some cases, the pseudo-time step may be overly restrictive, causing the free surface to deform very 'slowly'. To overcome this the relaxation parameter can be set greater than unity.

### 4.3.3 Newton Iteration

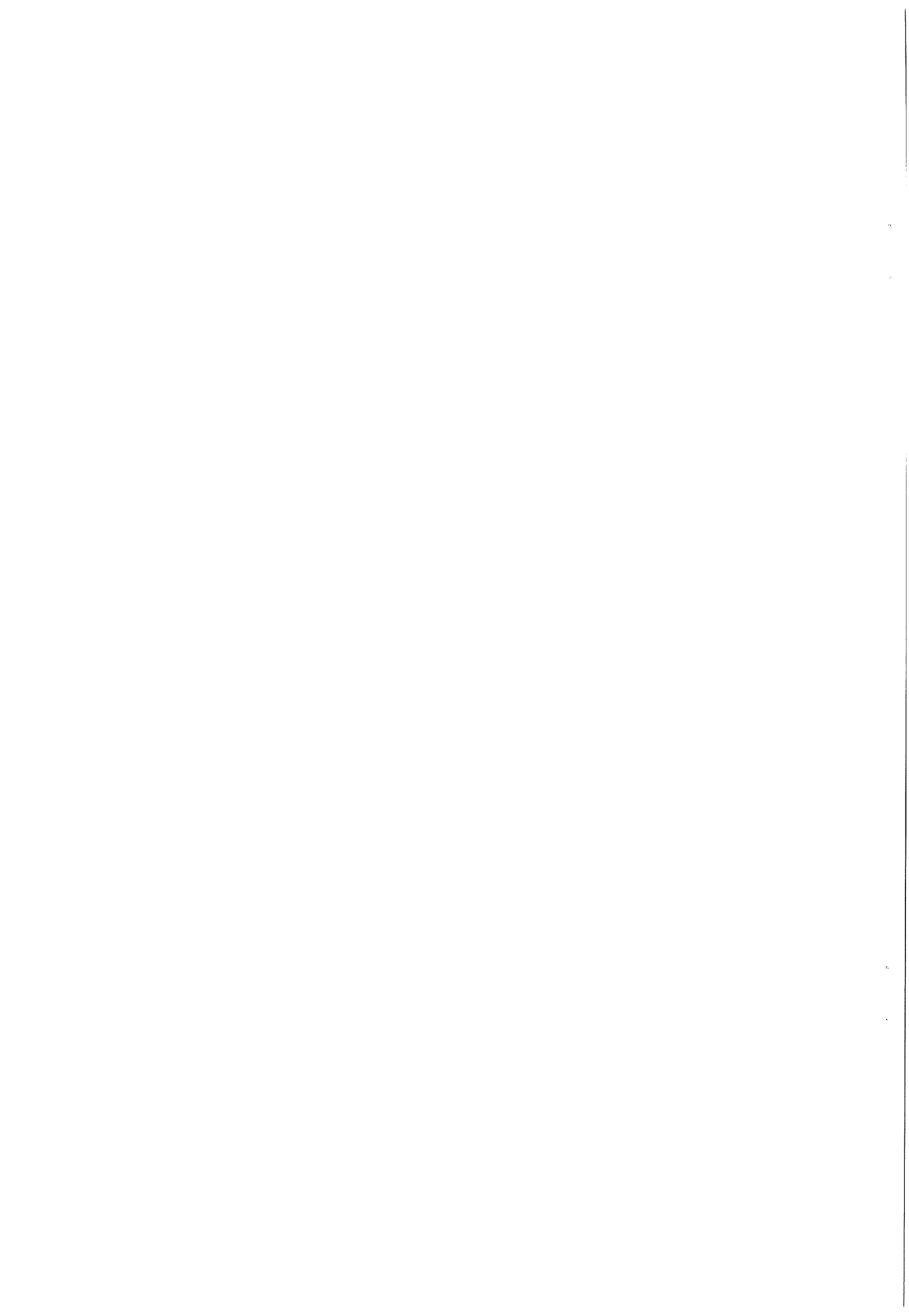
The tedious iteration between the flow-field calculation and the free-surface update can be avoided by simultaneously solving all the equations, including equations for the position of the nodes on the free surface and those in the domain interior. Newton's method (e.g. Isaacson and Keller, 1966) linearises the complete equation set,  $\mathbf{R}$ , around the current estimate of the solution,  $\mathbf{y}^k$ , to yield:

$$\frac{\partial \mathbf{R}}{\partial \mathbf{y}}(\mathbf{y}^k) \Delta \mathbf{y} = -\mathbf{R}(\mathbf{y}^k)$$

4.9

and adds the solution  $\Delta \mathbf{y} = [\mathbf{y}^{k+1} - \mathbf{y}^k]$  of the resulting linear system to the current estimate  $\mathbf{y}^k$  in order to provide an updated estimate of the flow field, including the position of the free surface(s). The iteration is repeated until convergence.

In contrast to the trial method, Newton's method converges quadratically and, hence, requires only four or five iterations in most cases, the number being independent of the flow parameters. Due to its small radius of convergence, however, Newton's Method requires a 'good' initial guess. Therefore the trial method should be used to obtain a 'good' initial guess and Newton's method should be used to speed up the convergence of this guess.



#### 4.3.4 Convergence Criteria

There are various ways to control when the solution process used by NEKTON (figure 4.2) should stop. First of all, if after a geometry update the solution has changed only by some very small amount between the previous iteration and the current one, the solution should be considered converged. There are three solution criteria:

- the maximum relative change in the velocity and scalar fields.
- the maximum relative change in geometry, which is defined as the maximum value of:

$$\frac{dx}{L} = \frac{(\Delta x^2 + \Delta y^2 + \Delta z^2)^{\frac{1}{2}}}{L}$$

4.10

on the free surface. A recommended value of the tolerance is  $1 \cdot 10^{-4}$ . For  $L$  a characteristic length scale of the flow is chosen.

- the maximum relative normal velocity on the free surface,  $V_n/V$ , when the surface tension negligible or kinematic steady free surface algorithm is used. Here  $V_n$  is the maximum normal velocity on the free surface, while  $V$  is the local fluid velocity. Thus, when using either of these two free surface algorithms, a converged solution must satisfy two convergence criteria:  $dx/L$  and  $V_n/V$ . A recommended value of the tolerance on the maximum normal velocity on the free surface is **0.01**.

Secondly if, within a segregated iteration, the residual for the particular governing equation currently being solved is very small, the equation is considered satisfied and the solution method moves on to the next equation. For the coupled velocity-pressure solvers used exclusively in this thesis there is just one residual criterion: the velocity-pressure tolerance, which is used to judge convergence of the Newton iteration for Navier-Stokes problems. The maximum relative change criterion is used to judge whether another segregated iteration is required after the properties have been updated, and is used for both iterative and direct solvers.

Finally, to prevent the solver from ‘getting stuck’ within a particular iteration loop, the maximum number of iterations for each equation can be set by using limiters.

#### 4.3.5 Contact Angles & Slip

When ‘translating’ the physical problem to a numerical problem some problems may arise with the empirical wetting parameters described in chapter 3. Imposing an apparent dynamic contact angle can be more subtle than is commonly appreciated. When the mesh is refined, the angle of meniscus inclination at ‘visible’ distances from the solid, as found from dynamic contact angle measurements, may be different from that imposed at the putative wetting line.

As far as the unphysical force singularity is concerned, there is another approach to overcome the need of a slip condition at the putative wetting line. The weak form



---

of the Galerkin weighted residual equations can accommodate multi-valued velocities at dynamic wetting lines without catastrophic consequences for the flow nearby. In this thesis both free slip and the Galerkin approach were used to solve the governing equations near the stress singularity. Since both methods are ad hoc ways of handling the stress singularity their physical significance is small. Comparison of the solution with experimental data is the only means of discrimination between the two methods.

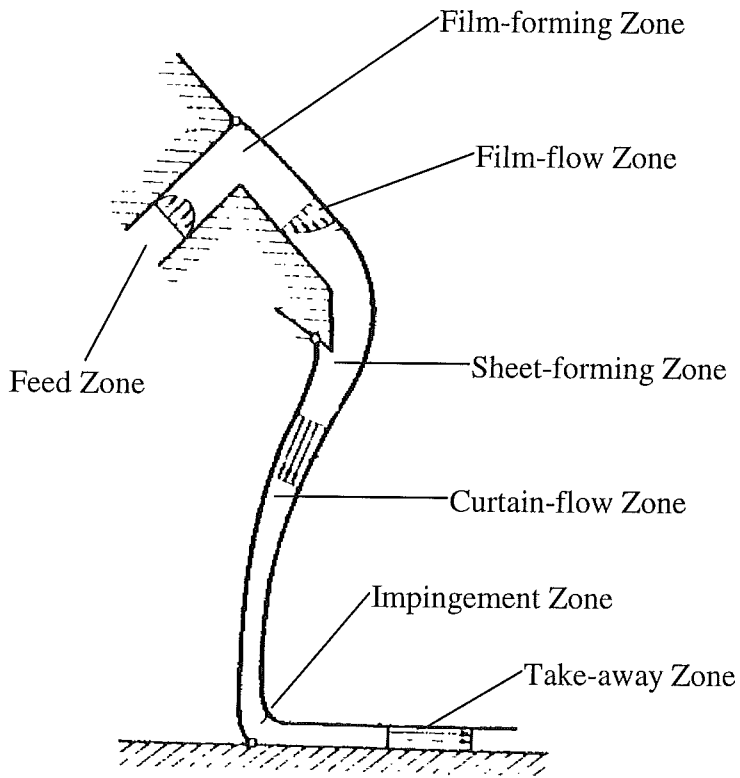


Figure 5.1: Division of the curtain coating flow into seven zones (Kistler, 1984).

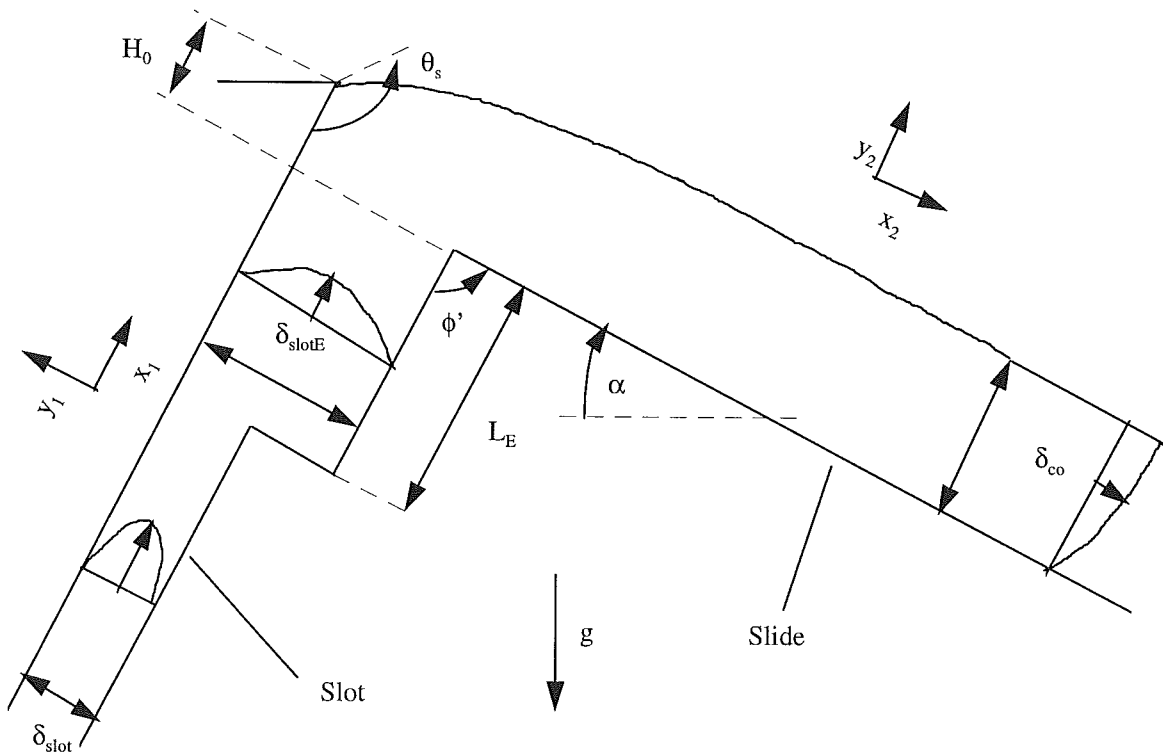


Figure 5.2: Schematic of the slide coater die.

## 5. Division of the Flow into Seven Zones

To organise the discussion of curtain coating and also to facilitate a theoretical analysis of the process, the flow is usefully divided into the seven zones shown in figure 5.1. The crucial zones are the short zones of fully two-dimensional flow rearrangement, called *forming zones*. In these zones, upstream influence is abundant, or in other words capillary pressure and normal viscous stress transmit momentum upstream against the flow so that the entire zone constitutes a system. These zones can only be solved realistically by using numerical techniques. In curtain coating, details of flow in the film-forming zone (e.g. Ade, 1976) and in the sheet-forming zone (e.g. Raux, 1976) significantly affect uniformity of the coated layers, while flow in the impingement zone to a large degree affects the range of operable process conditions.

Typically the forming zones merge with simpler regimes of developing flow and, in many cases, regions of fully developed flow far upstream and downstream. In these zones, which are here called *flow-developing zones*, the liquid undergoes predominantly shearing or extensional deformation. The fully developed regimes are easily solved analytically.

In this chapter a short description is given of the seven flow zones associated with a slide curtain coater.

### 5.1 Feed Zone

Liquid, fed to the coating die by a metering pump, arrives in the manifold where it is distributed over the full die width. In the feed slot the liquid then flows under a uniform pressure gradient. In this thesis the slide curtain coater die in figure 5.2, with its appropriate co-ordinate systems is considered. The velocity and shear profiles in the die are found when solving the momentum equations 2.4. For steady state, one dimensional flow, these equations reduce to a force balance:

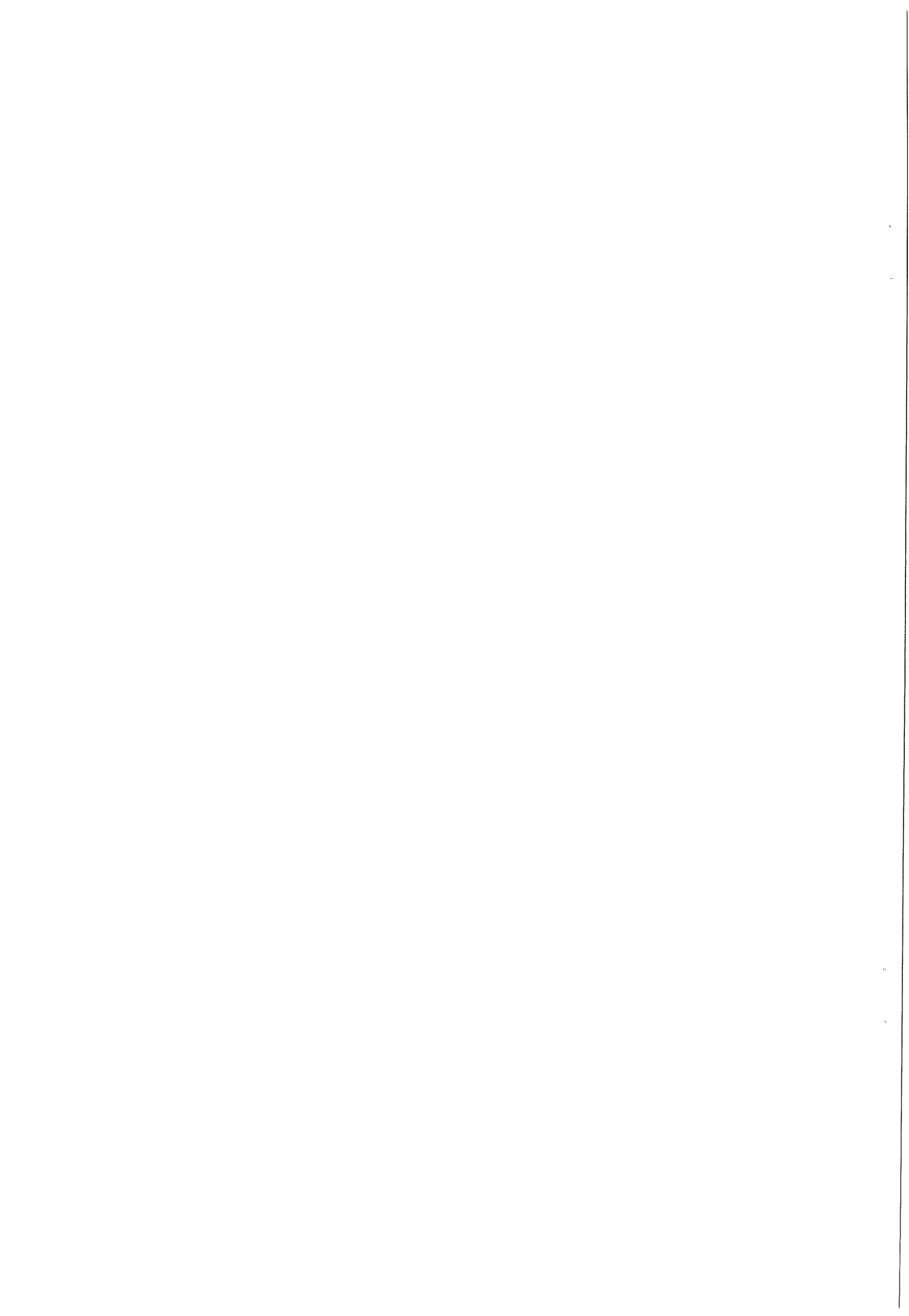
$$\frac{d \tau_{y_1 x_1}}{d y_1} = \Gamma + \rho g \sin(\phi) \quad 5.1$$

where  $\phi$  is the angle of projection of the gravity force, which is defined as:

$$\phi \equiv \alpha - 180^\circ + \phi' \quad 5.2$$

where  $\alpha$  is the angle of inclination of the die and  $\phi'$  the angle between the slide and the slot. Assuming Newtonian behaviour of the liquid (2.5), solution of equation 5.1 yields the following  $x_1$ -velocity profile:

$$v_{x_1} = \frac{\Gamma + (\rho g \sin(\phi))}{2 \eta} (\delta_{\text{slot}} y_1 - y_1^2) \quad 5.3$$



where  $\delta_{\text{slot}}$  is the slot height of the die and  $\Gamma$  the pressure drop per metre length between manifold and slit exit:

$$\Gamma = -\frac{dp}{dx_1} \tag{5.4}$$

The value for  $\Gamma$  is found when equating the flow rate per meter die width,  $q$ , also known as the premetered flow rate, to the integral of the  $x_1$ -velocity profile over the slot height of the die and rewriting:

$$\Gamma = 12\eta \frac{q}{\delta_{\text{slot}}^3} - \rho g \sin(\phi) \tag{5.5}$$

The *parabolic* velocity profile of equation 5.3 is usually called *Poiseuille* flow.

Most coated fluids, however, are not satisfactorily described by the Newtonian model. In most cases the viscosity itself is dependent on the magnitude of the local rate of strain. We therefore use the so called Ostwald-de Waele model (2.8) to solve equation 5.1 and find the following  $x_1$ -velocity profile:

$$v_{x_1} = \frac{1}{2} \left[ \frac{\Gamma + (\rho g \sin(\phi))}{2K} \right]^{\frac{1}{n}} \left( \frac{n}{n+1} \right) \left[ \delta_{\text{slot}}^{\frac{n+1}{n}} - (\delta_{\text{slot}} - 2y_1)^{\frac{n+1}{n}} \right] \tag{5.6}$$

$\Gamma$  is now given as:

$$\Gamma = 2K \left[ 2 \left( \frac{2n+1}{n} \right) \delta_{\text{slot}}^{-\frac{(2n+1)}{n}} q \right]^n - \rho g \sin(\phi) \tag{5.7}$$

Liquids with a power-law index,  $n$ , greater than unity are called shear thickening and those with  $n < 1$ , shear thinning.

## 5.2 Film-forming Zone

At the slot exit, the liquid turns direction, acquires a free surface which separates from the die at a static contact line, and then begins to flow down the slide face under the influence of gravity. As mentioned above the forming zones can influence coating quality significantly. Padday (1961) claimed that an enlargement of the distribution slot close to the slot exit (figure 5.2) improves uniformity of the coated layer(s). He argued that in conventional slide coating without slot enlargement a defect in the final coated product is often found which appears as lines parallel to the coating direction. Finite element predictions of the flow field and the free surface shape in the film-forming zone, suggest possible mechanisms for the occurrence of this defect (Kistler, 1984).

Kistler investigated the effect of flow rate, slot clearance and slot exit enlargement for a conventional die design (figure 5.2). In his simulations he used the

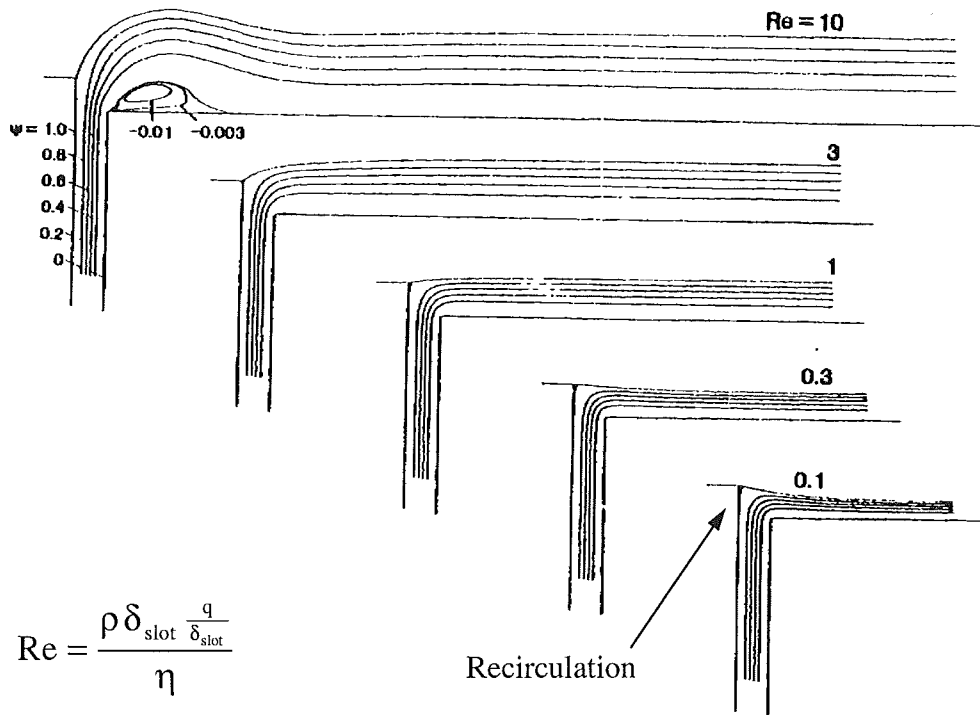


Figure 5.3: The contours of the stream function show the effect of flowrate on the flow field (Kistler, 1984).

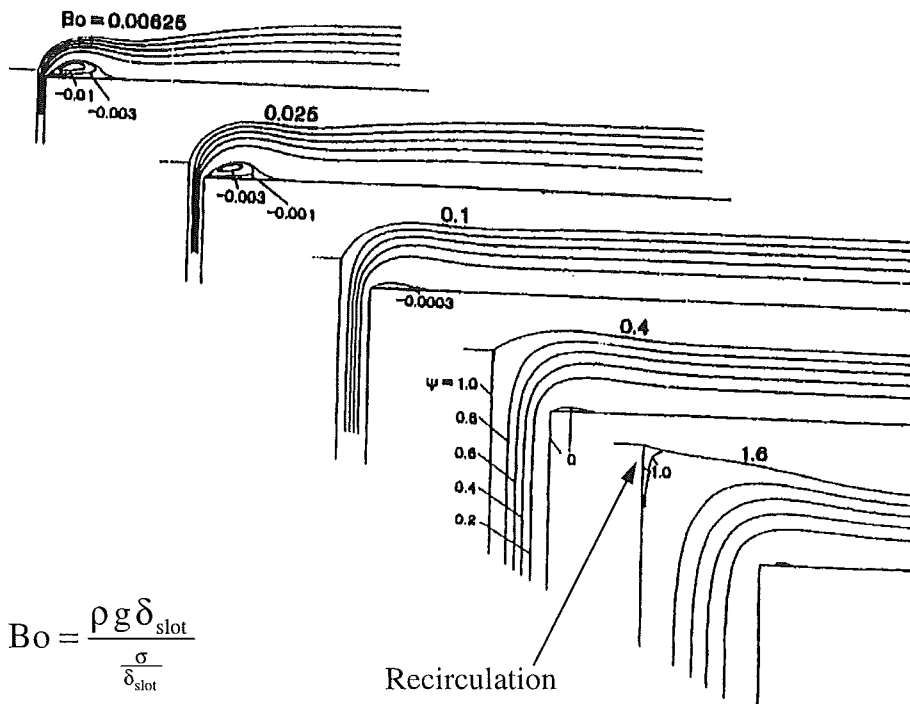


Figure 5.4: The contours of the stream function show the effect of varying the slot clearance on the flow field (Kistler, 1984).

slot clearance,  $\delta_{\text{slot}}$ , as the characteristic length scale and the average velocity in the slot,  $q/\delta_{\text{slot}}$ , as the characteristic velocity and found:

- At low flow rates, when the final film thickness,  $\delta_{\text{film}}$ , is smaller than or comparable to the step height,  $r_H = H_0/\delta_{\text{slot}}$ , he found that a small recirculating eddy forms just at the static attachment line (figure 5.3). As the pumping rate is increased, the separation angle (definition see figure 5.2) becomes larger; the eddy at the contact line shrinks and eventually disappears. However, above a certain flow rate the flow turning around the sharp corner separates from the surface of the inclined slide, thereby driving another slowly circulating eddy. The film thickness passes through a maximum and minimum and eventually approaches to its final value,  $\delta_{\text{film}}$ .
- Flow field and free surface shape change in similar fashion when the slot clearance is varied (figure 5.4). For slot clearances,  $\delta_{\text{slot}}$ , larger than or comparable to the final film thickness, there is an eddy in the region of slow flow close to the static attachment line. For slot clearances much smaller than the final film thickness, there is a slowly circulating eddy of substantial size where the flow separates from the solid at the sharp corner. Again the film thickness passes through a maximum and minimum before it decays to its final value downstream; and the separation angle can be close to  $180^\circ$ .
- Variation of the slot enlargement,  $r_E = \delta_{\text{slot,E}}/\delta_{\text{slot}}$ , and the step height,  $r_H$ , strongly influences the separation angle (figure 5.5). Kistler found that preferred slot exits should be so designed as to yield as small a separation angle as other design criteria permit.

The above examples clearly show that coating defects are caused by recirculation zones, which can be identified using two dimensional flow simulations. For more detailed die design, however, one should extend the analysis to three dimensional configurations.

### 5.3 Film-flow Zone

On the slide face, the liquid film, if it is stable, attains fully developed *Nusselt* flow, i.e. a *semiparabolic* velocity distribution which is devoid of upstream influence (figure 5.2). The final film thickness is now found by solving:

$$\frac{d\tau_{y_2x_2}}{dy_2} = \rho g \sin(\alpha)$$

5.8

The appropriate boundary conditions are: no-slip at the slide face and zero shear at the free surface.

Assuming Newtonian liquid behaviour, solution of equation 5.8 yields the following  $x_2$ -velocity profile:

$$v_{x_2} = \frac{\rho g \sin(\alpha)}{2\eta} (2\delta_{\text{film}} y_2 - y_2^2)$$

5.9

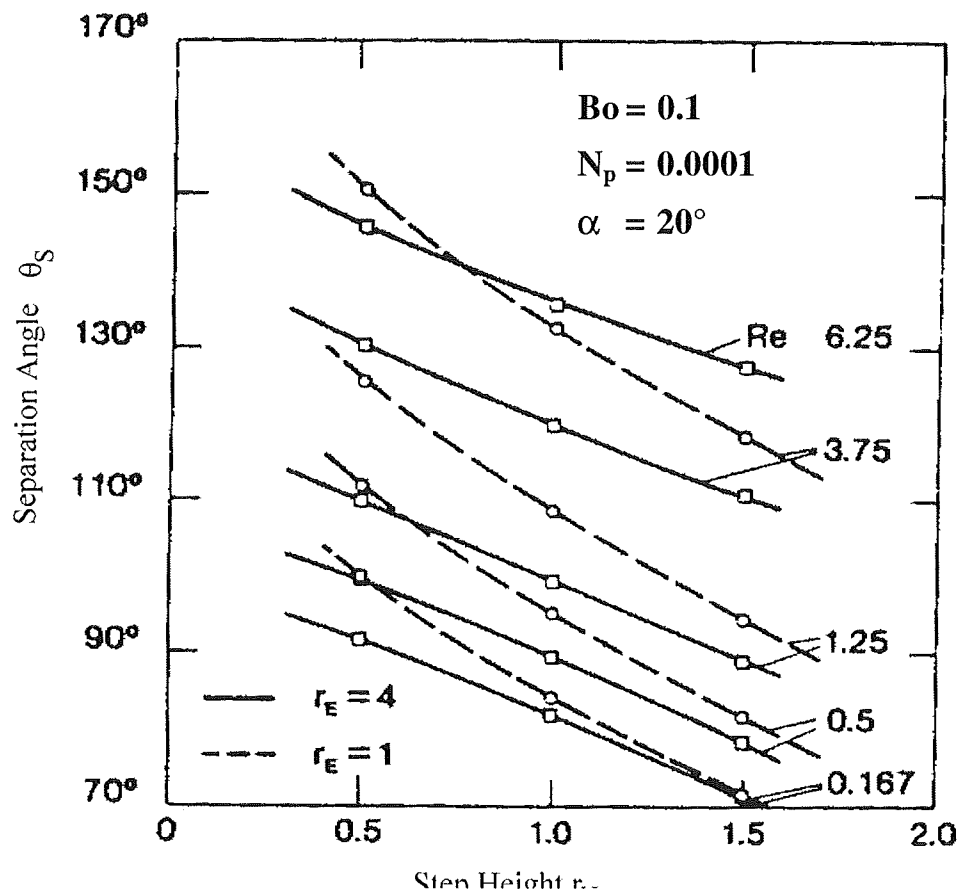


Figure 5.5: The effect of step height and Reynolds number on the separation angle  $\theta_s$  (Kistler, 1984).

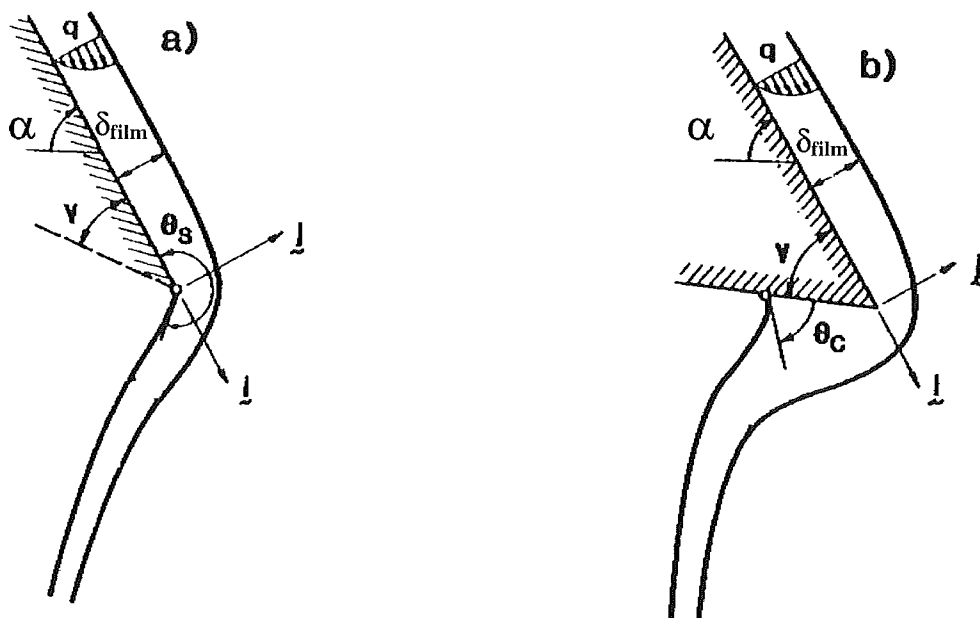


Figure 5.6: Two-dimensional flow of viscous film falling from the lip of an inclined plate to form an unsupported liquid sheet, or curtain: a. no wetting, i.e. the contact line pinned at sharp edge; b. with wetting, i.e. contact line free to migrate (Kistler, 1984).

where  $\delta_{\text{film}}$  is the final film thickness on the slide. The shear-stress profile is calculated according to:

$$\tau_{y_2 x_2} = -\rho g \sin(\alpha)(\delta_{\text{film}} - y_2) \quad 5.10$$

The unknown value for  $\delta_{\text{film}}$  in equations 5.9 and 5.10 is found when equating the flow rate per meter die width,  $q$ , to the integral of the  $x_2$ -velocity profile over the final film thickness on the slide and rewriting:

$$\delta_{\text{film}} = \left( \frac{3\eta}{\rho g \sin(\alpha)} \frac{q}{n} \right)^{\frac{1}{3}} \quad 5.11$$

The calculated shear-stress profile can be used to obtain an estimate for the range within which experiments should be done to determine the correct values of the consistency and the power law index for the Ostwald-de Waele model. When this model is used the  $x_2$ -velocity profile is given as:

$$v_{x_2} = \left( \frac{\rho g \sin(\alpha)}{K} \right)^{\frac{1}{n}} \left( -\frac{n}{n+1} \right) \left[ (\delta_{\text{film}} - y_2)^{\frac{n+1}{n}} - \delta_{\text{film}}^{\frac{n+1}{n}} \right] \quad 5.12$$

and the final thickness of the film as:

$$\delta_{\text{film}} = \left( q \left( \frac{2n+1}{n} \right) \left( \frac{\rho g \sin(\alpha)}{K} \right)^{-\frac{1}{n}} \right)^{\frac{n}{2n+1}} \quad 5.13$$

the shear-stress profile is calculated with equation 5.10.

## 5.4 Sheet-forming Zone

Around the die lip, the liquid changes direction and falls off the die, acquiring a second free surface which separates from a static contact line. This flow is important in curtain coating for the following reason. Whether a contact line remains pinned at a sharp edge, as in figure 5.6a, or whether it is free to migrate, as in figure 5.6b, can critically affect product uniformity. The flow in figure 5.6 is a fluid mechanical curiosity, for it exhibits a peculiar set of phenomena that is all too familiar from everyday occurrence.

This set of phenomena is often called the *teapot effect*, a usage reinforced by Reiner's (1956) article speculating about the physics involved. Kistler (1984) investigated these phenomena both experimentally as well as theoretically through simulations. In his simulations he used the final film thickness,  $\delta_{\text{film}}$ , as the characteristic length scale and the average velocity in that film,  $q/\delta_{\text{film}}$ , as the characteristic velocity.

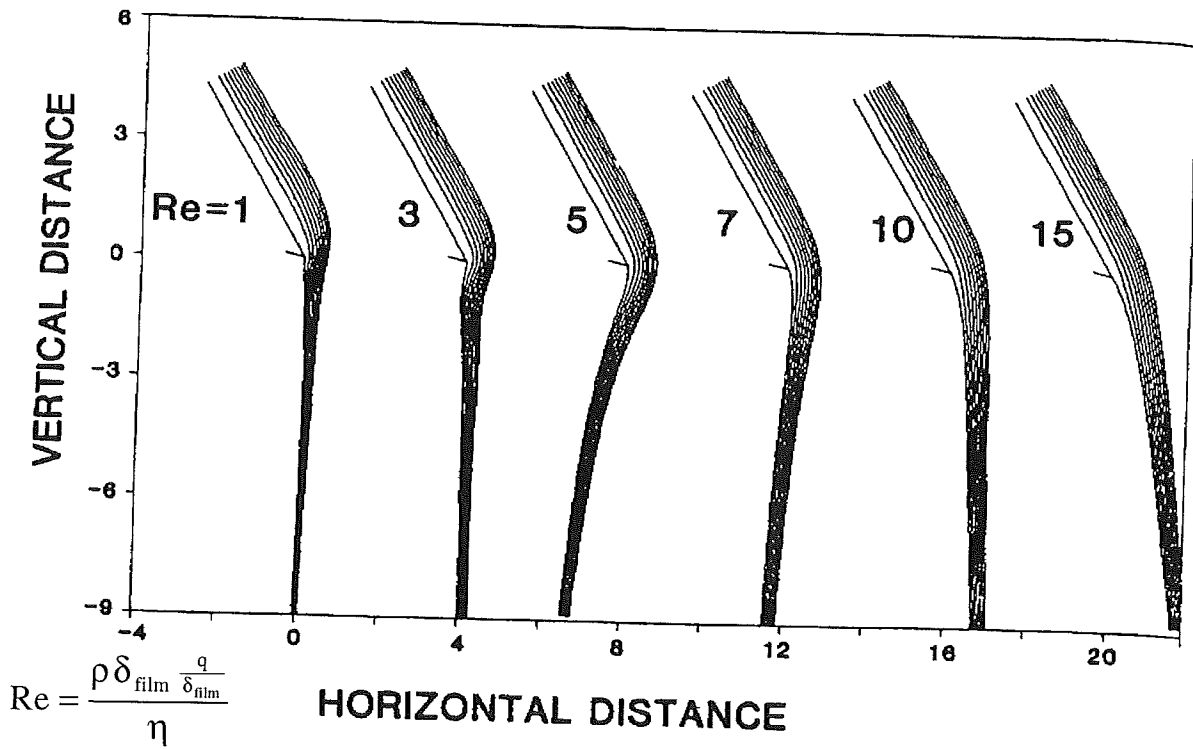


Figure 5.7: Effect of varying Reynolds number on hydrodynamic deflection of a viscous liquid curtain falling from an inclined plane (Kistler, 1984).

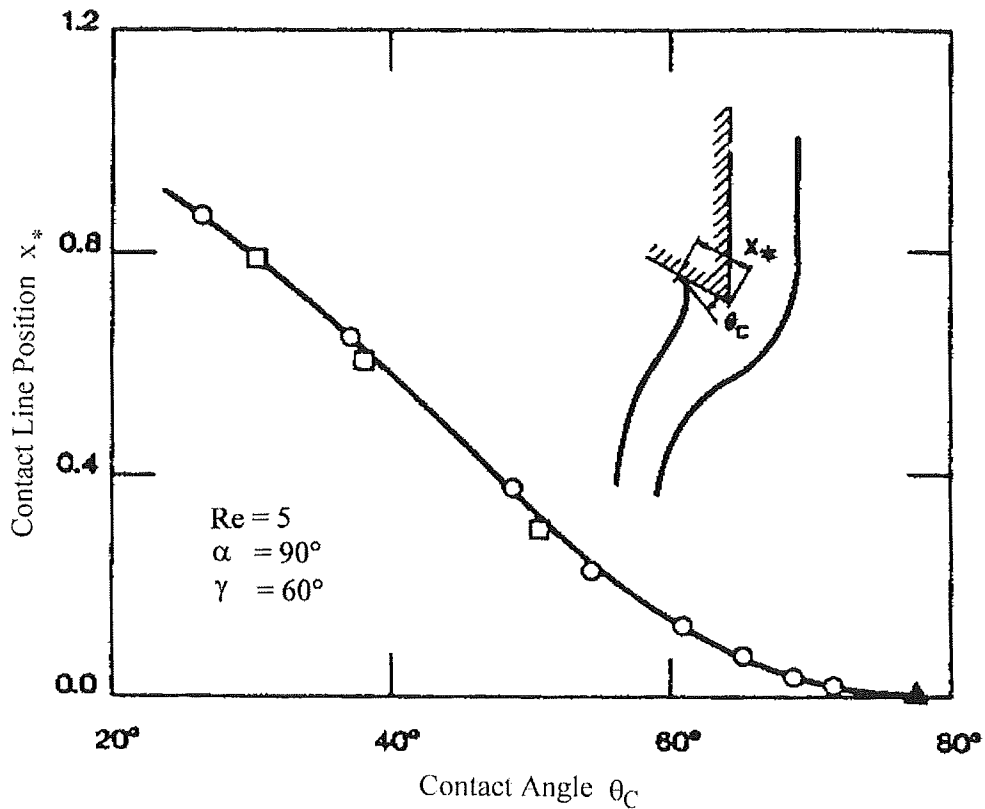


Figure 5.8: Contact line position  $x_*$  as a function of contact angle  $\theta_c$ .

From his observations it appears that the teapot effect stems from three basic mechanisms:

1. purely hydrodynamic deflection of a liquid stream;
2. contact angle hysteresis;
3. hydrodynamic hysteresis.

#### 5.4.1 Purely Hydrodynamic Deflection - Pinned Contact Line

Simulations of curtain fall from an inclined plane, when the static attachment line is pinned at the sharp die edge, reveal similar trends as observed in experiments (figure 5.7): the trajectory of the curtain is ‘ballistic’ at high flow rates, because the inertial effects dominate the flow; reverses to an ‘antiballistic’, or deflected, trajectory that passes through a maximum deflection as the flow rate decreases; and is nearly vertical at low rates, where viscous effects dominate and flow rearrangement is confined to a short forming zone. Evidently, a viscous liquid sheet falling from the lip of a plane deflects toward the underside of the lip because of the interplay of purely hydrodynamic forces, but not because of the forces that control wetting and spreading.

#### 5.4.2 Contact Angle Hysteresis - Migrating Contact Line

The foregoing paragraph leaves two fundamental questions unanswered. Under what conditions are steady-state solutions with pinned contact line stable with respect to contact line displacement away from the sharp edge? And under what conditions are only those steady-state configurations stable in which the liquid wets the lip underside?

The answers to these questions are given by figure 5.8. It shows that if the predicted static contact angle,  $\theta_C$ , is larger than a critical angle,  $\theta_C^{\text{crit}}$ , there are **no** steady-state configurations in which the underside of the lip is wet by the liquid. As the contact line position  $x_*$  is set closer and closer to zero, the predicted contact angle,  $\theta_C$ , approaches and eventually reaches  $\theta_C^{\text{crit}} = \theta_S - (180^\circ - \gamma)$ , where  $\theta_S$  is the separation angle that results when the contact line is taken to be pinned at the sharp corner and  $\gamma$  is the cut-back angle. This result implies that the contact angle does not advance over the sharp edge if the separation angle,  $\theta_S$ , satisfies the inequality condition:

$$\theta_S \leq \theta_S^{\text{crit}} = \theta_C + (180^\circ - \gamma)$$

5.14

This condition is the so-called Gibbs inequality condition (Gibbs, 1906). In the teapot flow analysed here,  $\theta_S$  is a function of the Reynolds number, the fluid properties and the inclination angle  $\alpha$ ; whereas  $\theta_S^{\text{crit}}$  depends on the contact angle  $\theta_C$ , which must be a recently advanced angle, and on the cut-back angle.

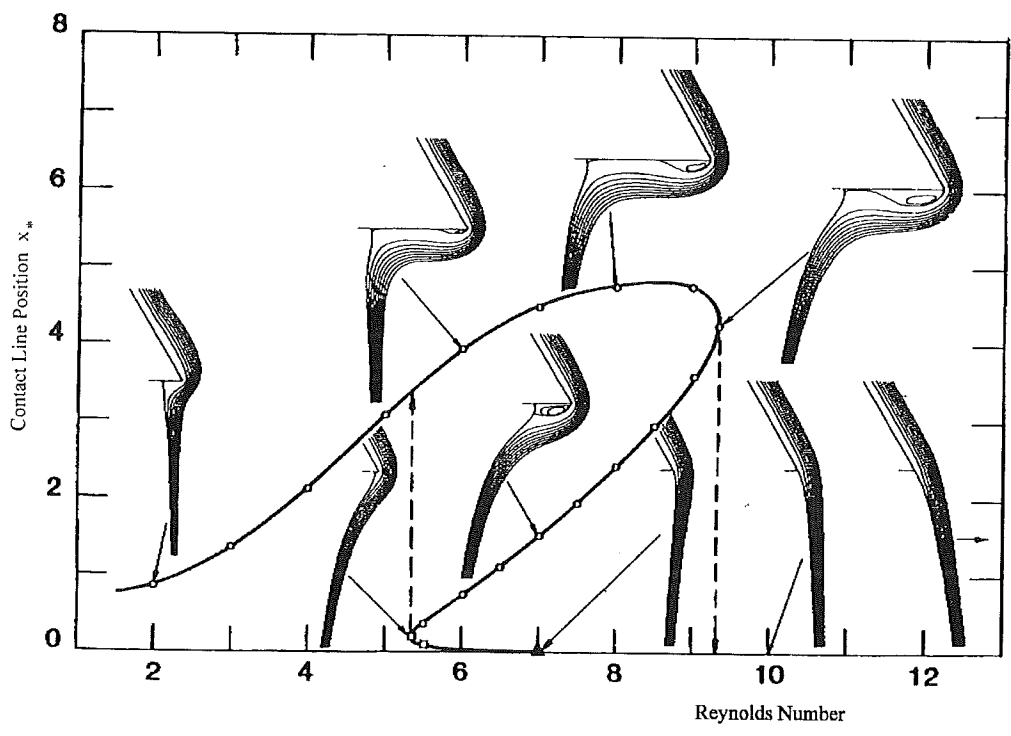


Figure 5.9: Migration of the contact line and its hysteresis (Kistler, 1984).

### 5.4.3 Hydrodynamic Hysteresis

The Gibbs inequality condition (5.14) is not a sufficient condition for the contact line to remain pinned at a sharp corner. The non-linearity in the Navier-Stokes equation makes multiple states with and without recirculating eddies possible, and these lead to hysteresis.

Figure 5.9 shows how the contact line migrates over the solid surface (for purposes of simplicity, the effects of contact angle hysteresis are ignored) as a function of the Reynolds number. At low Reynolds number, the only realisable steady state in figure 5.9 is one in which the lip underside is wet and the curtain falls almost vertically. When the sheet-forming flow is started up at a low rate, this configuration ought to be established. As the flow rate is increased, the contact line advances; the deflection of the curtain intensifies; and the flow detaches from the solid beneath the sharp edge and drives a recirculating eddy of increasing size. At the upper critical turning point,  $Re_U^{crit}$ , at which the eddy has grown so big that the main flow does not reattach at all to the lip underside, the upper turning point is reached. At any  $Re$  beyond  $Re_U^{crit}$ , the Navier-Stokes system has no steady-state, two-dimensional solutions with a free contact line. Therefore, a slight increase of flow rate beyond the critical value causes a catastrophic transition of the flow in the curtain forming zone: the separation line recedes spontaneously to the sharp edge. As the flow rate is increased even further, the contact line remains pinned at the sharp edge.

When the flow is started up at high enough flow rate that  $Re > Re_U^{crit}$ , the contact line presumably remains pinned as the flow rate is decreased until the Reynolds number reaches the critical value  $Re_S^{crit}$ , at which the separation angle no longer satisfies the Gibbs inequality condition (5.14). Decreasing  $Re$  further makes the contact line detach from the sharp edge. The contact line remains, however, close to the edge down to the flow rate that corresponds to the critical value  $Re_L^{crit}$  at the lower turning point. A slight further decrease in flow rate triggers another catastrophic transition that re-establishes the flow on the upper branch with substantial wetting and a large recirculating eddy. The coating liquid trapped in these eddies can gel or dry out, thereby causing streaks, or can discharge intermittently to appear as defects in the coating.

Owing to this hydrodynamic hysteresis, described above, the flow field and especially the contact line position, depend not only on the flow parameters, the lip shape, and the wetting characteristics of the lip underside, but also on the way the flow state was established.

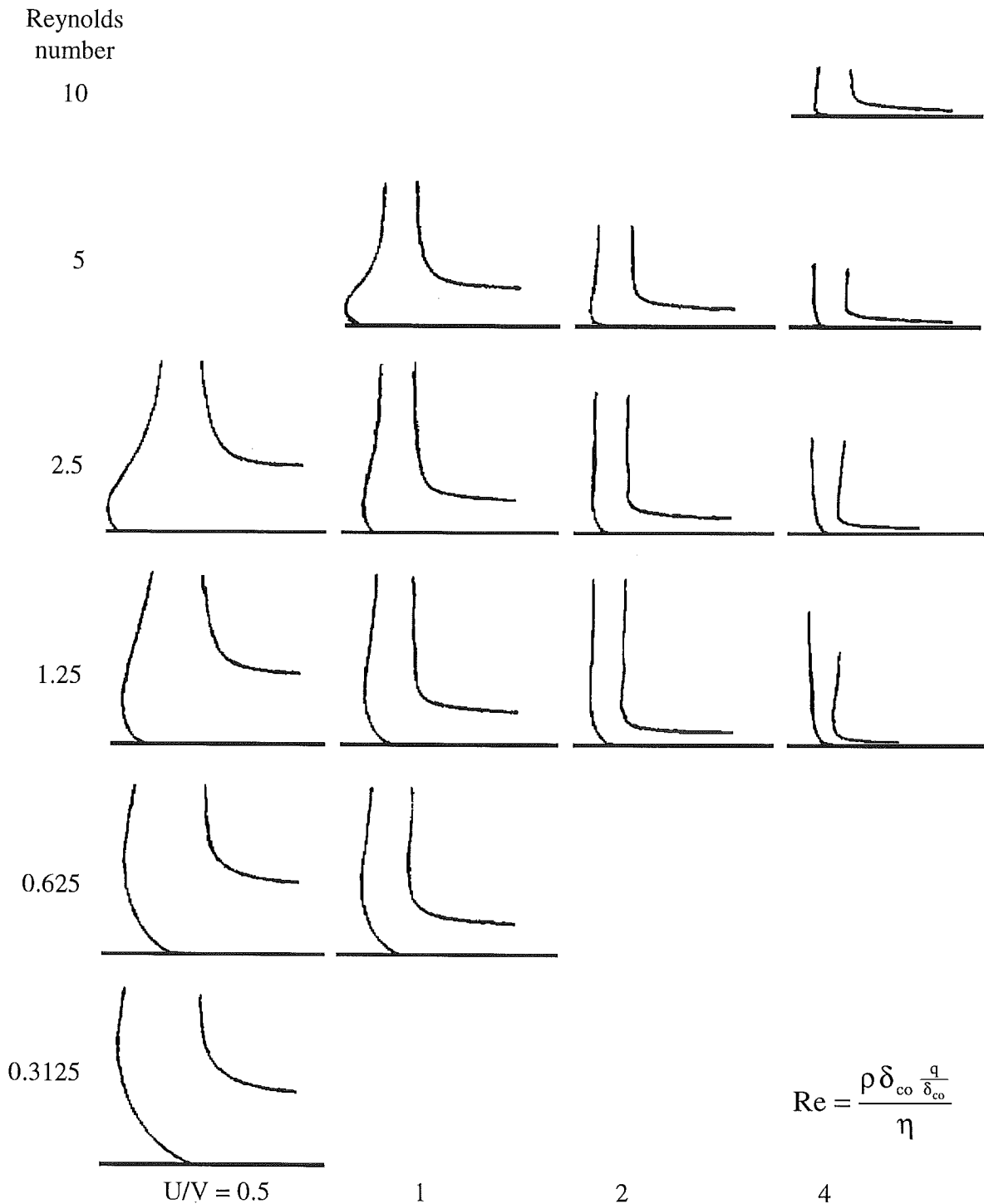


Figure 5.10: A provisional coating window (Kistler, 1984).

## 5.5 Curtain-flow Zone

Beyond the lip, the falling liquid sheet approaches an extensional flow regime in which acceleration by gravity contends with upstream influence through normal viscous stress. Brown (1961) measured the velocity within a curtain falling from a slot by means of a rotating mirror that projected the trajectories of bubbles in the falling liquid sheet. He found that the curtain reaches a free-fall regime a short distance below the slot exit and proposed an empirical formula for the curtain velocity,  $V$ , as a function of the vertical co-ordinate,  $Y$ , in the form of a free-fall parabola that starts from the point  $Y_0$  below the slot:

$$V^2 = V_0^2 + 2g[Y - Y_0]$$

5.15

In this formula,  $V_0$  is the average velocity at the slot exit. For slide curtain coating, however, the average velocity of the fully developed velocity profile (5.9) and (5.12) may be used. The distance  $Y_0$  is taken to be (Brown, 1961):

$$Y_0 = 2 \left( \frac{4\eta}{\rho} \right)^{\frac{2}{3}} g^{-\frac{1}{3}}$$

5.16

When  $Y$  exceeds a few centimetres, which is usually the case in industrial practice (table 1.1) the influence of the initial distance and velocity are negligible.

Thus far, the formation and free fall of the curtain has been discussed independently of the impingement flow downstream. In certain flow regimes, however, capillarity can transmit a significant amount of upstream influence from the impingement region, and 'pull' the curtain in the direction of the substrate motion, resulting in a bent trajectory toward the substrate. This so-called 'pulled-film' phenomenon is observed when the flow rate is low or the curtain height is small.

## 5.6 Impingement Zone

The falling liquid sheet, or curtain, impacts onto the moving substrate that is being coated in the so-called *impingement zone*. Here the flow abruptly changes direction and displaces the gas previously in contact with the substrate; furthermore one of the free surfaces terminates in a dynamic wetting line. This 'coated-film-forming' zone is the heart of curtain coating, for it largely controls the operating behaviour of the process.

Kistler (1984) was the first to investigate the evolution of free-surface shape and associated flow field in the impingement region. He did so by performing finite-element calculations in the limit that viscous forces dominate capillary forces, i.e. for very high capillary numbers. Here the Reynolds number,  $Re = q/v$ , and the ratio of the substrate speed  $U$  to the impingement speed  $V$  become the dominant parameters.

Figure 5.10 shows an example of a provisional 'coating window', which synthesises computed predictions of free surface shapes in the impingement zone.

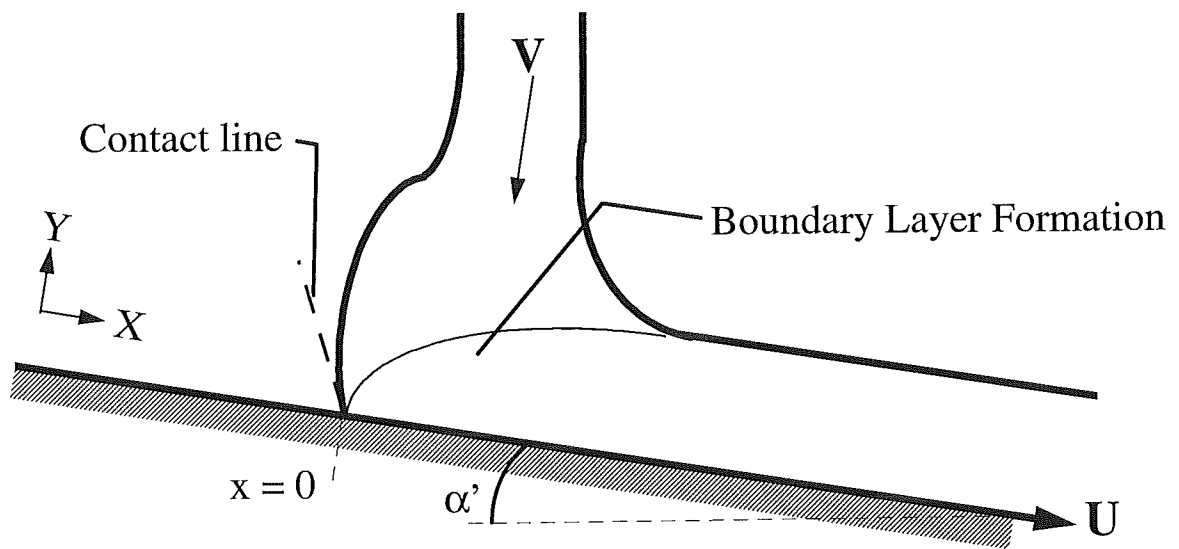


Figure 5.11: Boundary layer formation.

The following flow configurations can be attributed to certain combinations of Reynolds number and velocity ratio,  $U/V$ :

For a combination of *small*  $U/V$ , i.e. at very low web speed or for a relatively long curtain, and *small*  $Re$ , i.e. at low flow rate or high viscosity, the dynamic wetting line tends to get pulled underneath the impinging curtain, resulting in massive air entrainment. Upon increasing  $Re$ , i.e. for higher flow rate or lower viscosity, at fixed  $U/V$  a heel forms. Eventually this heel becomes too large and one or several recirculations form upstream of the impinging curtain. These eddies may trap bubbles or degraded particles of the coating solution, which in turn can cause coating streaks. Large heels may also be susceptible to various instabilities, including instabilities that result in periodic flow structures in the cross-web direction.

When increasing  $U/V$ , i.e. at high web speed or for small curtains, at fixed  $Re$ , on the other hand, the curtain will again be pulled, leading to air entrainment. At high web speed and high flow rate, air is entrained excessively beneath the heel.

The pulled film configuration and the limit of air entrainment, pose lower and upper speed limits for successful curtain coating. These and other coating window related aspects will be discussed below.

### 5.6.1 Boundary Layer Analysis of the Impingement Flow

The flow field for curtain coating is not very complicated, its essential features can be captured using a relatively simple, macroscopic model. Kistler (1984) explained how the position of the dynamic wetting line and the closely related size of the heel can be estimated from a boundary-layer theory for moving flat surfaces (Sakiadis, 1961). This theory however only applies in cases of high capillary or Weber numbers, i.e. when surface tension is negligible. Blake, Clarke and Ruschak (1994) extended Sakiadis' analysis to account for these surface tension effects.

The boundary layer (figure 5.11) begins at the dynamic wetting line, where the liquid contacts the substrate, and grows in thickness until all of the supplied liquid has been entrained. The end point of the envelope of the boundary layer is assumed to lie on the front free surface of the curtain. If the point were located internally, there would be a region of recirculation adjacent to the downstream surface of the curtain, and this is not the case under the conditions considered. Both experimental as well as theoretical work support this physical picture.

For the analysis the limiting case of  $U/V \gg 1$  is considered. This implies that the contribution of pressure and extension in the x-momentum balance are negligible. The influence of the pressure generated through the impact of the curtain, however, is expected to assist acceleration of the flow. The assumptions used in the boundary layer analysis are only valid for an infinite medium. In case of flow between, e.g. two vertical plates of which one is moving, this *penetration* theory applies until (Bird, 1960):

$$\delta_M = \sqrt{\pi \nu t} < \frac{L}{2}$$

5.17

where  $\delta_M$  is the thickness of the momentum boundary layer,  $L$  a characteristic length scale, viz. the distance between the plates, and  $\nu$  the kinematic viscosity.



Since the main interest is the position of the dynamic wetting line, rather than a correct description of the flow field, penetration theory is rigorously applied without taking the assumption of an infinite medium into account.

At the surface of the substrate the no-slip condition gives boundary conditions on  $v_x$  and  $v_y$ . As an additional boundary condition the x-component of velocity outside the boundary layer approaches the x-component of the curtain impingement velocity.

Solution of the reduced Navier-Stokes equations, using the method of moments, yields the following general form for the boundary layer thickness ( $0^{\text{th}}$  moment):

$$\delta_M = C_1 \sqrt{\frac{v_x}{U}} \quad 5.18$$

The value of the constant,  $C_1$ , depends on the chosen form of the similarity velocity profile,  $\varphi(\eta)$ . The position of the dynamic contact line is now found by setting the flow in the boundary layer equal to the flow rate per metre die-width at the position  $x = L_\delta$ , where the boundary layer hits the front free surface of the curtain. After rewriting the following general equation is found for  $L_\delta$ :

$$\frac{L_\delta}{\delta_{co}} = C_2 \left( \frac{q}{v} \right) = C_2 \text{Re} \quad 5.19$$

In table 5.1 three values of the constant,  $C_2$ , are given for a web inclination of  $0^\circ$  together with the similarity velocity profiles, used in the boundary layer analysis.

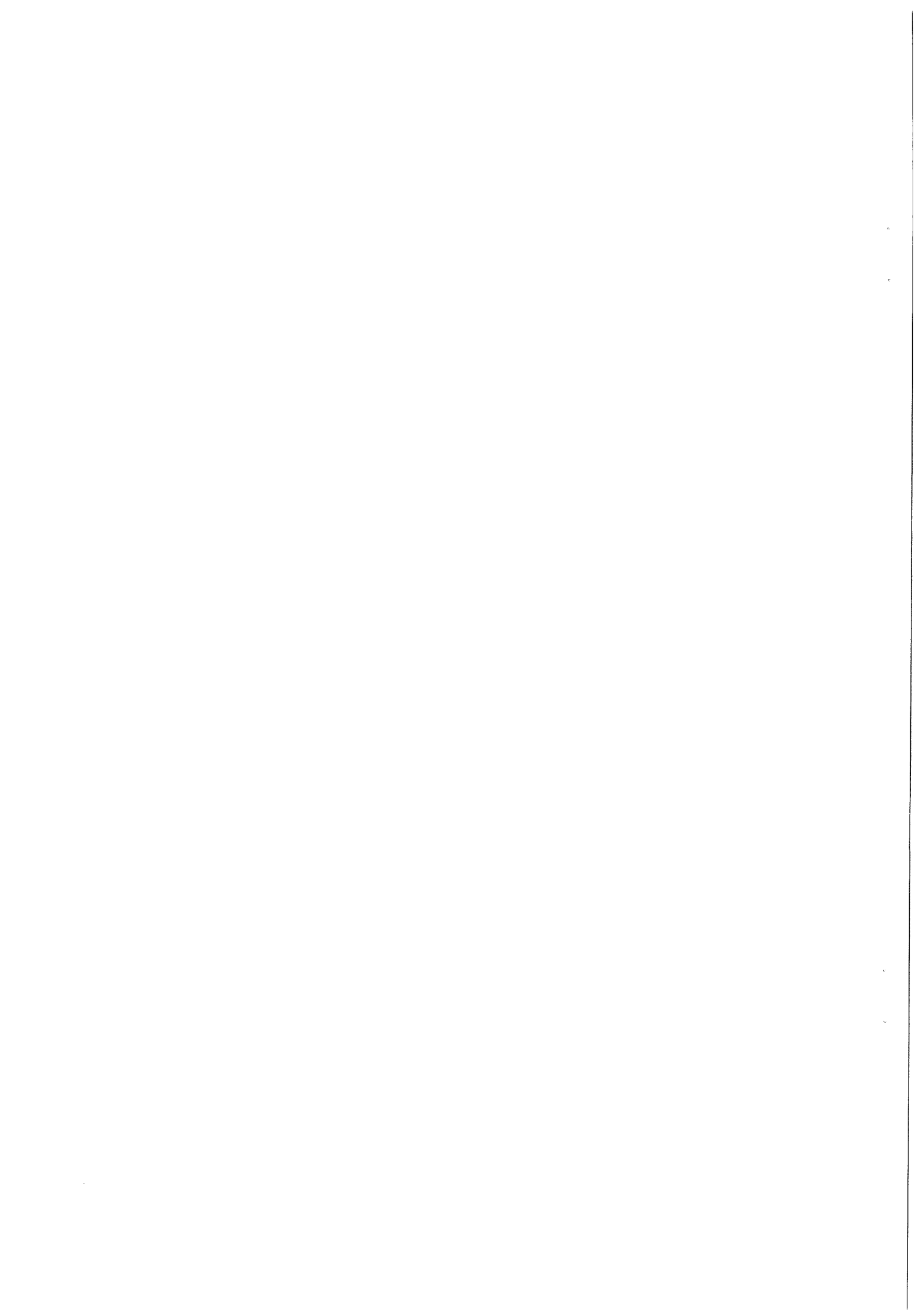
Table 5.1: Three results for the constant in boundary layer analysis and the associated similarity velocity profiles.

Method	Value for the constant $C_2$	$\varphi(\eta)$
Sakiadis	0.383	-
Blake, Clarke and Ruschak	0.45	$1 + (\eta^2 - 2\eta)$
Author	0.559	$1 + 1/2 (\eta^3 - 3\eta)$

The range of values for the constant  $C_2$  stresses the fact that the equation for the position of the dynamic wetting line is only an estimation. The basic relationship can, however, be used to correlate data. Another shortcoming of this analysis is the fact that the wall shear stress becomes very high in the vicinity of the dynamic wetting line and reaches infinity in this point:

$$\tau_{yx} = C_3 \eta U \sqrt{\frac{U}{v_x}} \quad 5.20$$

In practice Weber numbers are of order unity or smaller and surface tension effects are usually appreciable. Because of the expected curvatures of the interfaces near the boundary layer, we expect surface tension to increase pressure where the boundary layer begins and decrease pressure where the boundary layer ends. Consequently, there should be a negative pressure gradient that shortens boundary layer length.



Taking this pressure gradient into account yields for the dynamic contact line position (Blake et al. 1994):

$$\frac{L_{\delta}}{\delta_{co}} = \frac{3}{20} \frac{(3+2\omega)}{(1+2\omega)^2} \left[ 1 - \frac{30C_4}{(1-\omega)(3+2\omega)} \right] \text{Re} \quad 5.21$$

Where  $\omega$  is the velocity ratio:  $V/U \sin(\alpha')$  and  $\alpha'$  the angle of web inclination. The constant  $C_4$  is found from an overall momentum balance:

$$C_4 = \frac{(1+2\omega)(1-\sin(\alpha'))}{3 \text{We}} \quad 5.22$$

A convenient way of quantitatively describing the position of the dynamic wetting line is as the dimensionless ratio,  $l'$ , the relative wetting line position:

$$l' = \frac{L_{\delta}}{\delta_{cu}} \cos(\alpha') \quad 5.23$$

For  $l' = 1$ , the dynamic wetting line lies in the plane of the rear surface of the curtain. When  $l'$  is less than unity, the wetting line is located further downstream, leading to air entrainment. While for  $l'$  exceeding unity, the curtain impingement zone is characterised by a heel.

Blake et al. further stated that the pressure forces, which arise from a transformation of the y-momentum of the impinging curtain into stagnation pressure, can act as a load that may delay the onset of air entrainment. Based on a balance of y-momentum, they found a maximum for the impingement pressure:

$$p_{\max} = \frac{\rho}{4} (U \cos(\alpha'))^2 \quad \text{for} \quad L_{\delta} = \frac{2\delta_{cu}}{\cos(\alpha')} \quad 5.24$$

In other words, the optimum position of the relative wetting line, according to this criterion, is 2. In practice, the optimum relative wetting line position usually lies in the range of  $1 < l' < 2$  (Schweizer, 1997). The momentum of the impinging curtain typically postpones visible air entrainment to substrate speeds ten times as high as those of plunging continuous surfaces.

## 5.7 Take-away Zone

The coated liquid film approaches and ultimately attains the fully developed plug flow of solid body translation at the substrate speed in the so-called take-away zone. In this zone there is no upstream influence, as a rule of thumb it is attained at a distance approximately eight times the curtain thickness (Grald, 1997).

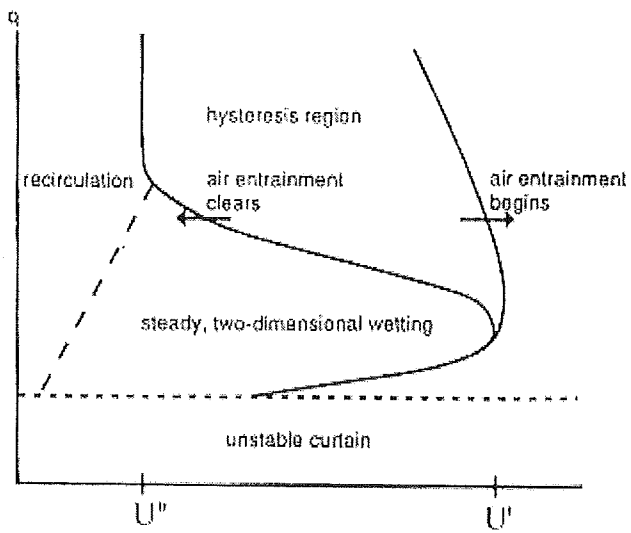


Figure 6.1: A plot of the flow rate per meter die-width versus web speed showing the different regimes encountered in curtain coating (Blake et al., 1994).

## 6. Operability - Coating Window

The analysis of the flow in curtain coating has already mentioned a few limits of coatability, e.g. the pulled film regime and visible air entrainment. The first step in a successful curtain coating operation, however, is the formation of a stable liquid curtain. At low flow rates, the liquid curtain tends to detach from the edge guides or break into individual streams. Brown (1961) analysed the stability of a falling liquid sheet. He found that to stabilise the curtain and carry away disturbances, the inertial forces of the curtain must exceed the surface forces. He found the following formula for the wavespeed of a disturbance,  $C$ :

$$C = \left( \frac{2\sigma V}{\rho q} \right)^{\frac{1}{2}}$$

6.1

Using the curtain stability criterion that the impingement speed must be greater than the wave speed of the disturbance, gives:

$$We = \frac{\rho q V}{\sigma} > 2$$

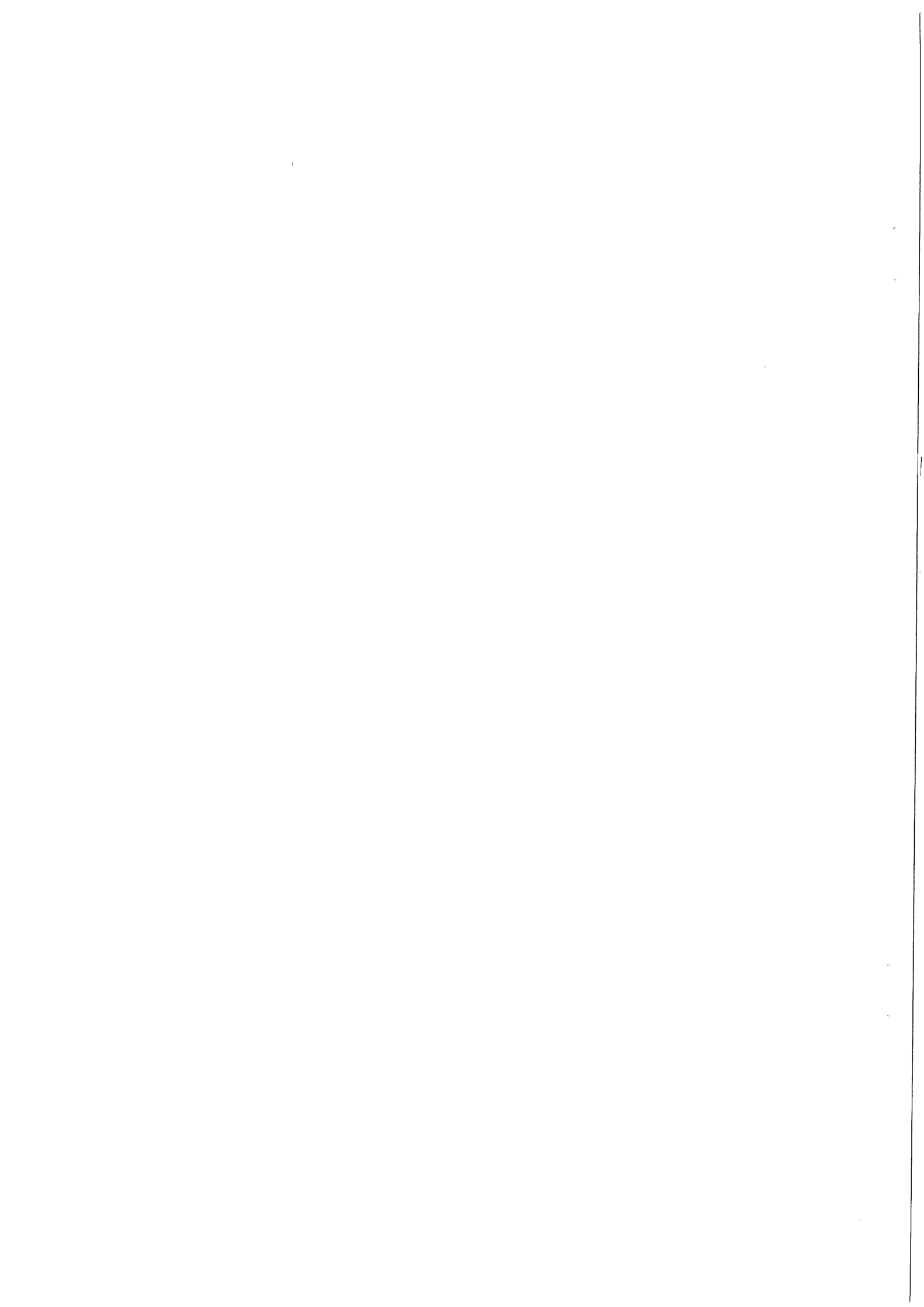
6.2

Recent theories and experiments by Do and Christodoulou (1992) and Finnicum et al. (1993), however, show that falling curtains are linearly stable regardless of the Weber number. More likely the curtain disintegrates due to edge effects. Wetting of the edge guides causes local thinning of the curtain near the edge guides which could trigger break-up. Furthermore increasing viscosity enhances damping of disturbances and thereby stabilises the curtain, at the same time, it accelerates boundary layer development along the edge guide and thereby promotes breakage of the curtain. This problem may be solved by optimising edge guide design. Another likely cause for the loss of curtain integrity comes from non-linear effects such as those arising from contaminants and bubbles in the liquid, which may become nucleation sites for holes growing in the curtain (Do and Christodoulou, 1992).

The Weber number is still a useful parameter for predicting a pulled film regime. Experimental work by Ogawa et al. (1992) indicates that liquid viscosity and coating speed have a relatively small effect on preventing film pulling. Likewise, air flow turns out to be insignificant. The way to avoid the pulled-curtain effect and thereby widen the coating window is to increase curtain height if the curtain is sufficiently stable or to lower the (dynamic) surface tension.

The analyses by Kistler (1983) and Blake et al. (1994) of the impingement zone make plain that long curtains and low-viscosity liquids are effective in delaying the onset of air entrainment. The rapid flow development near the dynamic wetting line suggests a positive effect of a shear-thinning coating liquid on delaying the onset of air entrainment (Ogawa and Scriven, 1994).

Figure 6.1 shows another complication in successful coating (the impingement speed is fixed). At very high flow rates, the speed at the onset of air entrainment either changes slowly with flow rate or approaches a constant value,  $U''$ , at which the wetting line is isolated (heel with recirculation). As the flow rate is decreased from high values, the air-entrainment speed departs from the curve for an isolated wetting



---

line and increases. At a certain flow rate, the air-entrainment speed attains a maximum value,  $U'$ , which can easily be an order of magnitude larger than  $U''$ . The air-entrainment velocity decreases to very low values as flow rate is reduced further, and the wetting line moves visibly downstream from the curtain (pulled film). At flow rates higher than that corresponding to  $U'$ , however, there may be a region of *air-entrainment hysteresis*. Whether or not air entrainment occurs at a point in this region depends on how the point is reached. If, for example, air entrainment is produced by increasing speed at constant flow rate, it will not begin until the higher-speed boundary of the region is reached. If speed is then reduced, however, air entrainment does not clear until the lower-speed boundary is reached. This region must therefore be avoided in industrial operation.



## 7. Area to be Investigated Through Simulations

The above discussion of the 7 coating zones, shows that there are several interesting areas, the so-called forming zones which greatly influence curtain stability. First the film-forming zone, which is closely related to the internal die-design. Second the sheet-forming zone and its associated teapot effect, which is closely related to the lip-design and flow rate. Finally the impingement zone, which is to a large extent related to the flow rate and the velocity ratio  $U/V$  and hence determines the limits of operability.

In this chapter the impingement zone is examined more closely. First the influence of an increase in the velocity ratio,  $U/V$ , on heel formation is studied. Second the influence of the prescribed dynamic contact angle on the position and shape of the rear free surface is examined. Aside from physical parameters there are also numerical parameters. The solution can only be considered physically realisable when it becomes independent of an increase in polynomial order and of the amount of grid refinement. Since both increasing the polynomial order and grid refinement require more computational effort, an iterative solver should be used. There might, however, be some differences in the consistency of the solution due to using this type of solver instead of a direct solver. Therefore both solvers are used for the same case and the outcome is compared.

(Please note that some of the figures in this chapter have been attached at the end of this chapter).

### 7.1 General Simulation Conditions

#### *Operating Variables*

In order to be able to simulate any process, the operating variables should be identified. The following operating variables are associated with curtain coating: webspeed, curtain height, the angle of web inclination, liquid properties and wet coating weight. All but webspeed are fixed variables in the simulations and their values are given in table 7.1.

Table 7.1: Operating variables in curtain coating.

Operating variable	Value
Curtain height	0.30 m
Angle of web inclination	0°
Liquid: Density	1000 kg·m <sup>-3</sup>
Dynamic viscosity	0.01 Pa·s
Surface tension	0.03 N·m <sup>-1</sup>
Wet coat weight	0.016 kg·m <sup>-2</sup>



Once the last degree of freedom, the web speed, is given the following dependent variables are set:

- The flow rate per meter die width, which is given as:

$$q = \frac{UM_{ct}}{\rho}$$

7.1

where  $M_{ct}$  is the wet coat weight.

- The impingement speed, given by equation 5.15.
- The final thickness of both curtain and coated film.
- The velocity ratio.

### Boundary Conditions

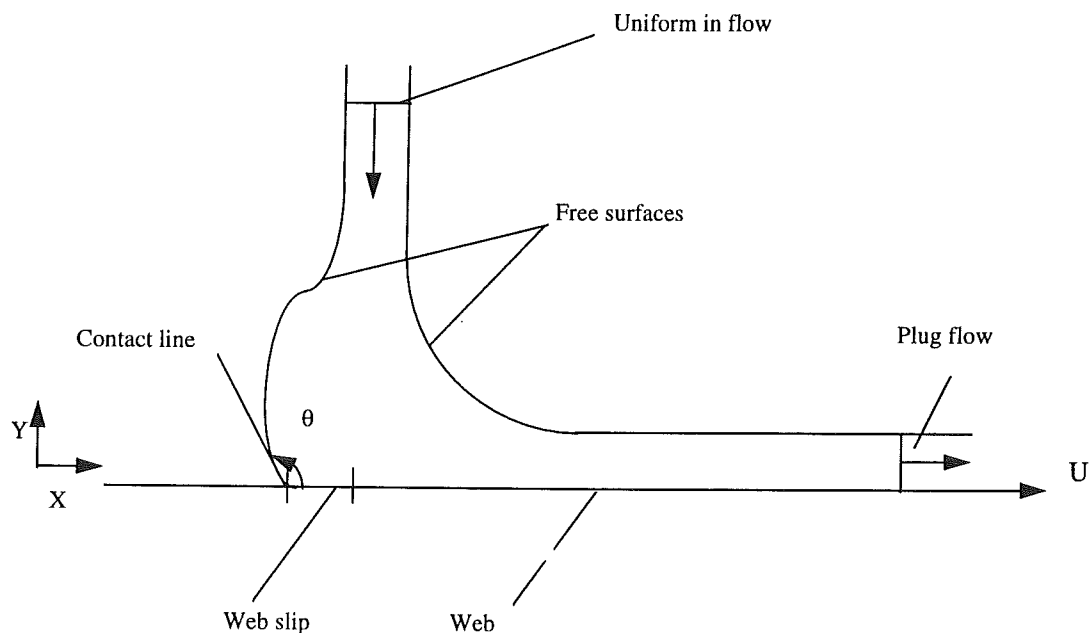


Figure 7.1: A schematic of the impingement zone and its appropriate boundary conditions.

The next step is to set the boundary conditions (figure 7.1). At some inflow plane, typically six to eight times the final coating thickness, the velocity of the inflowing curtain is taken to be uniform and known. The outflow boundary is placed far enough downstream, also typically six to eight times the curtain width at impact, where the coated film has attained fully developed plug flow of solid body translation at the substrate speed (Grald, 1997). The web is buildup of two parts: the web slip part, where the velocity is set equal to the coating speed,  $U$ , and the mesh is treated as sliding because the dynamic contact point needs to move over it; and the web part, which is the same except for the mesh which is not considered to slide. Due to the fact that the web slip part is sliding, the size of this region may vary.

At a  $U/V$  of 1.4 two simulations were done: a. where the boundary condition on the web slip area was taken to be that of free slip, i.e. all gradients are set equal to zero at this boundary; b. where the usual no-slip boundary condition was applied. The size of this free slip area is 0.74 times the final curtain thickness.



The dynamic contact angle, defined as the angle between the web slip zone and the contact line is measured through the fluid and fixed at  $145^\circ$ , unless mentioned differently. Table 7.2 compares the basic properties of all the meshes to be used below.

Table 7.2: Basic properties of the meshes used to simulate the impingement zone.

Web slip condition	free slip	no-slip	no-slip	no-slip	no-slip
Number of elements	54	54	54	54	126
Element order	4	4	6	8	4
Number of nodes	933	933	2047	3593	2109
Total number of nodes	1350	1350	2646	4374	3150

The total number of nodes includes the extra nodes introduced through interpolation. Figure 7.2 to figure 7.5 show magnifications of these grids in the heel region. The average linear dimension of the cells close to the dynamic contact point (dcp), the linear dimensions of the cell in this point and the aspect ratio of the cell in this point are listed in table 7.3.

Table 7.3: Average linear dimensions and those in the dynamic contact point for all meshes used.

Number of elements	54	54	54	126
Element order	4	6	8	4
Total number of nodes	1350	2646	4374	3150
Average cell dimension [ $\mu\text{m}$ ]	4.2	2.8	2.1	2.2
x-dimension of cell in the dcp [ $\mu\text{m}$ ]	3.2	1.5	0.9	1.6
y-dimension of cell in the dcp [ $\mu\text{m}$ ]	0.8	0.4	0.2	0.3
Aspect ratio of the cell in the dcp	4.0	3.9	4.5	5.5

### Models

The next step is to define the models NEKTON has to apply in the calculations. Steady two dimensional fluid flow is chosen; the geometry is allowed to move since we are dealing with deforming boundaries, i.e. free surfaces. The convection term in the Navier Stokes equations (advection in NEKTON) is taken into account, because  $Re > 1$  (see table 2.1 for definition). When the mesh geometry is deformable or when a non-Newtonian fluid viscosity is used or if there are traction BC's applied on any fluid boundary the option stress formulation must be selected. This means that the full symmetric stress tensor is used in the calculations.

### Solvers

Once the models are known the solver has to be chosen. In this thesis either the direct or the iterative coupled velocity-pressure solver is used. The relaxation parameters for geometry and velocity-pressure are kept at their default value of unity. The convergence of the different iteration steps is judged based on the convergence criteria listed in table 7.4.



Table 7.4: Convergence criteria for the different iteration steps used in NEKTON.

Solution Criteria	Max. relative change in velocity	0.001
	Max. relative change in geometry	0.0001
	$V_n/V$	0.01
Residual Criterion	v-p tolerance	0.0001



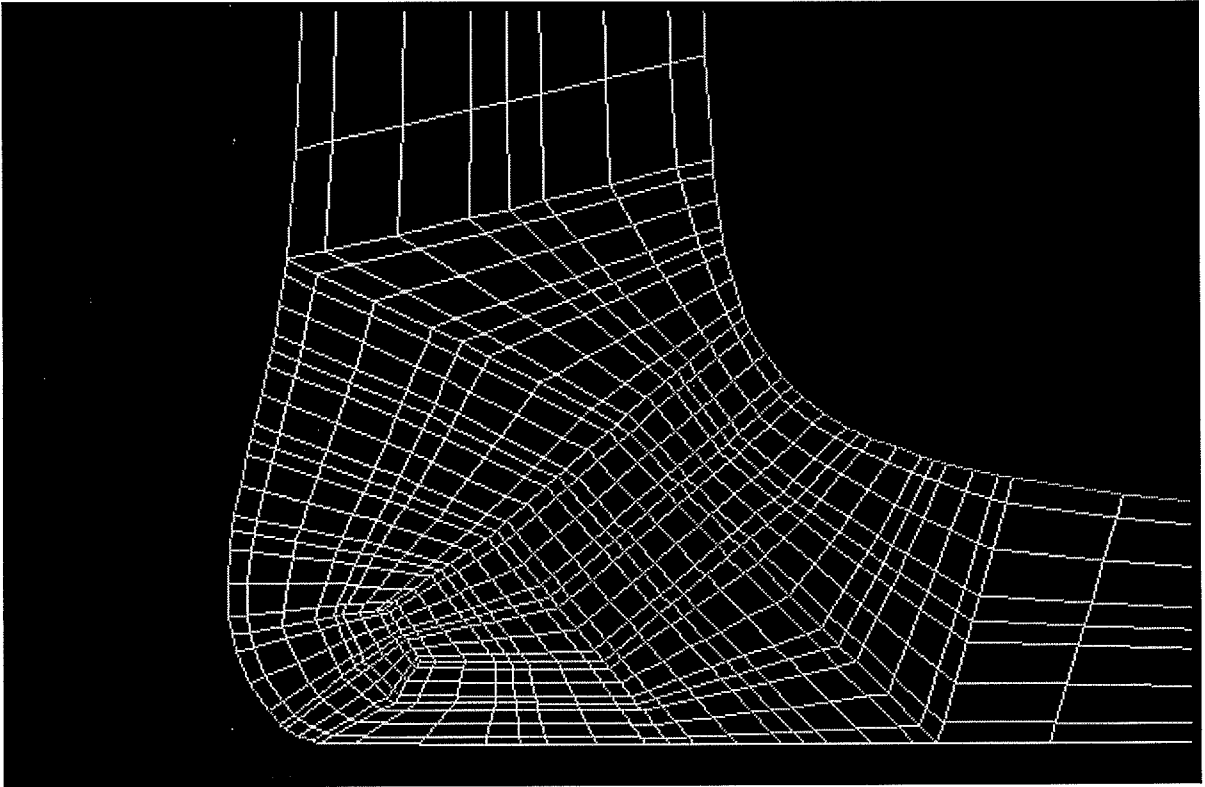


Figure 7.2: The grid in the heel region, for a fine mesh of order 4.

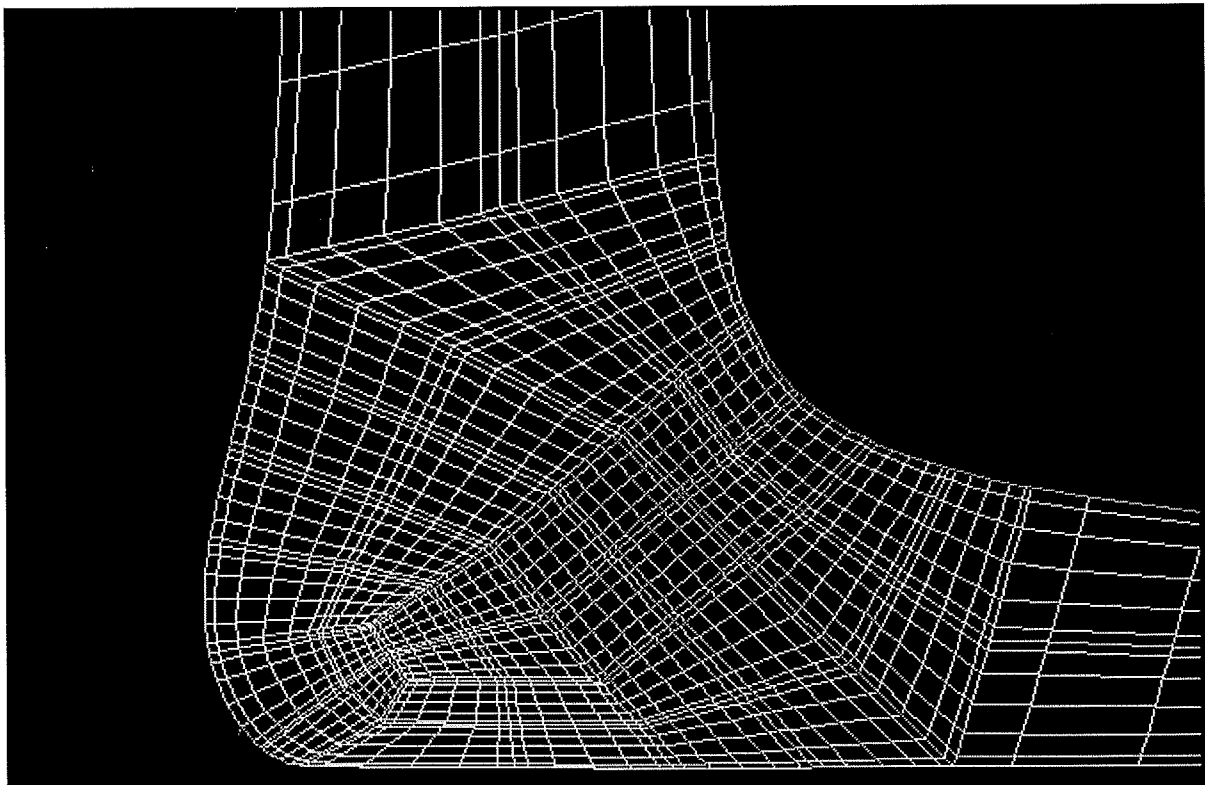


Figure 7.3: The grid in the heel region, for a coarse mesh of order 6.



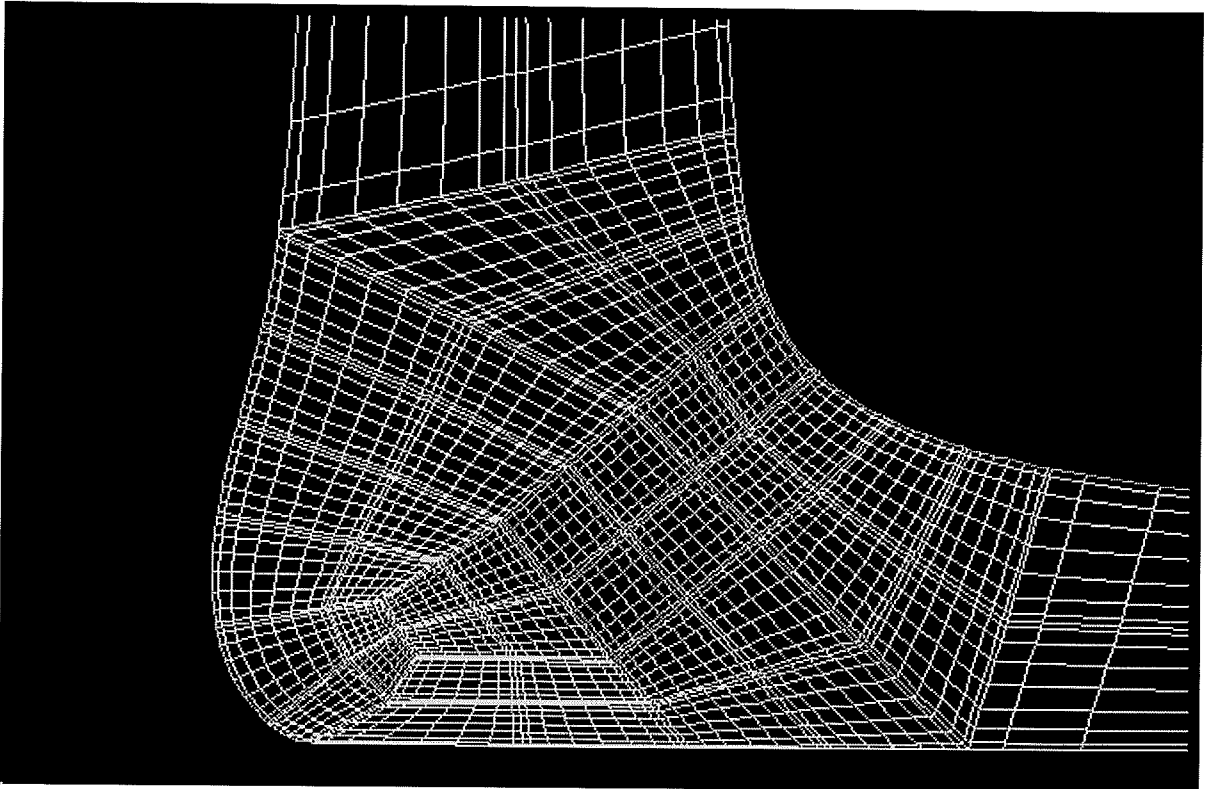


Figure 7.4: The grid in the heel region, for a coarse mesh of order 8.

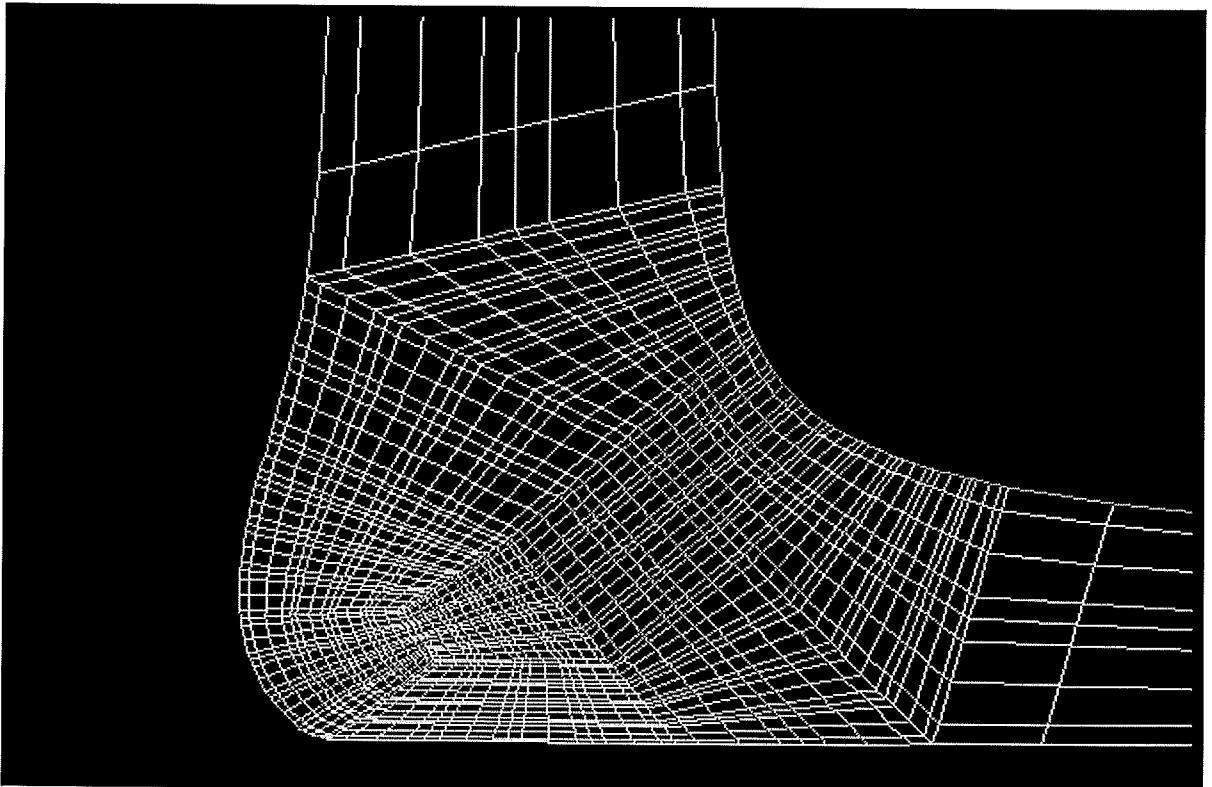


Figure 7.5: The grid in the heel region, for a fine mesh of order 4.



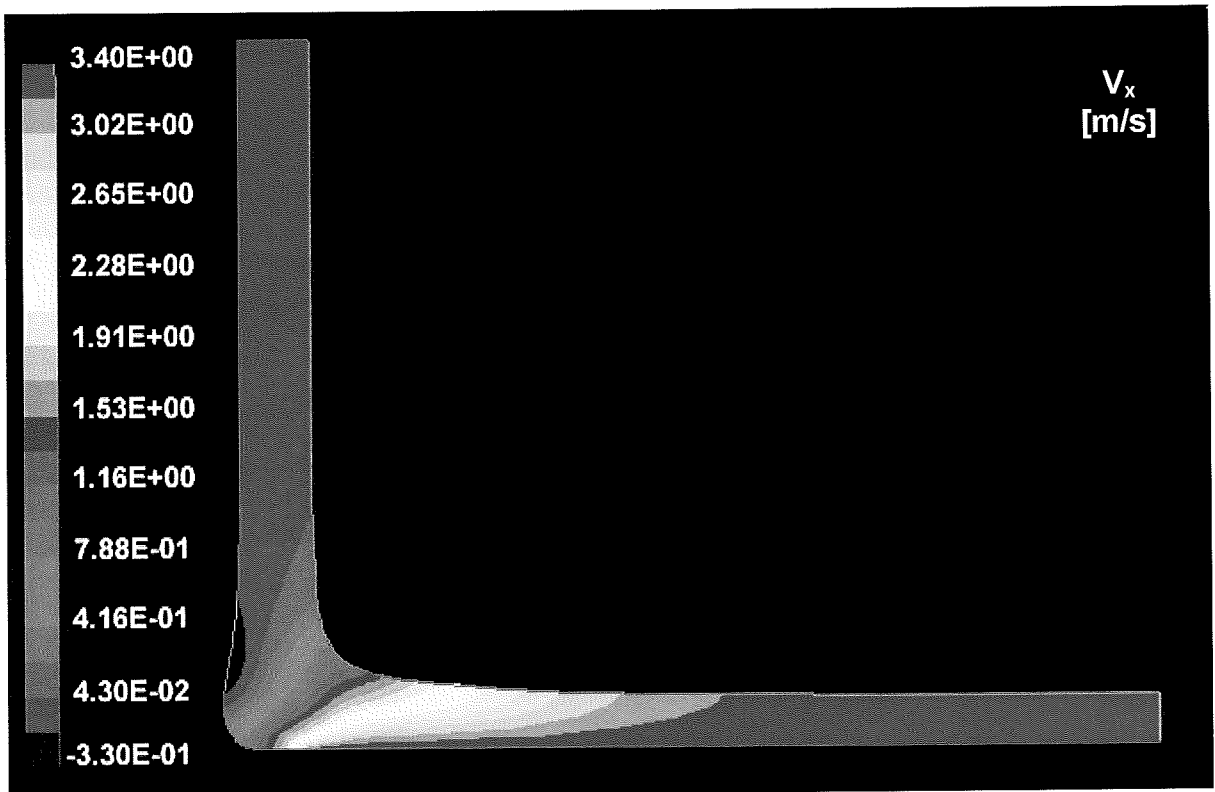


Figure 7.6: Contours of x-velocity when applying the no-slip condition (coarse mesh,  $n = 4$ ).

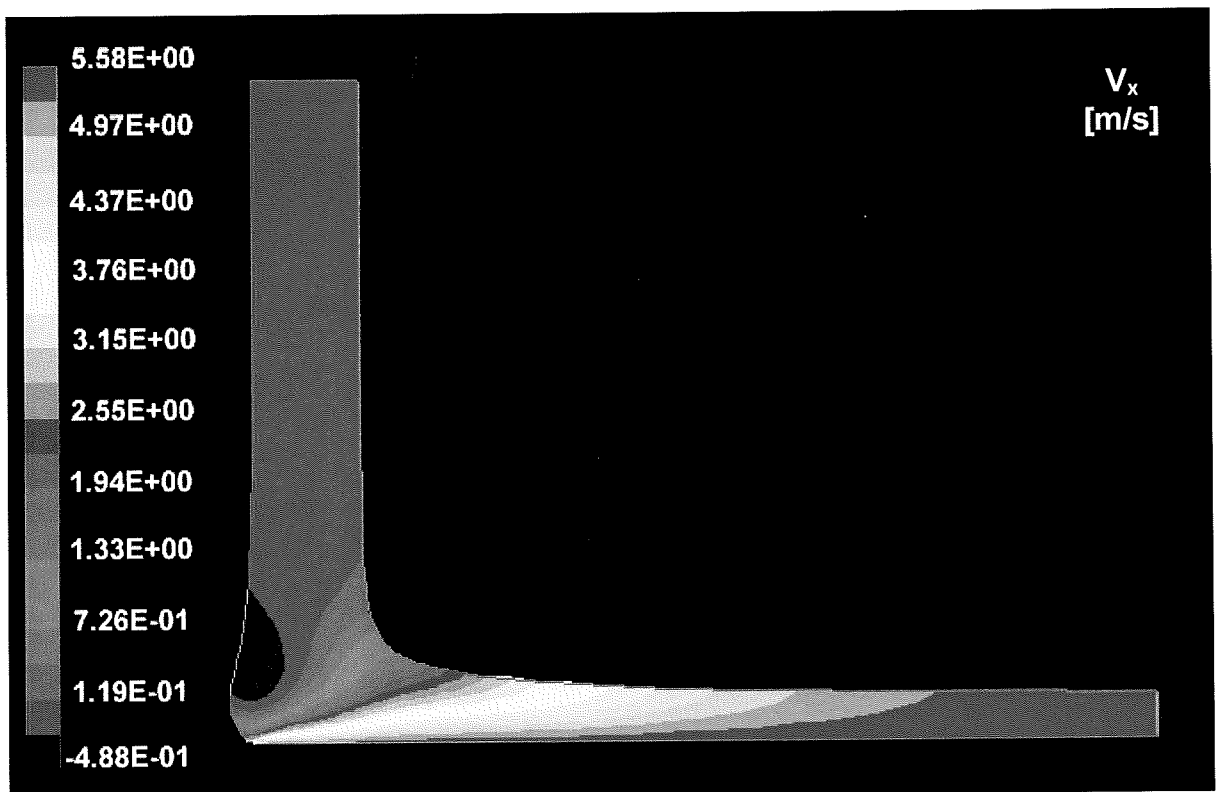


Figure 7.7: Contours of x-velocity, when using a region of free slip (coarse mesh,  $n = 4$ ).



## 7.2 Parameter Studies Of the Curtain Coating Process

In order to find the operating window of curtain coating we should examine the governing equations and chose the appropriate length scales for the dimensionless numbers. Kistler (1984) suggested the following for impingement flow: length is measured in units of  $\delta_{cu}$ , the ultimate thickness of the impinging curtain; the velocity in units of  $U$ , the coating speed. Both pressure and stress are measured in units of  $\eta U / \delta_{cu}$ , where  $\eta$  is the viscosity of the fluid. For laminar, steady, two dimensional coating flows considered in this thesis equation 2.9 reduces to:

$$\text{Re} \left( \frac{U}{V} \right) \mathbf{v}^* \cdot \nabla^* \cdot \mathbf{v}^* = -\nabla^* p^* - \nabla^* \cdot \boldsymbol{\tau}^* + \text{St} \left( \frac{U}{V} \right)^2 \mathbf{f}$$

7.2

The choice of taking  $\delta_{cu}$  as the characteristic length is useful because it incorporates two important parameters, which characterise the flow: the premetered flow rate and the impingement velocity. On the other hand the resulting Reynolds and Stokes number are based on the 'wrong' length scale. Therefore Kistler redefined the dimensionless numbers (table 2.1) in equation 7.2 and those important for choosing the solution algorithm in NEKTON.

Table 7.5: Dimensionless groups measuring ratios of competing forces in the impingement zone.

Dimensionless Group	Definition	Ratio of
Reynolds Number	$\text{Re} \equiv \frac{\rho q}{\eta}$	$\frac{\text{Inertial force}}{\text{Viscous force}}$
Stokes Number	$\text{St} \equiv \frac{\rho g q^2}{\eta U^3}$	$\frac{\text{Gravity force}}{\text{Viscous force}}$
Capillary Number	$\text{Ca} \equiv \frac{\eta U}{\sigma}$	$\frac{\text{Viscous force}}{\text{Surface tension forces}}$
Weber Number	$\text{We} \equiv \frac{\rho q U}{\sigma}$	$\frac{\text{Surface tension forces}}{\text{Inertial force}}$

We now evaluate the dimensionless numbers for each change in webspeed to investigate whether or not the governing equations remain dominated by the same mechanism (table 7.6).

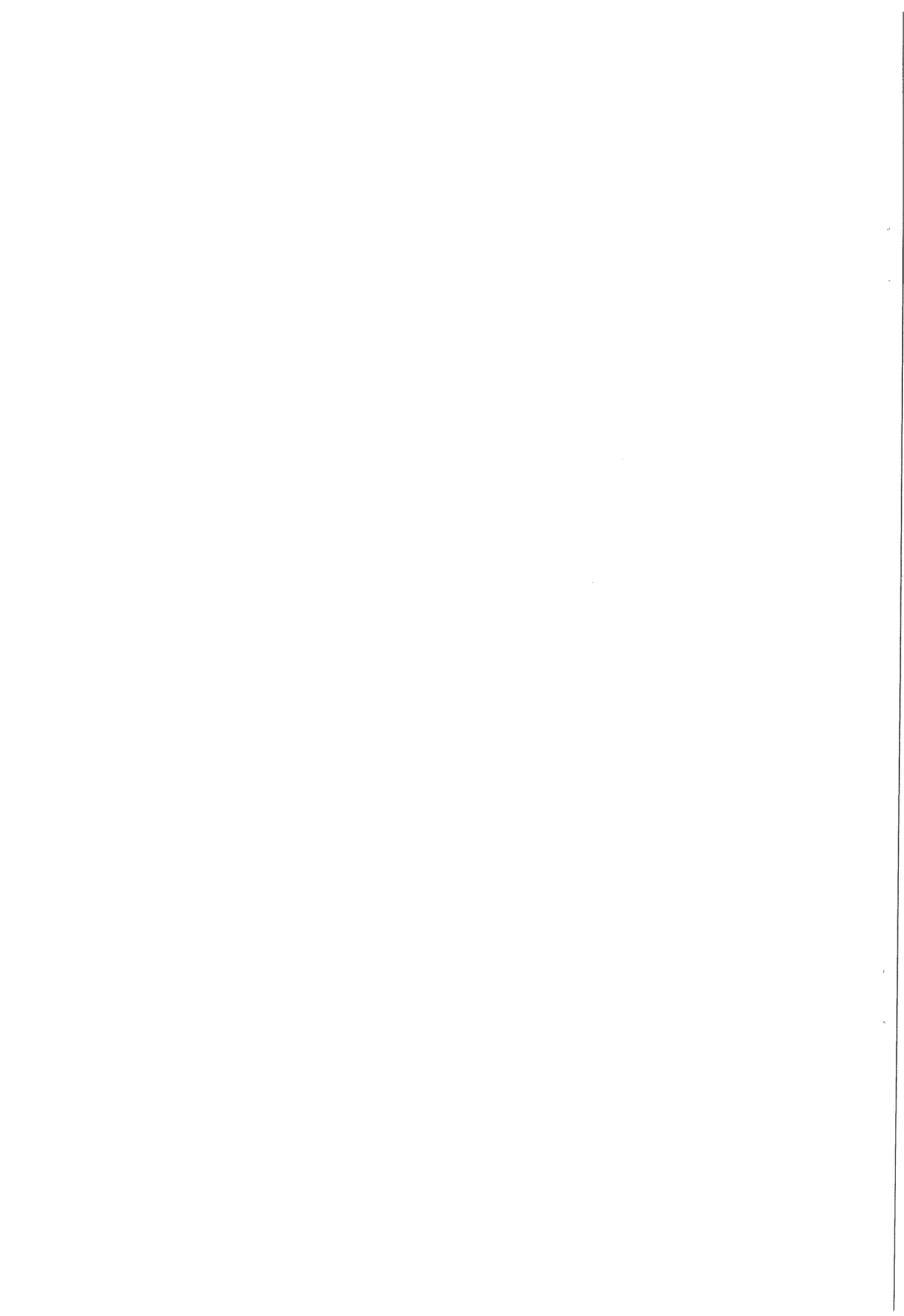


Table 7.6: Evaluation of dimensionless numbers relevant to the impingement flow, for varying web speeds.

U/V	Re	Ca	We	St $\cdot 10^{-5}$
-	-	-	-	-
1.4	5.43	1.13	6.15	7.39
1.5	5.82	1.21	7.06	6.90
1.8	6.99	1.46	10.17	5.75
1.9	7.38	1.54	11.33	5.45
2.1	8.15	1.70	13.84	4.93
2.3	8.93	1.86	16.61	4.50

Though all-important on the scale of curtain height, gravity is insignificant on the length scale of film thickness in the impingement zone. The Stokes number is of the order  $10^{-5}$ , hence gravity is not taken into account as a body force. The flow regime remains laminar over the entire range of web speeds. The Reynolds number exceeds unity, thus inertia is important and the choice of the solution algorithm should be made based on the Weber number instead of the capillary number. Therefore the kinematic solution algorithm was chosen on the free surfaces.

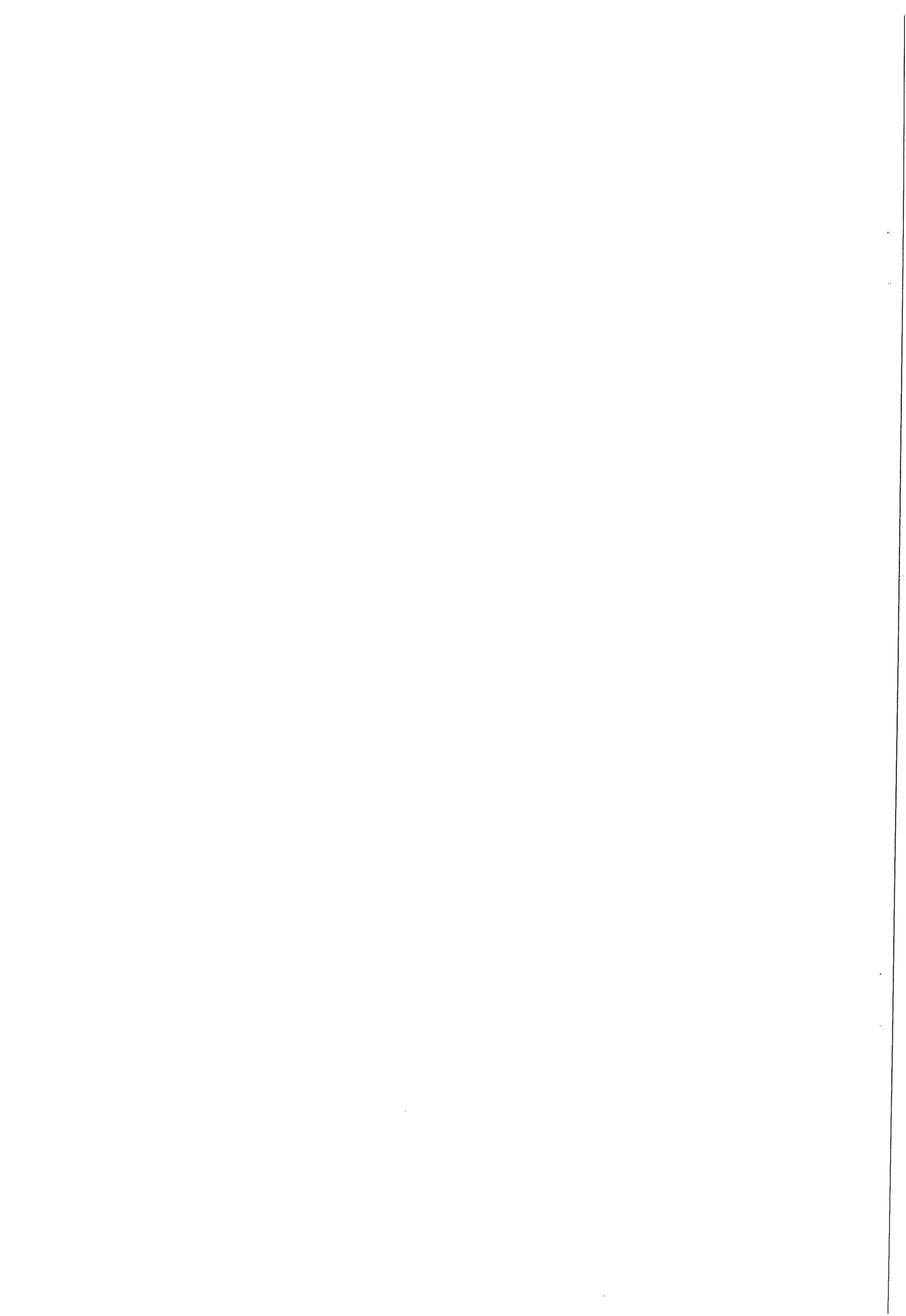
From the contours of x-velocity we may conclude that the slip region in the simulation at U/V of 1.4, with a free slip boundary condition, is too large (figure 7.6); the boundary layer starts to grow at the end of the slip region. In the simulations without slip the boundary layer starts in the dynamic contact point, as is to be expected (figure 7.7). For the other simulations no specific slip condition was applied near the dynamic contact point, because the weak form of the governing equations can handle the pressure and stress singularity. As shown in chapter 4, both methods of handling the pressure and stress singularity are ad hoc methods, with only a small physical significance. The only way to assess their accuracy is by comparing the calculated flow fields with experimental data.

Table 7.7 lists the results of the simulations: the actual wetting line position and the relative wetting line position for varying U/V; the latter are compared to predicted values, according to a theoretical model (eq. 5.21) by Blake et al. (1994).

Table 7.7: Results of the simulations for varying web speeds.

U/V	$\delta_{cu}$ $\mu\text{m}$	$L_\delta$ $\mu\text{m}$	$\Gamma'$	Blake pred. $\Gamma'$
-	-	-	-	-
1.4 (a)	22.4	19.2	0.857	0.800
1.4 (b)	22.4	15.6	0.696	0.800
1.5	24.0	17.4	0.725	0.922
1.8	28.8	24.5	0.851	1.174
1.9	30.4	27.1	0.891	1.233
2.1	33.6	31.3	0.932	1.326
2.3	36.8	36.0	0.978	1.396

When comparing the relative wetting line position to Blake's theoretical predictions, which take into account surface tension effects, the same trend is observed as in the simulations. There is, however, a large discrepancy between the simulations and the theoretical predictions. There are several possible reasons for this



difference: the fact that like in equation 5.19 the constants in equation 5.21 are dependent on the similarity velocity profile chosen (a maximum difference of 30% was found), and the fact that the solution may still be grid dependent as is shown in paragraph 7.6.

As web speed is increased the influence of surface tension in Blake's model fades and the relative wetting line position seems to reach an asymptotic value (figure 7.8). This agrees with Kistler's predictions where surface tension plays no role (eq. 5.19) and the relative wetting line position is independent of web speed:

$$l' = 0.383 \frac{M_{ct} V}{\eta}$$

7.3

According to this equation the relative wetting line position is 1.49 under the given conditions. This asymptotic behaviour can not be deduced clearly from the available simulation data.

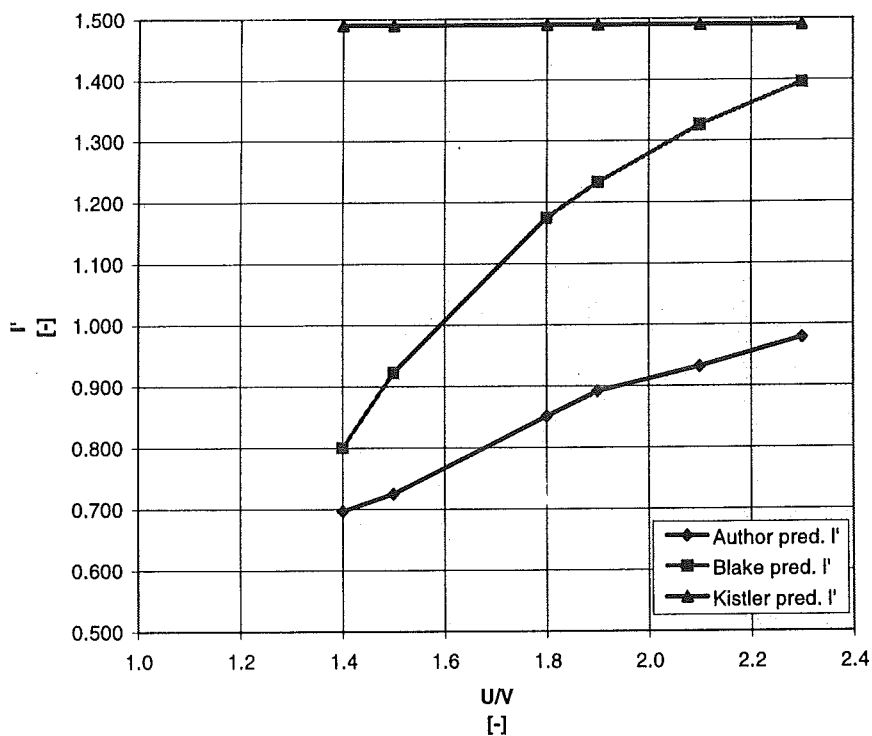
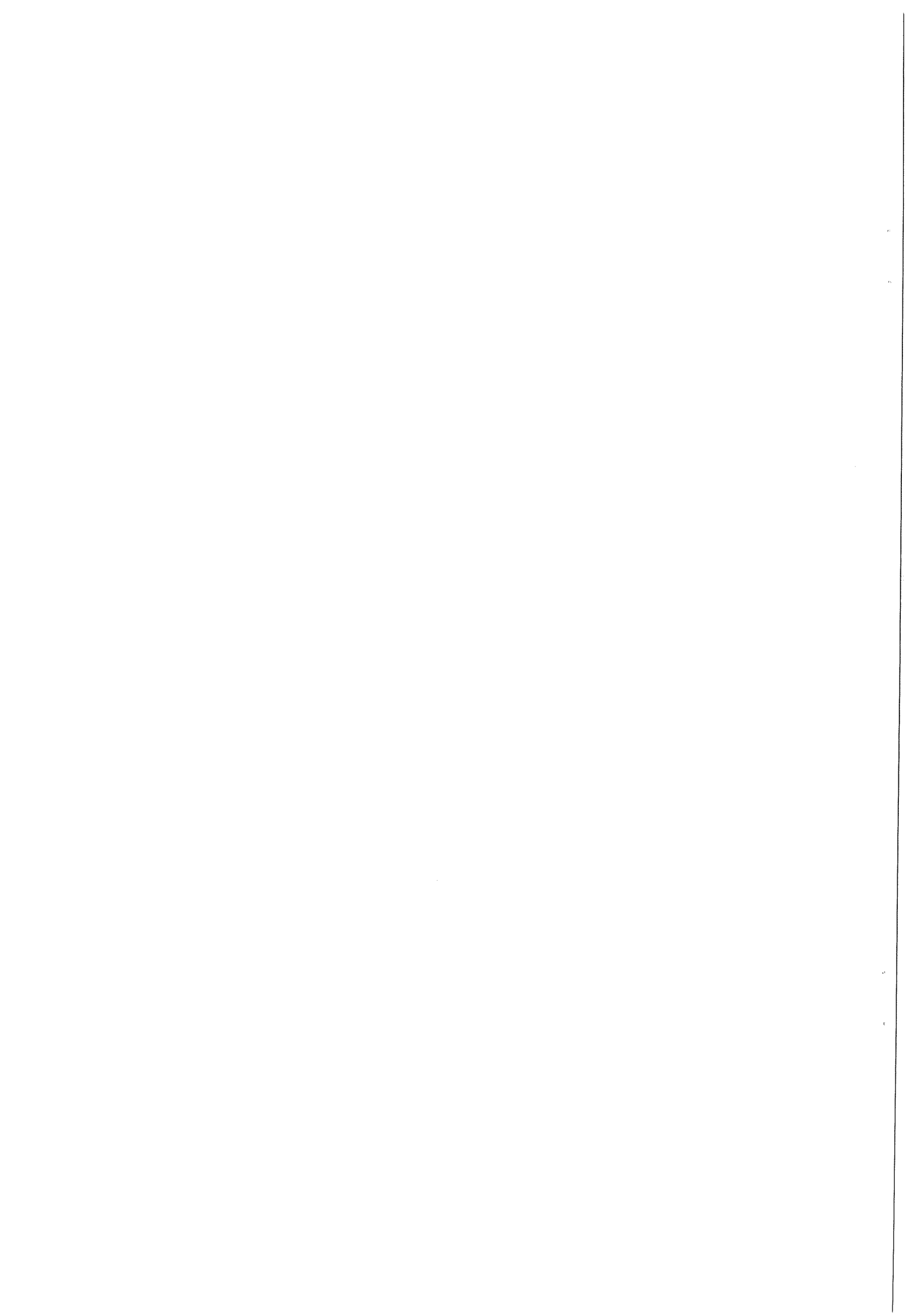


Figure 7.8: Prediction of the relative wetting line position v.s.  $U/V$  from simulations and a theoretical model by Blake et al. (1994)

The maximum and minimum pressure on the web in the heel region, vary very little with  $U/V$ , probably due to the small change in relative wetting line position.



### 7.3 Effect of Imposed Dynamic Contact Angle

At a speed ratio of 2.3, the dynamic contact angle was varied from 125° to 175° to investigate the influence on the rear free surface and the position of the dynamic contact point. To obtain the results as listed in table 7.8, the following translation was applied to the original data:

$$x_* = \frac{x_{dcp} - x_{ffs}}{\delta_{co}}$$

7.4

where  $x_{ffs}$  is the position of the front free surface.

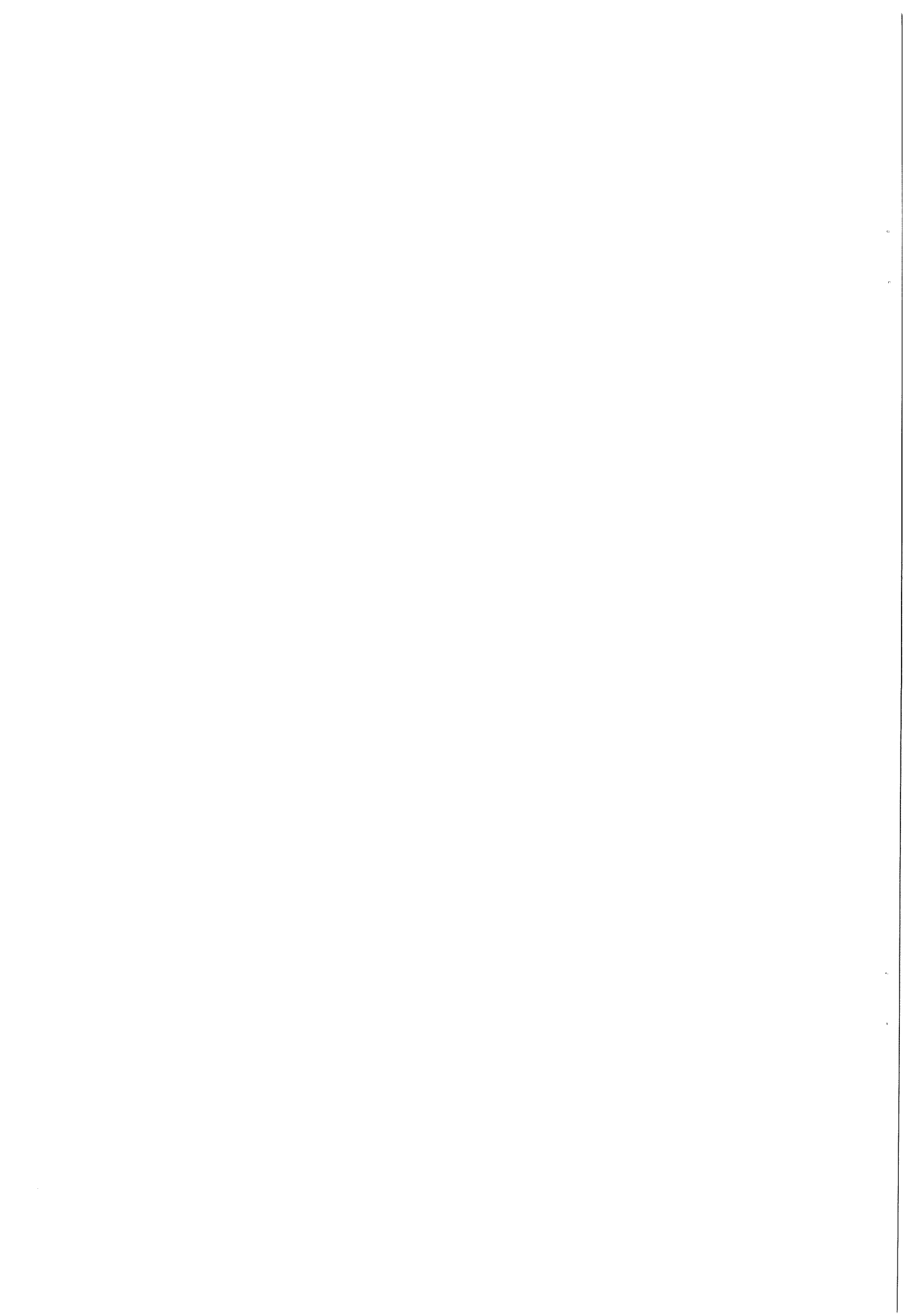
Table 7.8: Predicted dynamic contact point for a coarse and a fine mesh of order 4.  $Re = 8.93$ ,  $Ca = 1.86$ ,  $U/V = 2.3$ .

$\theta_D$	125°	145°	175°
$x_*$ coarse mesh	-2.28	-2.25	-2.23
$x_*$ fine mesh	-2.33	-2.32	-2.29

For both coarse and fine mesh solutions increasing  $\theta_D$  shifts the wetting line in the downstream direction. Figure 7.9 and figure 7.10 show how changing the imposed  $\theta_D$  deforms the free surface shape only locally; the overall free surface profile is almost unaffected. Especially at low  $\theta_D$  the free surface is curved very strongly so as to intersect the solid surface at the prescribed angle. Grid refinement captures these details more adequately. The results show, however, that the macroscopic flow field is not sensitive to the imposed dynamic contact angle.

### 7.4 Comparison of the Solvers

As mentioned before, in general large problems can no longer be solved efficiently using a direct solver because of the high RAM usage. We therefore need to explore iterative solvers. NEKTON uses a GMRES based solver, which should give the same results as the direct solver provided that the aspect ratio of the elements does not exceed  $l:b = 50:1$  (Grald, 1997). The solvers are compared using the case of an increase in  $U/V$  from 2.1 to 2.3. Again a translation according to equation 7.4 is applied to the original data. Figure 7.11 and figure 7.12 show the entire profile of the rear free surface and a magnification found with the direct and iterative solver. The iterative solution shifts the dynamic contact point slightly in the upstream direction,  $\Delta x_* = x_{*it} - x_{*dir} = -2.251 + 2.249 = -0.002$ . The small value for  $\Delta x_*$  shows that both solvers are consistent. We consider a shift in dynamic contact point one order of magnitude greater than this value to be a significant change.



## 7.5 Increasing the Polynomial Order

For a given grid the interpolation of the solution on that grid can be improved by increasing the polynomial order of the basis functions used for discretisation. The basic coarse mesh with order four was used as a starting-point for the simulations. The order was varied uniformly with increments of two to a final value of eight.

Comparison of the transformed data, using equation 7.4, shows that for the order  $n = 6$ , the dynamic contact point lies at  $\Delta x_* = x_{*n=6} - x_{*n=4} = -2.245 + 2.249 = 0.004$  and for  $n = 8$ , at  $\Delta x_* = -2.241 + 2.249 = 0.008$ . In other words the dynamic contact point shifts downstream with an increase in polynomial order. The amount of movement, however, is almost negligible and as can be seen from figure 7.13 and figure 7.14 the rear free surface and thus the entire flow field is not affected by this change.

## 7.6 Grid Refinement

Next to the fact that the solution should be independent of the polynomial order of the basis functions, it should also become independent of the grid. The basic coarse mesh of order four was therefore remeshed in the heel region, because this is the area where the biggest changes occur. In the fine mesh solution the dynamic contact point moved upstream with respect to the coarse mesh solution,  $\Delta x_* = x_{*fine} - x_{*coarse} = -2.316 + 2.249 = -0.067$ . Furthermore, the change in free surface shape due to grid refinement is much more radical than that due to the change in order, both on macroscopic as on submacroscopic scale (figure 7.15 and figure 7.16).

Grid refinement up to molecular dimensions yields mathematically acceptable solutions (Lowndes, 1980). When mechanisms at these length scales need to be resolved, however, the governing equations and boundary conditions need to be adapted to account for the physics that apply at these dimensions.

## 7.7 Pressure Distribution

Aside from curvature and x-velocity we are especially interested in the pressure distribution on the web. A large pressure will result in a more rapid penetration of the fluid into the paper. Therefore the more porous a paper gets, the smaller the maximum pressure should be to avoid that the coating is pushed through the paper.

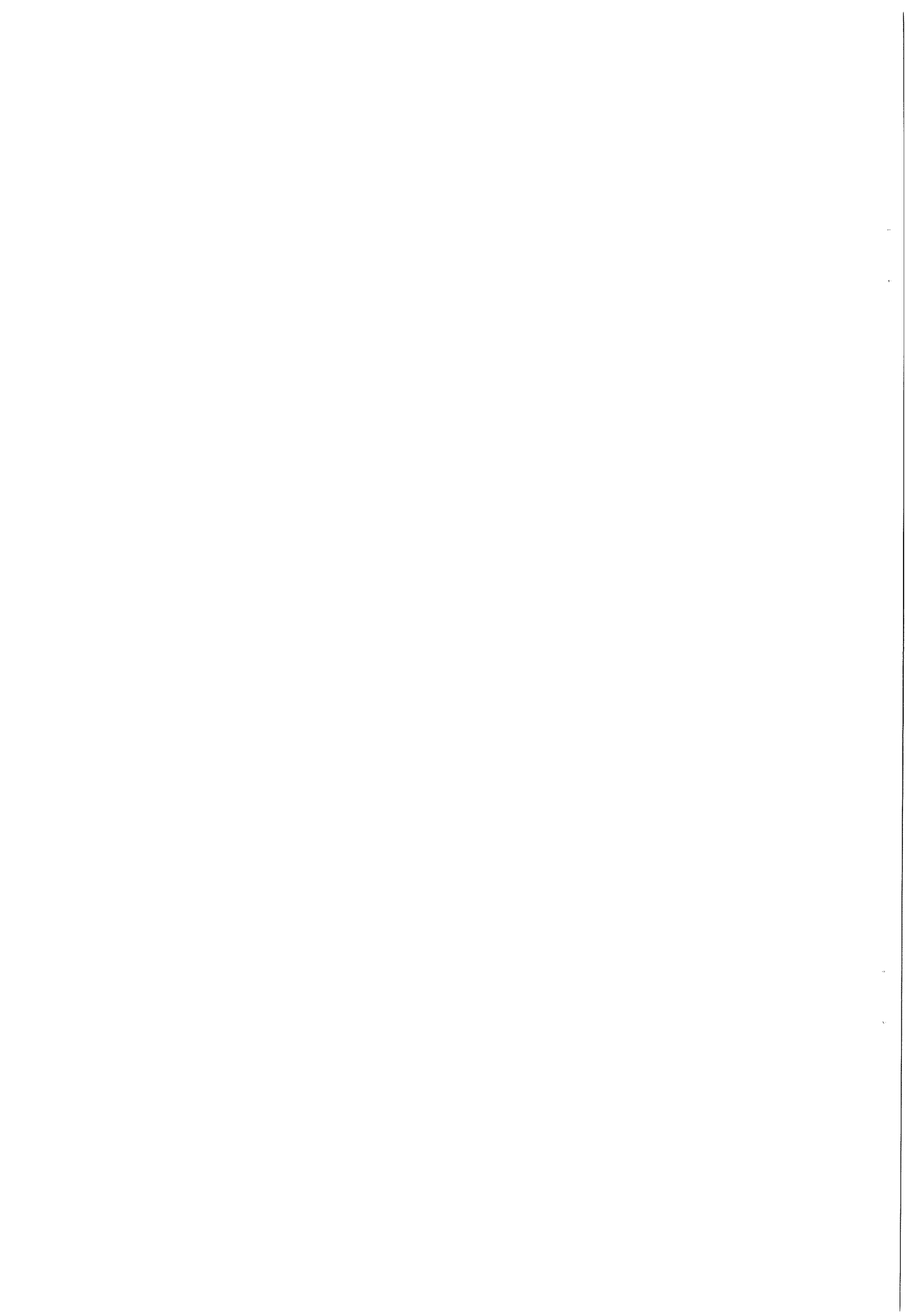
For both coarse and fine mesh bell shaped pressure contours are predicted straight under the curtain (figure 7.17 and figure 7.18). In both simulations there is a small region of negative pressure just left of the pressure singularity. This region, like the stress singularity diminishes when the grid is refined.

We will now look more closely to the pressure profile on the web in the heel region. To obtain the graphs a translation based on equation 7.4 was applied. The pressure was made dimensionless with:

$$p = \frac{1}{2} \rho V^2 = \rho g h$$

7.5

where  $h$  is the curtain height.



---

Figure 7.19 shows how both increase in polynomial order as well as grid refinement seem to have almost no influence on the predicted pressure profile on the web. The pressure singularity is just isolated upon order increase or grid refinement. The magnification (figure 7.20), however shows that an increase in order does not smoothen the pressure profile, whereas grid refinement does.

Figure 7.21 shows that the front free surface does not move. On the front free surface there is a small region of negative pressure due to capillarity.



## 7.8 Figures

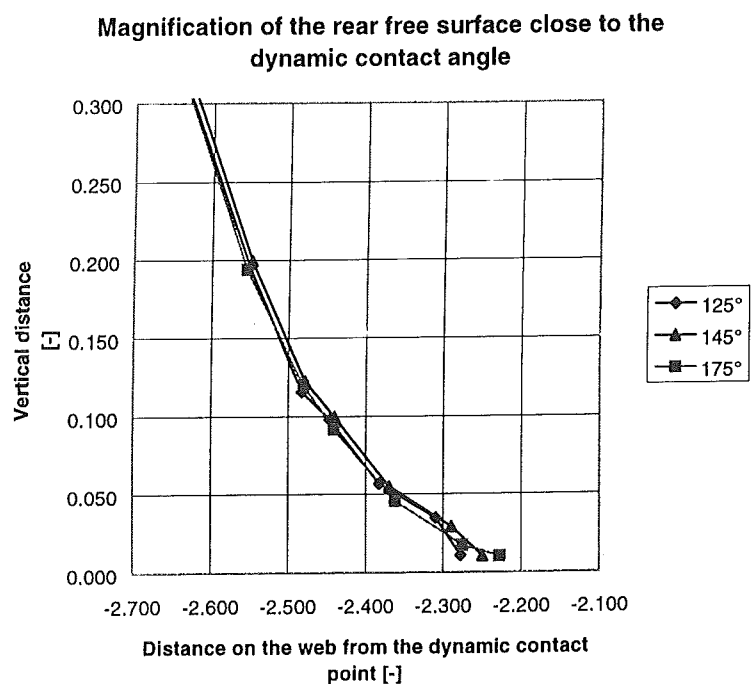


Figure 7.9: The influence of the imposed  $\theta_D$  on the shape and position of the rear free surface close to the wetting line (coarse mesh  $n = 4$ ,  $Re = 8.93$ ,  $Ca = 1.86$ ,  $U/V = 2.3$ ).

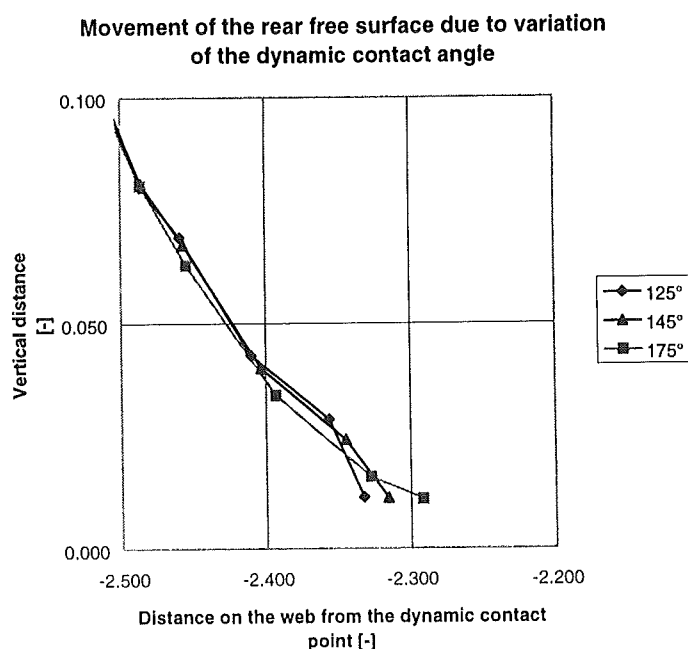
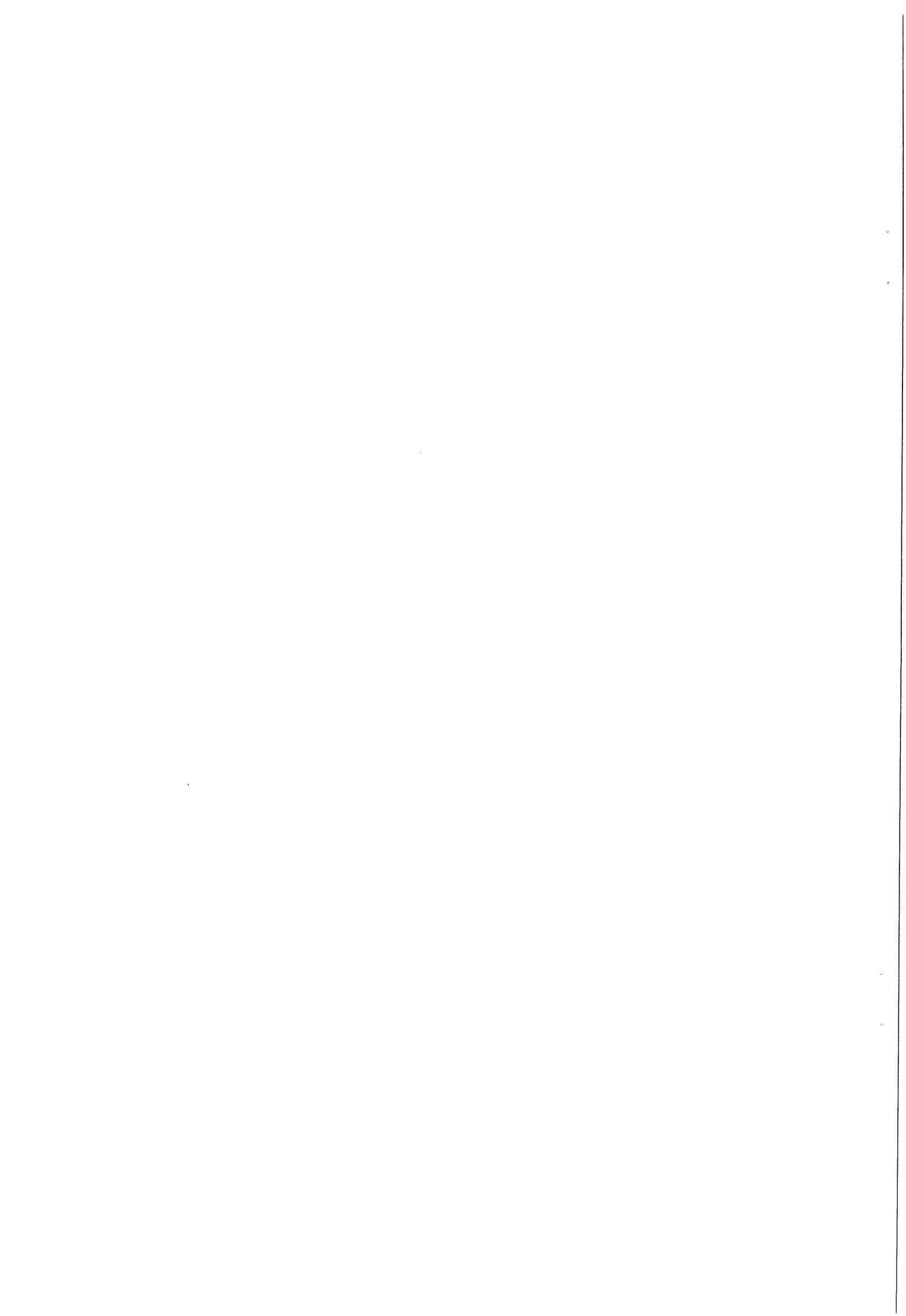


Figure 7.10: The influence of the imposed  $\theta_D$  on the shape and position of the rear free surface close to the wetting line (fine mesh  $n = 4$ ,  $Re = 8.93$ ,  $Ca = 1.86$ ,  $U/V = 2.3$ ).



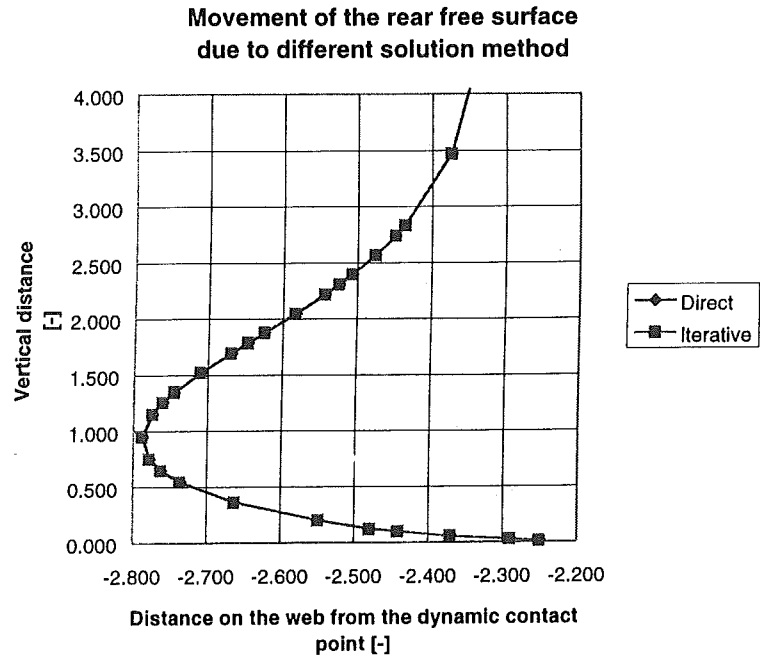


Figure 7.11: The influence of the type of solver on the consistency of the solution on macroscopic scale (coarse mesh  $n = 4$ ,  $Re = 8.93$ ,  $Ca = 1.86$ ,  $U/V = 2.3$ )

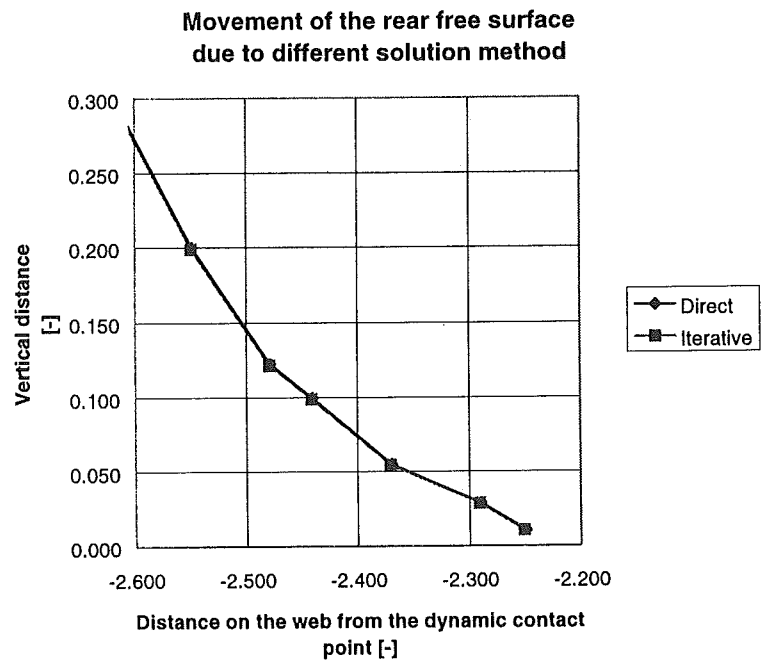


Figure 7.12: The influence of the type of solver on the consistency of the solution close to the wetting line (coarse mesh  $n = 4$ ,  $Re = 8.93$ ,  $Ca = 1.86$ ,  $U/V = 2.3$ ).



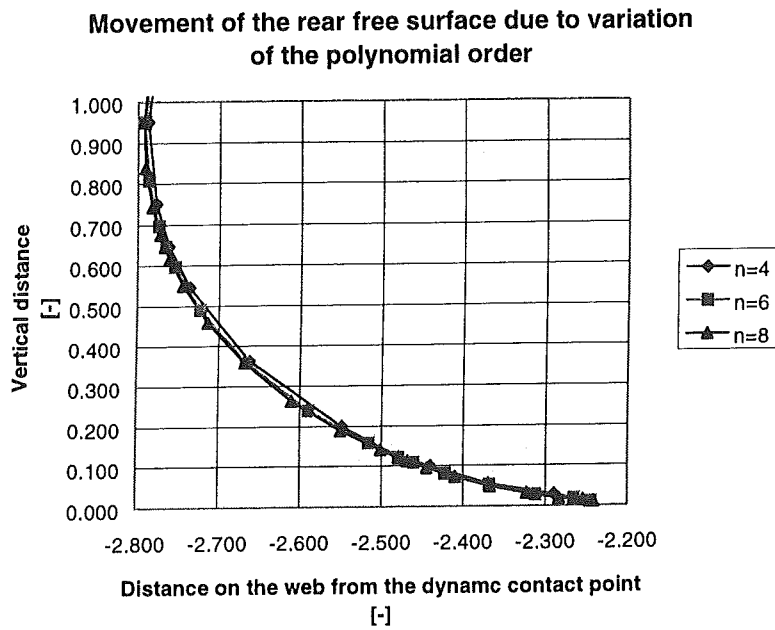


Figure 7.13: The influence of the polynomial order on the solution, macroscopic scale (coarse mesh,  $Re = 8.93$ ,  $Ca = 1.86$ ,  $U/V = 2.3$ ).

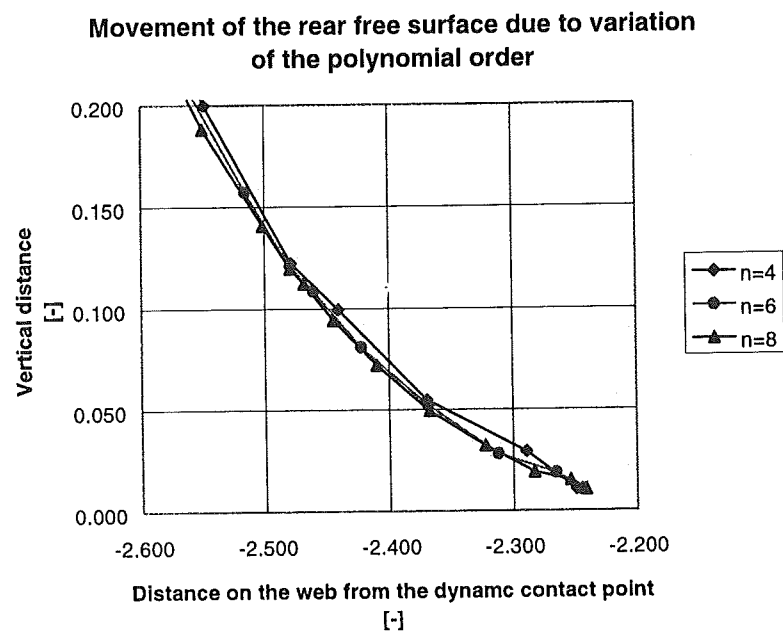
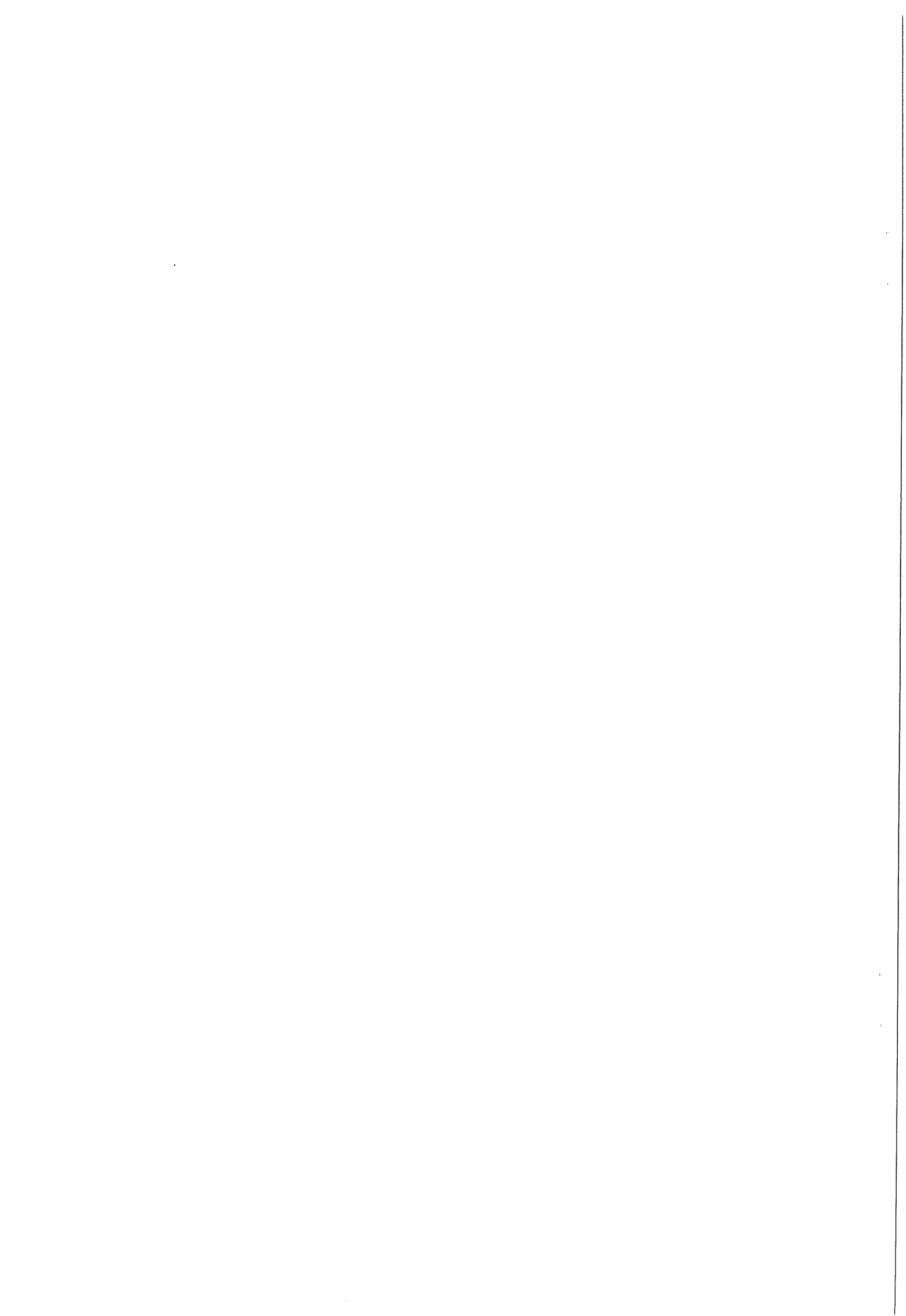


Figure 7.14: The influence of the polynomial order on the solution, close to the wetting line (coarse mesh,  $Re = 8.93$ ,  $Ca = 1.86$ ,  $U/V = 2.3$ ).



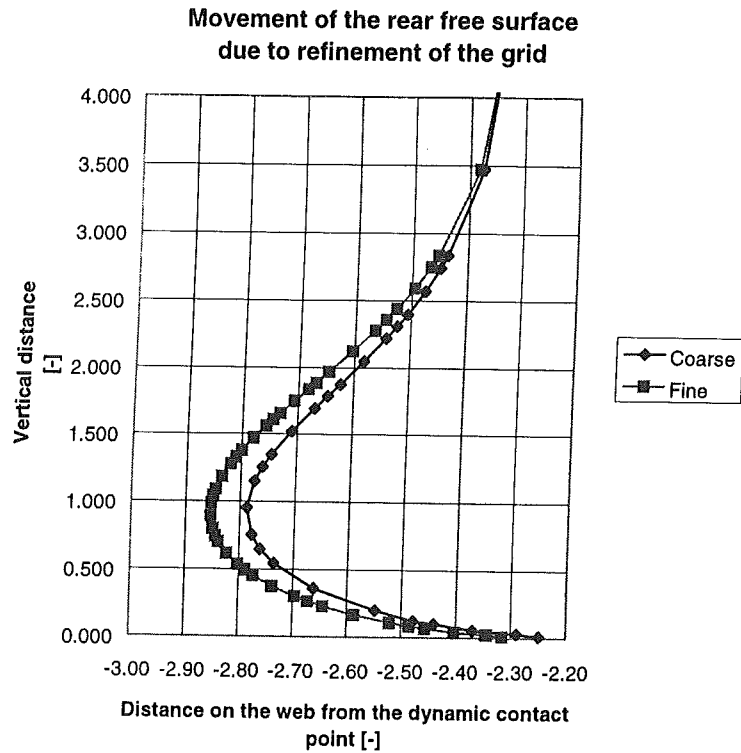


Figure 7.15: The influence of grid refinement on the position and shape of the rear free surface, macroscopic scale ( $n = 4$ ,  $Re = 8.93$ ,  $Ca = 1.86$ ,  $U/V = 2.3$ ).

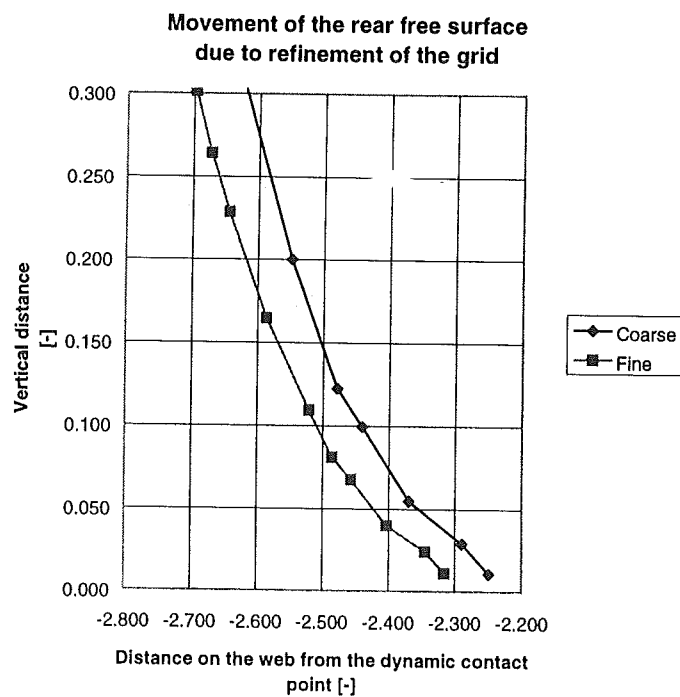


Figure 7.16: The influence of grid refinement on the position and shape of the rear free surface close to the wetting line ( $n = 4$ ,  $Re = 8.93$ ,  $Ca = 1.86$ ,  $U/V = 2.3$ ).





Figure 7.17: Contours of pressure in the heel region (coarse mesh,  $n = 4$ ).

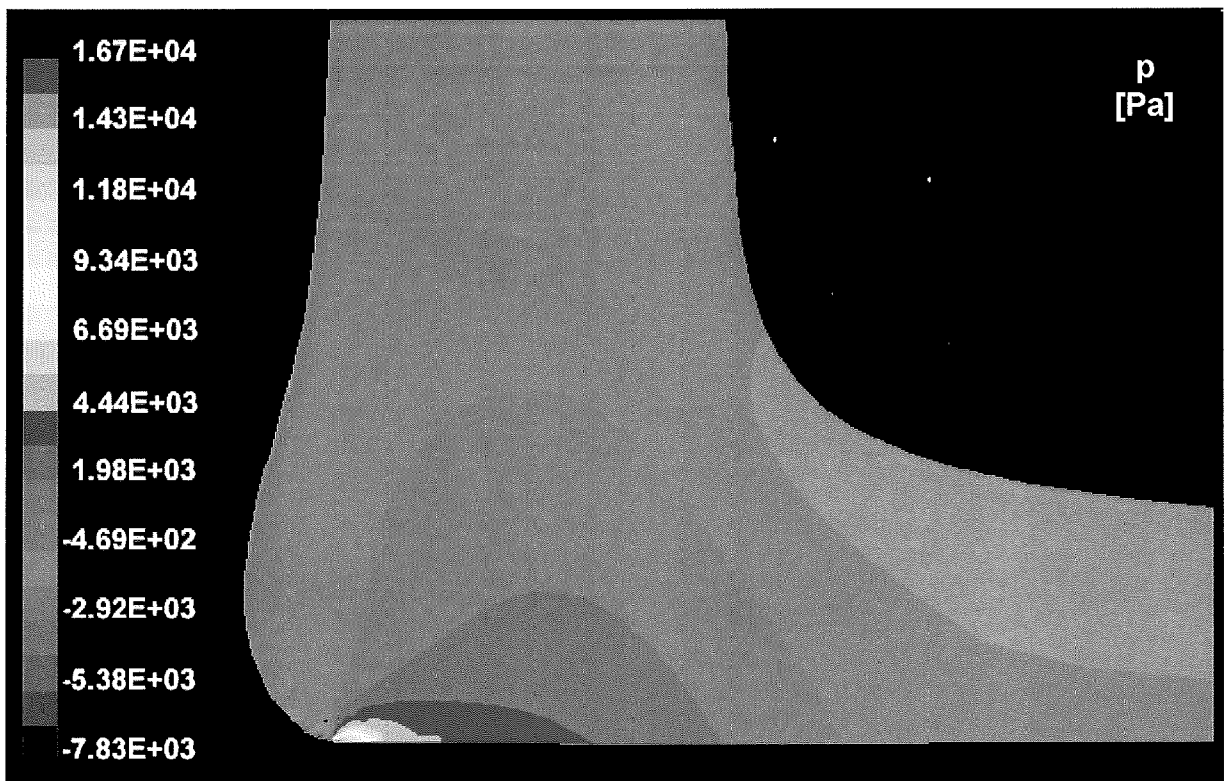


Figure 7.18 Contours of pressure in the heel region (fine mesh,  $n = 4$ ).



Pressure profile on the web

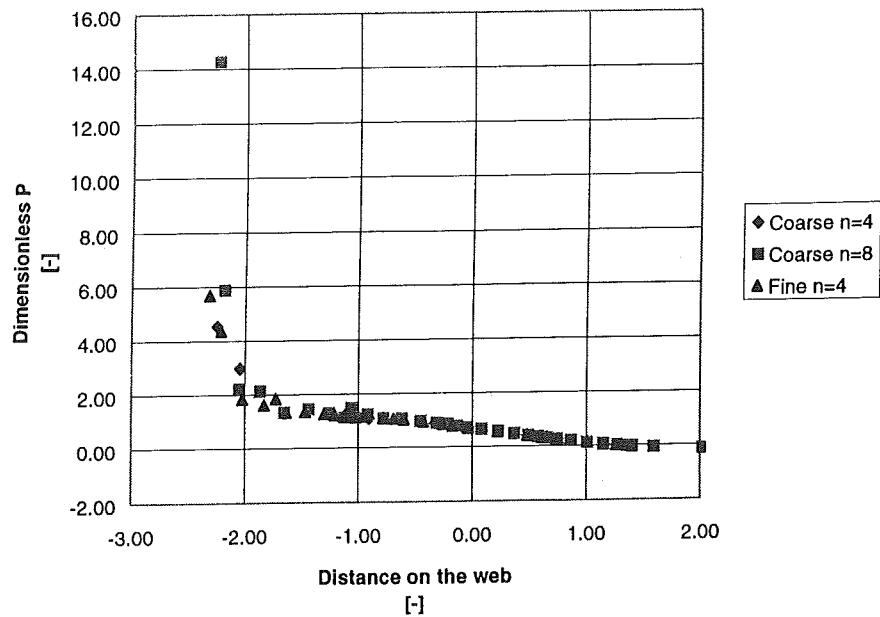


Figure 7.19: The pressure profile on the web for a coarse mesh of order four and eight and a fine mesh of order four ( $Re = 8.93$ ,  $Ca = 1.86$ ,  $U/V = 2.3$ ).

Pressure profile in the heel region  
(the dynamic contact point excluded)

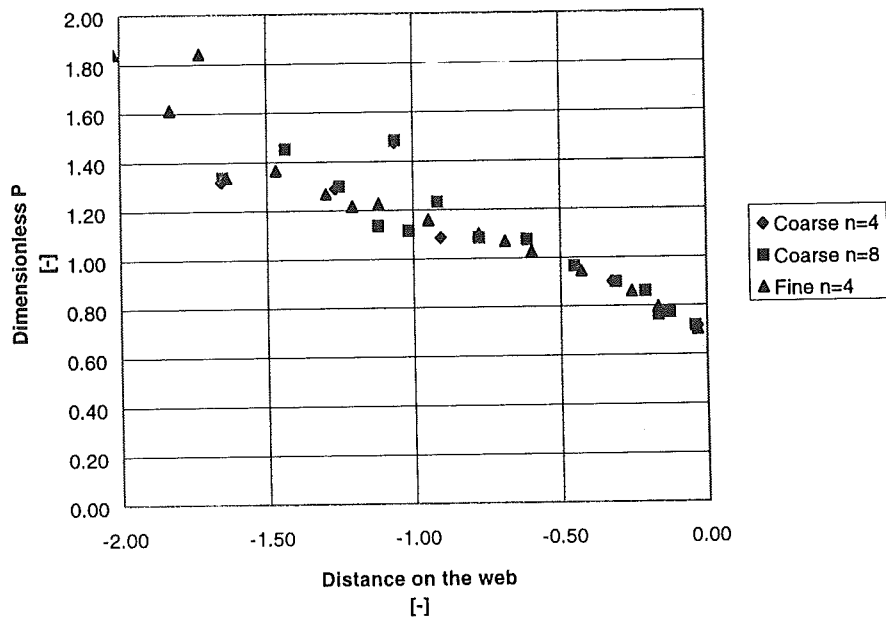


Figure 7.20: The pressure profile on the web for a coarse mesh of order four and eight and a fine mesh of order four (the dynamic contact point excluded). ( $Re = 8.93$ ,  $Ca = 1.86$ ,  $U/V = 2.3$ ).



Pressure at the front free surface

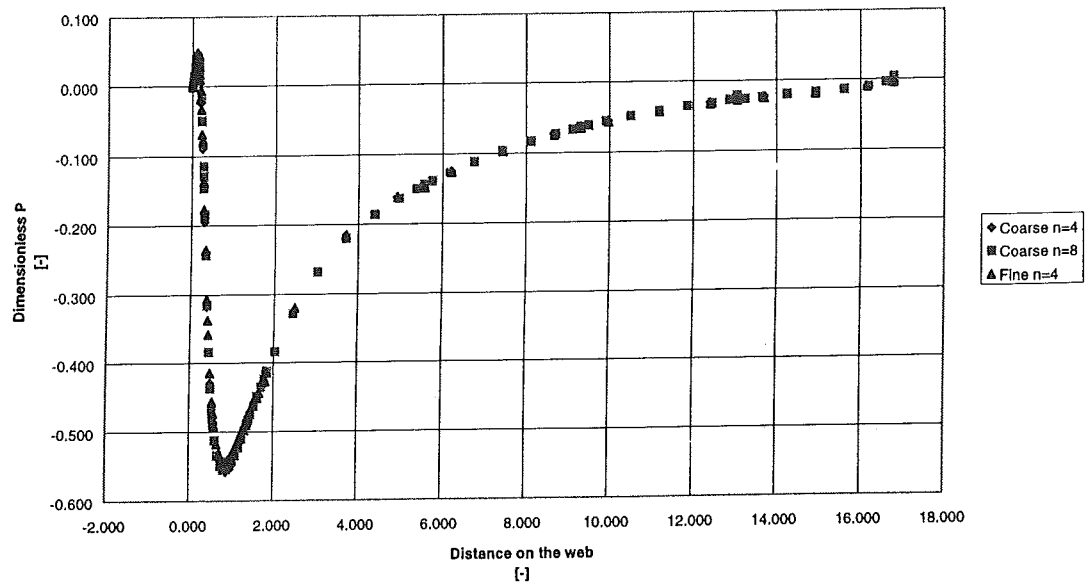
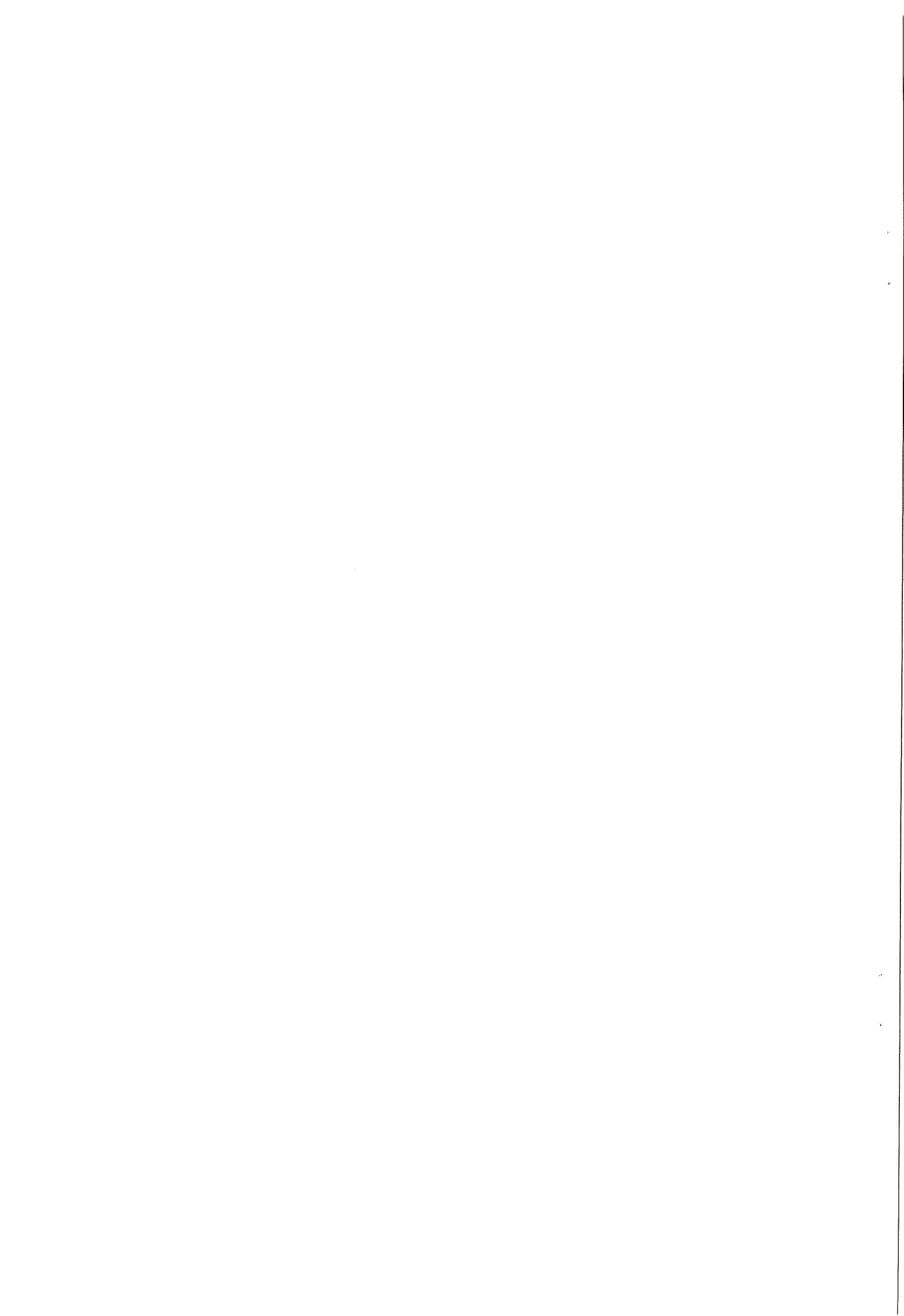


Figure 7.21: The pressure profile on the front free surface for a coarse mesh of order four and eight and a fine mesh of order four ( $Re = 8.93$ ,  $Ca = 1.86$ ,  $U/V = 2.3$ ).



## 8. Experimental Study of Curtain Coating

The simulations are complemented by experimental work covering four different areas. First, characterisation of the coating fluid; the obtained data is used as an input in the simulations. Second, both static as well as dynamic off-line experiments were done to get a feel for the process and to study the achievable coating window. Third, results obtained from the off-line set-up were verified with pilot coater experiments, to judge their consistency. Finally the design of the edge guides, needed to maintain the curtain at full width, and related edge effects were studied more closely.

### 8.1 Fluid Characterisation

#### *Viscosity*

One of the most important steps in applying a new coating technique is to characterize liquid to be coated in terms of viscosity behaviour, surface tension and density. As is shown below fluid properties may have a significant influence on stability of the curtain coating process, at the same time they are an input in the simulations as well. In the experiments done for this thesis one coating fluid was used. Its viscosity behaviour was measured using a Brookfield viscosimeter for the low shear rate range and a Haake viscosimeter for the high shear range. Figure 8.1 shows a log-log plot of the shear stress versus the shear rate, the regression line and its 95% confidence interval.

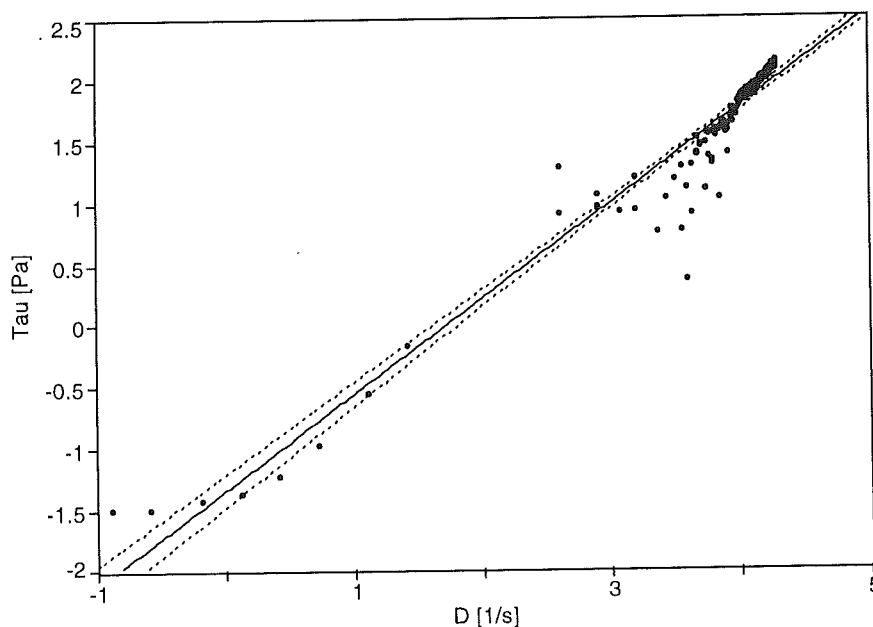


Figure 8.1: A log-log plot of shear stress versus shear rate.

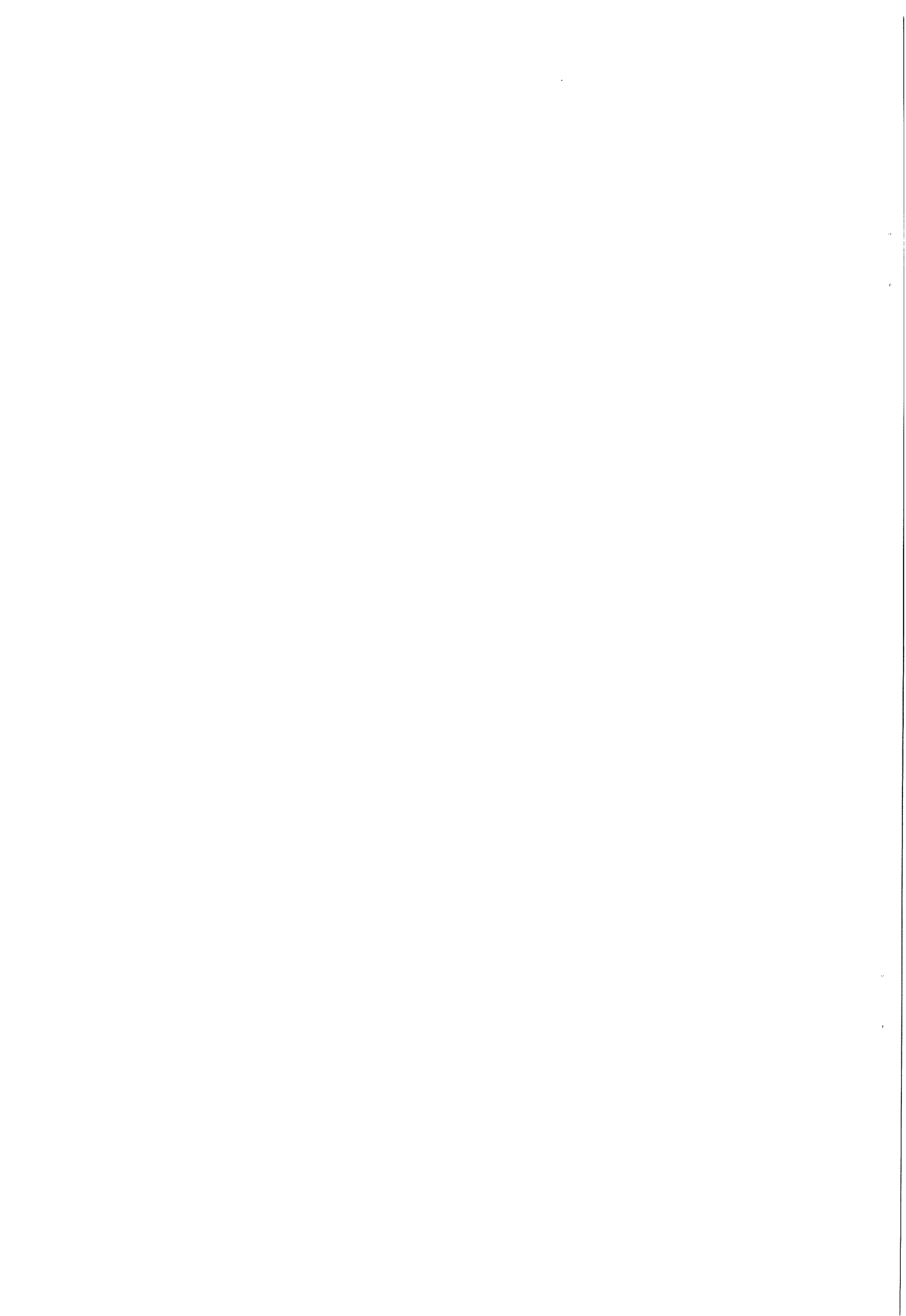


Table 8.1 lists the regression statistics of the fitted line in figure 8.1.

Table 8.1: Regression statistics.

R squared	0.9353
Adjusted R square	0.9344
Fit Standard Error	0.1933
F statistic	1995

The resulting regression line is:

$$\log(\tau) = 0.7772 \log(D) - 1.3570$$

8.6

### Surface Tension

The static surface tension was measured using the Du Noüy ring method (Hunter, 1987). The surface tension force acts around the perimeter of the ring which is being withdrawn from the liquid surface. This force is measured directly using a microbalance to determine the apparent weight of the ring as it is being withdrawn from the liquid surface. Since the meniscus forms on both sides of the ring, the force is given as:

$$F = 4 \pi r \sigma = m g$$

8.1

where  $m$  is the apparent mass. The static surface tension was found to be  $32 \text{ mN}\cdot\text{m}^{-1}$ .

In most coating processes free surfaces are created, surfactants present in the coating liquid need time to diffuse to this surface, hence the surface tension will no longer equal its static value. The dynamic surface tension, at a distance from the die lip is obtained by poking the falling liquid curtain with a needle and measuring the Mach angle,  $\theta'$  (figure 8.2).

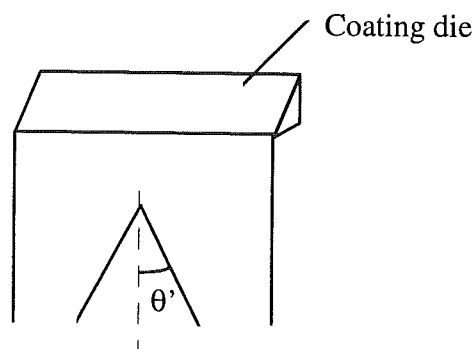


Figure 8.2: Measurement of the Mach angle.



The dynamic surface tension is then calculated according to (Brown, 1961):

$$\sigma_{\text{dyn}} = \frac{\rho \delta_{\text{cu}}}{2} V^2 \sin^2(\theta')$$

8.2

At a distance of 15 cm from the die lip and a flow rate per meter die width of  $1.61 \cdot 10^{-4} \text{ m}^3 \cdot \text{m}^{-1} \cdot \text{s}^{-1}$ , the Mach angle was  $26.5^\circ$  and thus the dynamic surface tension was  $27 \text{ mN} \cdot \text{m}^{-1}$ . Because of this relatively small change with respect to its static value, surface tension was assumed constant in the simulations.

### Density

Density, as mentioned in the table 7.1 with simulation conditions was approximately that of water.

## 8.2 Off-line Experiments

The main advantages of an off-line set-up are its cost effectiveness: unlike pilot equipment, no substrate is wasted nor are large amounts of coating liquid required for testing since the liquid can be recycled; and its availability: because of the high work load on the pilot equipment it can not be used frequently for the experiments. For the off-line experiments two separate units were used: a so-called static off-line set-up (figure 8.3) and a dynamic off-line set-up (figure 8.6).

### 8.2.1 Static Off-line Set-up

The static off-line experiments were done with the set-up shown in figure 8.3: liquid is pumped from a supply tank through a set of filters to avoid fouling of the equipment and at the same time reduce the size of the air bubbles present in the feed. The liquid is then pumped into the 50 cm wide die and a film is formed on the slide, which detaches at the slide lip to form a curtain. The curtain then impinges on a pivoted plate, which is used to adjust curtain height. To reduce testing cost the coating liquid is collected and recycled.

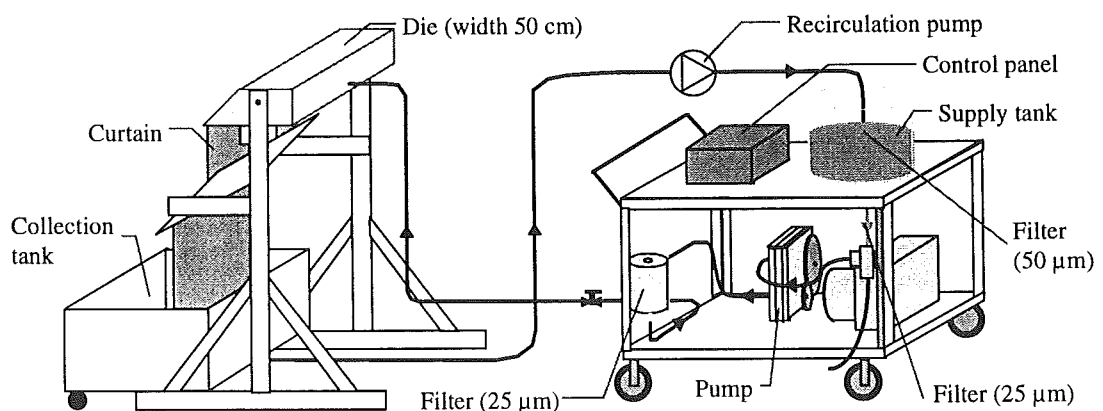


Figure 8.3: Static off-line set-up.



The static set-up is used to investigate several aspects of curtain coating. First of all the so-called teapot effect is studied. As mentioned in chapter 5.4, whether or not the static contact line remains pinned at the die lip or migrates under the die is important because it can critically affect product uniformity; next to that the trajectory of the falling liquid curtain can become such that it will no longer attach to the edge guides. In the experiments the influence of flow rate and slide angle on the occurrence of the teapot effect was studied. Already at intermediate flow rates the liquid bent back under the die lip (figure 8.4 a), leaning the die forward by 15° reduced the minimum flow rate, required to prevent curtain bend back. This was, however, not a sufficient solution to the problem and therefore an add-on piece was made (figure 8.4 b). Due to its sharp edge the liquid no longer creeps under the die. For further testing the die was put back into its horizontal position.

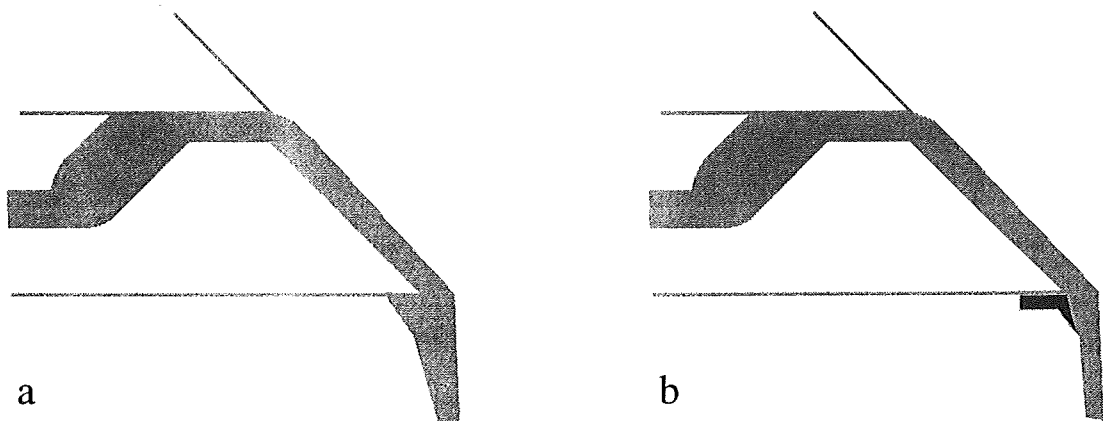


Figure 8.4: Flow of the liquid film near the die-lip, without and with add-on slide to prevent the tea-pot effect.

The next step is to determine the minimal flow rate per meter die width required to maintain a stable curtain. The curtain is considered to be stable when it reestablishes itself after intentional breakup, due to penetration of the curtain with a rod. The minimal flow rate is mainly a function of curtain height and liquid properties, i.e. density, viscosity and surface tension. In the experiments the curtain height was fixed at about 27 to 30 cm; when all other liquid properties are kept constant as well, a minimal flow rate of  $6.43 \cdot 10^{-5} \text{ m}^3 \cdot \text{m}^{-1} \cdot \text{s}^{-1}$  is found.

As a next step viscosity was increased using hydroxy-ethyl cellulose (HEC), which is chemically inert. Figure 8.5 shows a plot of the viscosity dependence on the concentration of HEC in water at 25 °C. Unfortunately HEC did not mix to well with the coating liquid used for the experiments. The amount of stirring required, resulted in massive foaming which persisted for quite some time, due to the large increase in viscosity, even at low concentrations of HEC. Since an air free feed is required to form a stable curtain, this method could not be used.



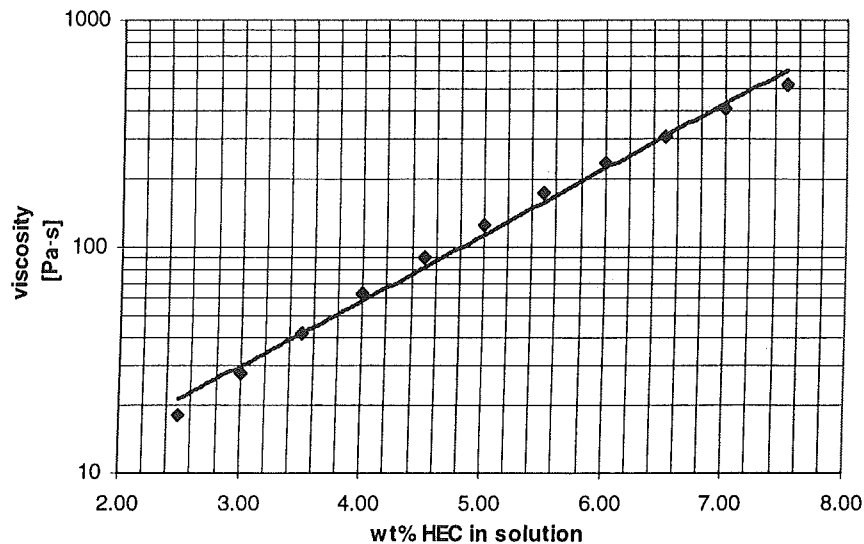


Figure 8.5: The viscosity as a function of the dissolved amount of HEC in water of 25 °C.

The resulting regression line is:

$$\eta = 4.0168 e^{0.6682c} \quad [\text{Pa} \cdot \text{s}]$$

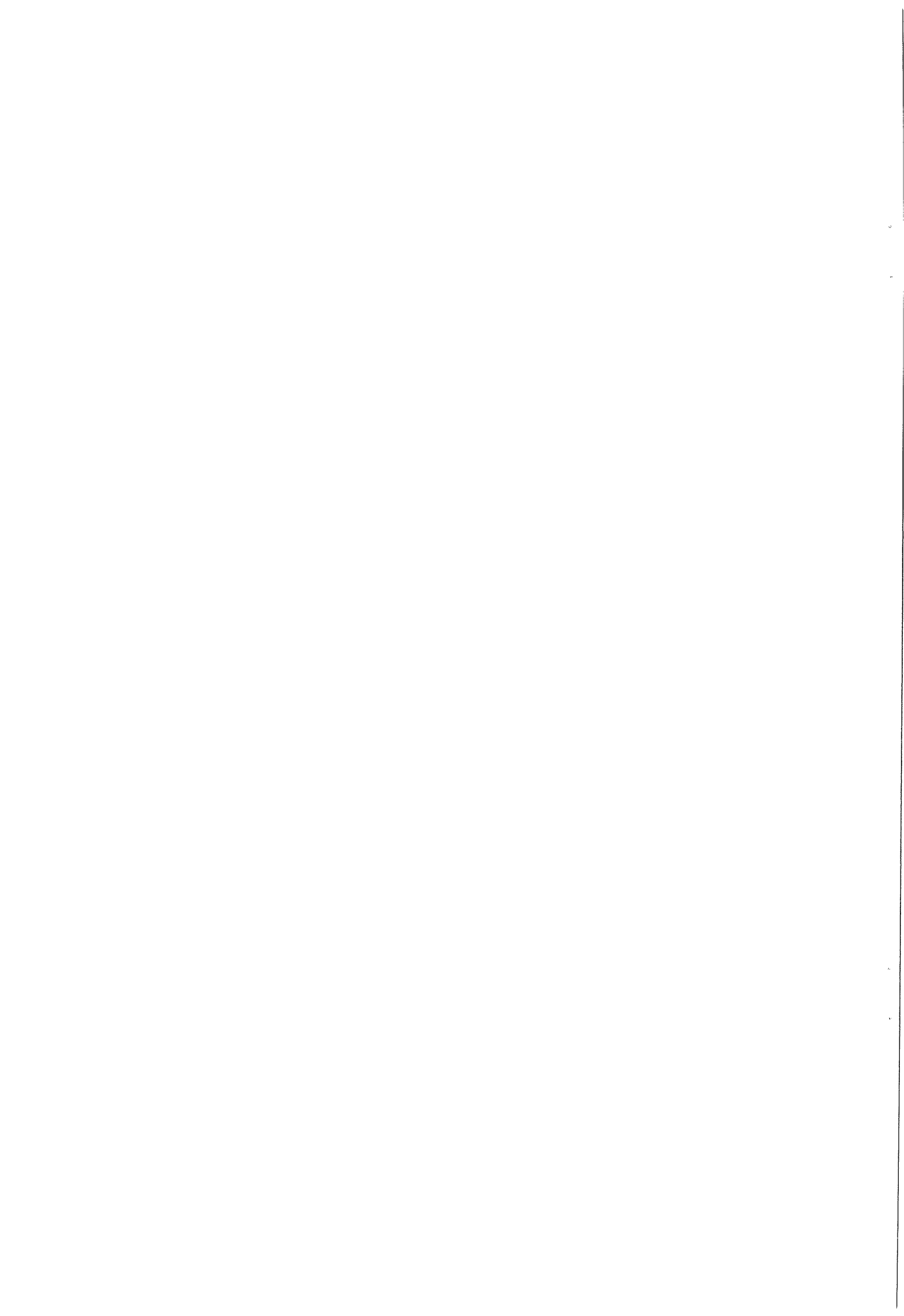
8.3

where  $c$  is the concentration of HEC in weight percent. The regression line explains 99% of the variance in the data.

### 8.2.2 Dynamic Off-line Set-up

Since curtain coating is a dynamic process, these aspects should be investigated as well. Therefore a dynamic off-line set-up was build, having the same advantages with respect to on-line equipment as the static set-up. In the dynamic set-up (figure 8.6) the curtain falls onto a rotating roll, which can be varied in speed up to 750 m/min. At the bottom the liquid is scraped off using a Teflon squeegee. However, a small residual liquid film will persist on the roll, which may affect the wetting properties and thus heel formation. Dynamic wetting studies, on the other hand, suggest that dynamic wetting depends mainly on the liquid flow rate,  $q$ , and the velocity ratio,  $U/V$ , and is largely independent of the substrate properties.

The air that is being dragged in by the rotating roll causes the curtain to flutter. When a barrier, a so-called airwipe, is put behind the curtain this flutter is eliminated. Experiments show that the airwipe should be placed onto the roll for maximum efficiency.



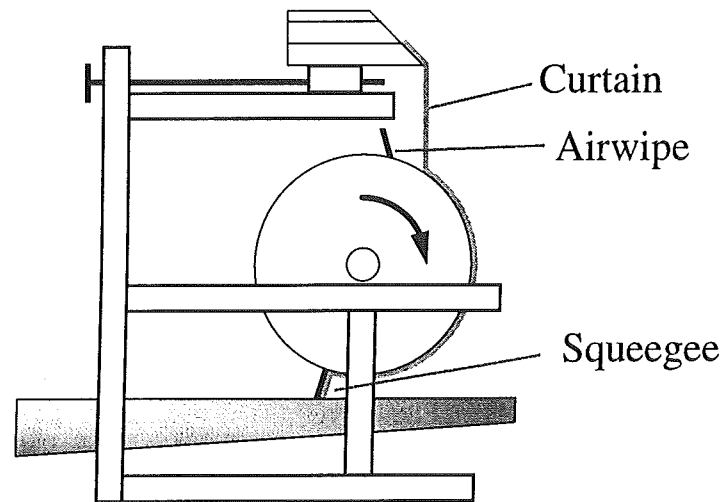


Figure 8.6: The dynamic off-line set-up.

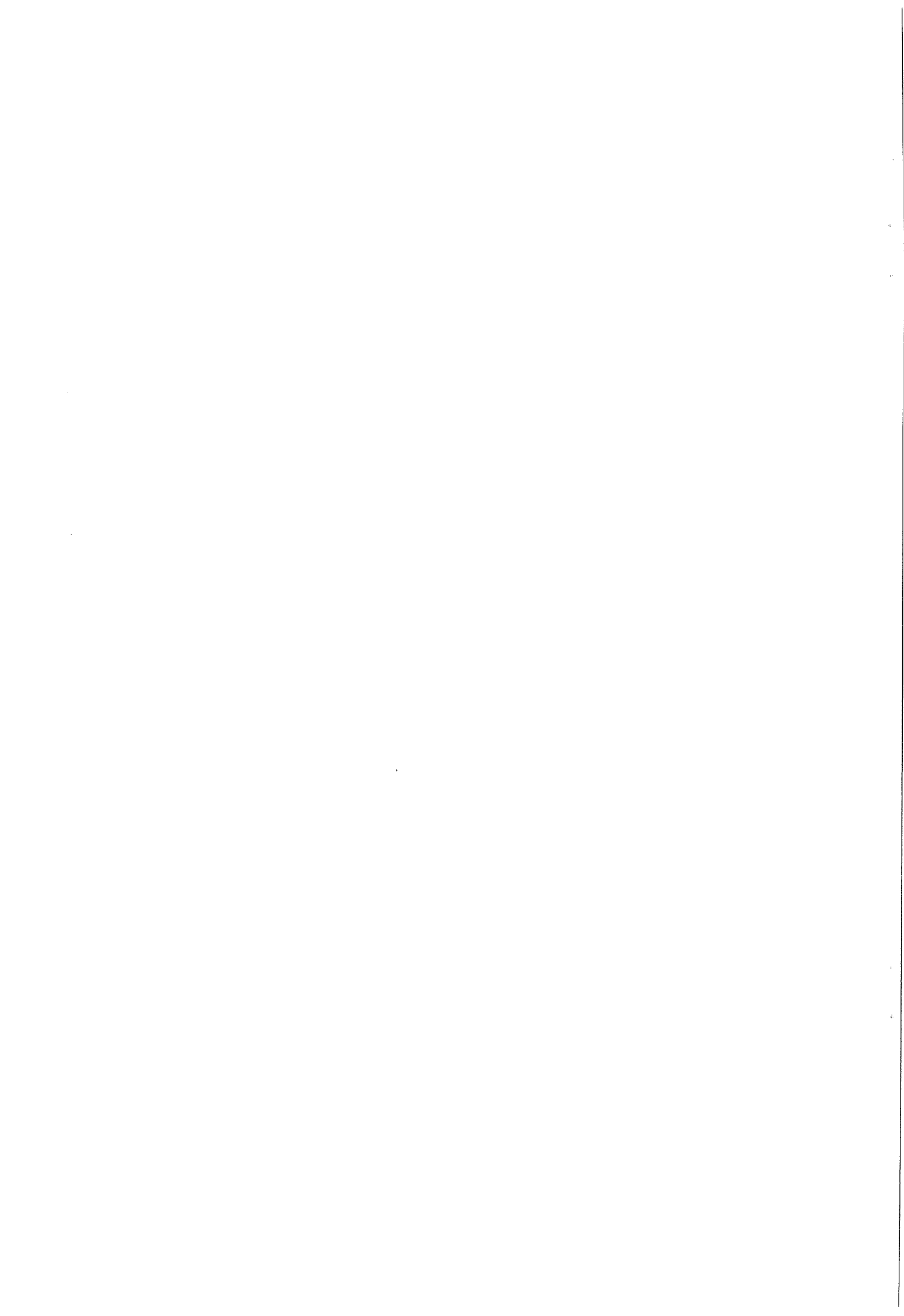
The first objective is to find the coating window, within which a stable heel is formed. Two types of experiments were carried out, both with fixed curtain height (29 cm). In the first series the coating thickness was fixed at  $16 \text{ g/m}^2$ ; both the premetered flow rate and the web speed were varied according to table 8.2.

Table 8.2: Experimental conditions used for the first series of dynamic off-line experiments.

U $\text{m}\cdot\text{min}^{-1}$	Flow rate $\cdot 10^{-5} \text{ m}^3\cdot\text{m}^{-1}\cdot\text{s}^{-1}$	U/V -
200	5.33	1.4
225	6.00	1.6
250	6.67	1.7
275	7.33	1.9
300	8.00	2.1
325	8.67	2.3
350	9.33	2.4
375	10.0	2.6
400	10.7	2.8

The minimum flow rate was found to be around  $7.3\cdot 10^{-5} \text{ m}^3\cdot\text{m}^{-1}\cdot\text{s}^{-1}$ , which means that a minimum web speed of about  $275 \text{ m}\cdot\text{min}^{-1}$  is required to obtain a coating thickness of  $16 \text{ g}\cdot\text{m}^{-2}$ . This minimum web speed is relatively high compared to other bead coating techniques, which operate at speeds below  $200 \text{ m}\cdot\text{min}^{-1}$ . Up to about  $400 \text{ m}\cdot\text{min}^{-1}$  no visible air entrainment was observed.

In the second series the web speed was varied at a fixed value of the flow rate ( $1.0\cdot 10^{-4} \text{ m}^3\cdot\text{m}^{-1}\cdot\text{s}^{-1}$ ). At a web speed of  $78 \text{ m}\cdot\text{min}^{-1}$  the heel is stable but droplets come off the edge guides. At  $113 \text{ m}\cdot\text{min}^{-1}$  these droplets disappear, this situation persists up to a web speed of  $269 \text{ m}\cdot\text{min}^{-1}$  where visible air entrainment occurs. First a few small V-shaped pockets are formed in the heel. In the tip of such triangles the liquid does not merge but an empty streak is left on the roll. With increasing web speed a sawtooth profile is formed in the impingement zone; the position of the individual



triangles varies much more than at the lower speeds, were they almost remain fixed. At  $375 \text{ m}\cdot\text{min}^{-1}$  so many triangles form that they merge to one big hole, from which the fluid leaks away.

At  $375 \text{ m}\cdot\text{min}^{-1}$  the flow rate was now increased with increments of  $1.1\cdot 10^{-5} \text{ m}^3\cdot\text{m}^{-1}\cdot\text{s}^{-1}$  to  $1.7\cdot 10^{-4} \text{ m}^3\cdot\text{m}^{-1}\cdot\text{s}^{-1}$ . Now the V-shaped pockets gradually disappear and a heel with air entrainment is formed. Droplets, detached from the heel, ‘bounce’ behind the heel.

The line at a fixed value for the premetered flow rate,  $q$ , is termed meta-stable, because it intersects with the stable line obtained from the first series of experiments (see figure 8.7). Finding the complete coating window is subject of further study.

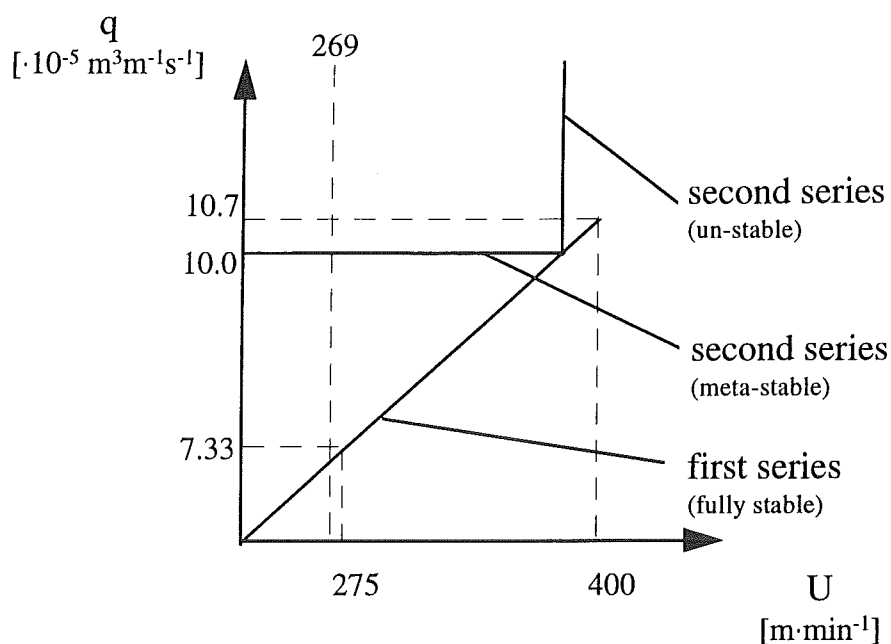


Figure 8.7: Examined part of the operating window.

### 8.3 Pilot Experiments

The next step is to verify qualitatively and quantitatively to what extent the data obtained from the off-line experiments agree with reality. Therefore pilot experiments were carried out on a half meter wide coater. Figure 8.8 shows a typical pilot coater used to simulate industrial conditions. In the curtain coater unit the substrate travels through a loop, in this way the substrate is turned. Without the loop, the coated web would touch the rolls and stick to them. After coating the web is passed through the dryer section, which is positioned above the coater.



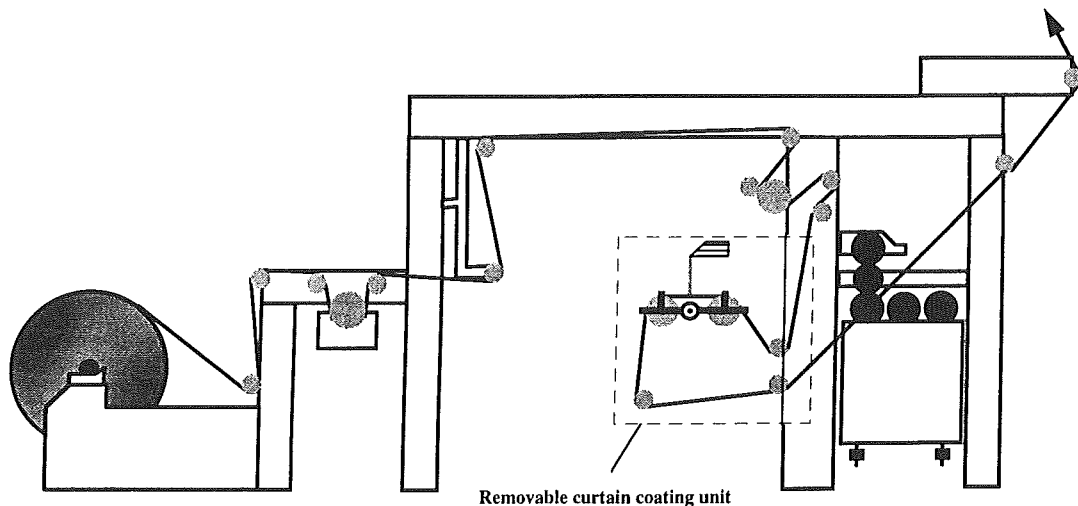


Figure 8.8: The pilot coater width build in curtain coater unit.

Two series of trials were carried out: the first in December 1996; the second in July 1997. In the first series the focus was on:

- start-up problems
- edge effects
- air entrainment

#### *Start-up problems*

For the curtain to form at start-up or after curtain breakup, a high liquid flow rate ( $1.6 \cdot 10^{-4} \text{ m}^3 \cdot \text{m}^{-1} \cdot \text{s}^{-1}$ ) is required, which is then reduced to the desired value. The capacity of the drying section, however, is not sufficient to dry this very thick coating. As a solution to this start-up problem, a so-called catch-pan is installed underneath the curtain. At start-up the web is brought up to speed and at the same time the curtain is formed; at the right speed the catch-pan is removed and the liquid coats the web. In case of breakup the catch-pan is used to prevent splashing of the liquid and to reestablish the curtain.

#### *Edge Effects*

Breakups of the curtain were mainly caused by the solid edge guides. To keep a stable curtain the solid edge guides had to be positioned inward; this reduces the overall coating width from 50 cm to about 43 cm. When using hollow edge guides the liquid does not wet the edge guide, instead the curtain is pinned to a slot.



### *Air Entrainment*

The trials started at a flow rate of  $7.3 \cdot 10^{-5} \text{ m}^3 \cdot \text{m}^{-1} \cdot \text{s}^{-1}$  and a web speed of  $230 \text{ m} \cdot \text{min}^{-1}$ . At these conditions there were problems in forming a stable curtain; the airwipe was able to sufficiently remove the airlayer from the surface of the web. At higher web speeds of about  $400 \text{ m} \cdot \text{min}^{-1}$  air was entrained visibly and the curtain was pulled, resulting in a bendout of about 2 - 3 cm. To overcome the problem of curtain bendout a thin wire was placed underneath the substrate at the point of curtain impingement. A voltage difference of 8 kV at a current of 1.2 mA was applied to this wire, which pinned the curtain to the substrate. The effect of this so-called electrostatic assist is most pronounced at low flow rates, where the curtain lacks momentum. The momentum flux of the curtain,  $I$ , is given as:

$$I = \rho q V$$

8.4

The assist was able to bend back the curtain for about 6 cm. The assist however was not able to prevent splashing of liquid at the sides near the edge guides. One of the reasons for this splashing is the alignment of the edge guides. For the tests in July a special positioning system was developed.

In the second series the emphasis of the experiments was on:

- better design of the airwipe
- studying the effect of the electrostatic assist

### *Better Design of the Airwipe*

The airwipe used for the experiments in December could not be placed onto the substrate without damaging the substrate surface. Therefore several materials were investigated and a polypropylene (PP) with plasticizer was found flexible enough not to damage the web. Thereby making experiments at  $400 \text{ m/min}$  as on the dynamic off-line equipment possible.

### *Electrostatic Assist*

The influence of electrostatic assist was studied at high flow rate and web speeds. Table 8.3 lists the conditions which were examined.

Table 8.3: Experimental conditions for the second trial series.

Electrostatic assist	8 kV	8 kV	0 kV	0 kV
Web speed (m/min)	350	400	350	400
Actual Coatwidth (m)	0.428	0.426	0.431	0.429
Flow rate (cc/min.m)	5714	6462	6387	5700

As expected coat weight measurements showed no significant difference between the four conditions. The next trials should be done at low flow rate.



## 8.4 Edge Guiding

Surface tension causes the liquid to neck-in in an attempt to reach the lowest state of internal energy. This effect is counteracted through the use of edge guides (figure 1.1). Two distinct types have been investigated: solid (figure 8.9) and hollow edge guides (figure 8.10).

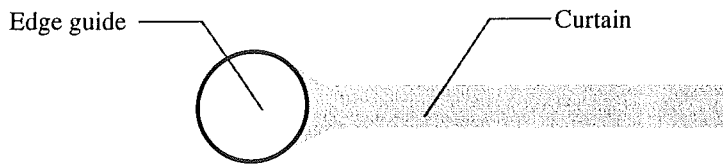


Figure 8.9: Attachment of the curtain to the solid edge guide (top view).

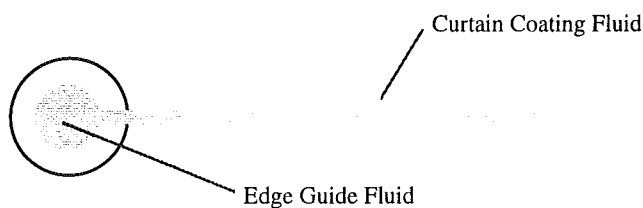


Figure 8.10: Attachment of the curtain to the hollow edge guide (top view).

During experiments it was observed that the hollow edge guides allow a much wider coating, 49 cm compared to the solid edge guides, 43 cm. There are two reasons for this: first the curtain is pinned to the slot in the hollow edge guide instead of wetting the entire edge guide. Second, the edge guide liquid works as a lubrication of the curtain, thereby reducing the velocity gradient near the edge.

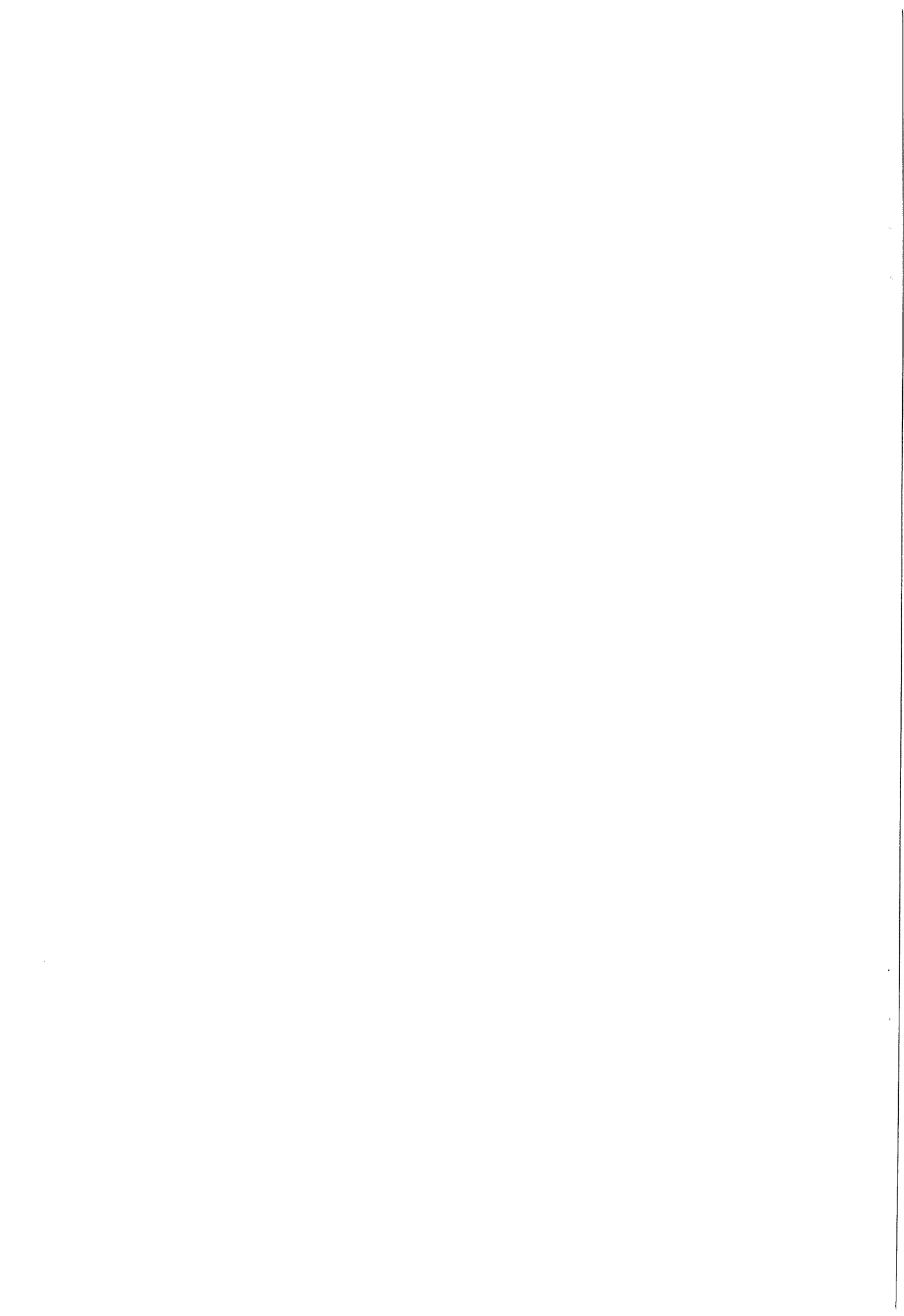
There are however some disadvantages with respect to plugging and the fact that the technique is patented. Therefore the experiments were done mostly with solid edge guides.

For the solid edge guides the type of material and the diameter were studied as well, a list is given in table 8.4.

Table 8.4: Different materials and diameter of the edge guide.

Brass	4 and 6 mm
Glass fibre	3, 4, 5 and 6 mm
Nylon	8 and 10 mm
PPMA	10 mm
Stainless steel	8 mm

The choice of material did not matter to much. The diameter should be chosen at about 3 mm.



## 9. Nomenclature

$\partial A$	the entire boundary of the computational domain	-
$\partial A_f$	all free-surface boundaries	-
$A$	computational domain	-
$c$	concentration	wt%
$C$	wavespeed of a disturbance	$m s^{-1}$
$c_T$	adjustable parameter in the Voinov-Tanner law	-
$h$	curtain height	m
$h$	Planck's constant	$kg m^2 s^{-1}$
$I$	momentum flux	$kg s^{-2}$
$k$	Boltzmann's constant	$J K^{-1}$
$K$	consistency	$kg m^{-1} s^{n-2}$
$L$	characteristic length scale	m
$l'$	relative wetting line position	-
$L_\delta$	distance where the boundary layer hits the front free surface of the curtain	m
$L_\sigma$	capillary length	m
$M_{ct}$	wet coat weight	$kg m^{-2}$
$n$	power-law index	-
$p$	pressure	Pa
$q$	flow rate per meter die width (premetered flow rate)	$m^3 m^{-1} s^{-1}$
$r_E$	slot enlargement	-
$r_H$	step height	-
$s$	arc length along the free surface	m
$T$	temperature	K
$t$	time	s
$U$	characteristic velocity	$m s^{-1}$
$U$	coating speed	$m s^{-1}$
$u$	speed of the contact line	$m s^{-1}$
$U'$	maximum air-entrainment speed attains	$m s^{-1}$
$u'$	overall velocity of wetting	$m s^{-1}$
$U''$	speed at the onset of air entrainment (very high flow rates)	$m s^{-1}$
$V$	curtain velocity	$m s^{-1}$
$V_0$	average velocity at the slot exit	$m s^{-1}$
$x$	distance measured from the contact line along the solid surface	m
$x^*$	contact line position	m
$x_{ffs}$	position of the front free surface	m
$Y$	vertical coordinate	m
$Y_0$	starting point below the slot of the free-fall parabola	m

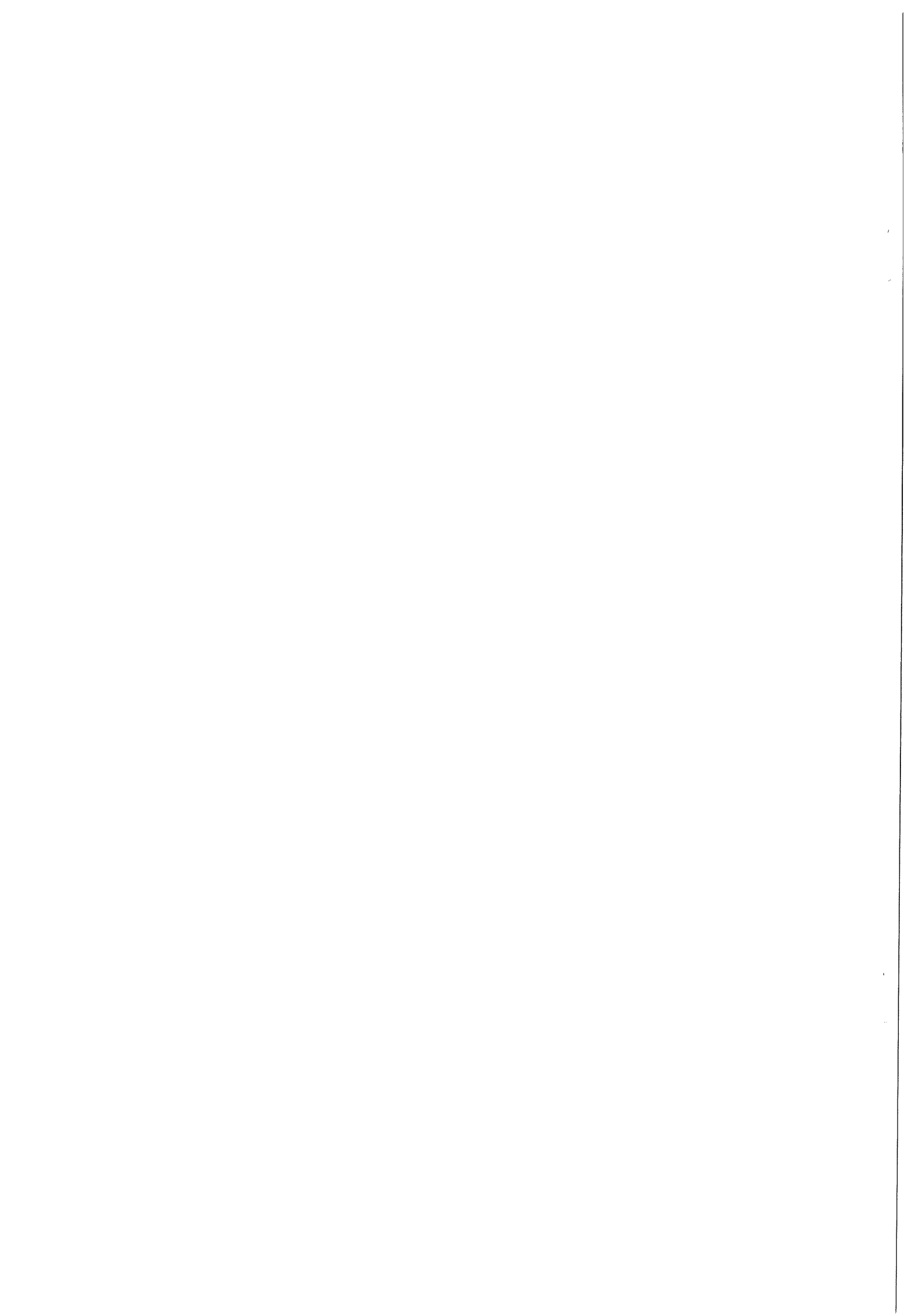


### *Tensors*

<b>D</b>	rate of deformation tensor	$s^{-1}$
<b>f</b>	unit vector in the direction of the gravitational force	-
<b>F<sub>net</sub></b>	net force on a body	N
<b>g</b>	gravitational acceleration	$m s^{-2}$
<b>I</b>	unit tensor	-
<b>L</b>	momentum of a body	$kg m s^{-1}$
<b>n<sub>i</sub></b>	outward unit normal of phase i to the interface	-
<b>n<sub>θ</sub></b>	unit normal to the visible free surface at the contact line	-
<b>n<sub>s</sub></b>	unit normal to the solid surface	-
<b>R<sup>C</sup></b>	weighted continuity residuals	-
<b>r<sub>i</sub></b>	residual traction	$kg m^{-1} s^{-2}$
<b>R<sup>K</sup></b>	weighted kinematic residuals	-
<b>R<sup>M</sup></b>	weighted momentum residuals	-
<b>R<sup>M</sup><sub>i,slip</sub></b>	contribution of a slip boundary condition to the momentum residual	-
<b>T</b>	total stress tensor	$N m^{-2}$
<b>t</b>	unit tangent to the interface	-
<b>τ</b>	stress tensor	$N m^{-2}$
<b>T<sub>σ</sub></b>	interfacial stress tensor	$kg s^{-2}$
<b>t<sub>s</sub></b>	unit tangent to the solid surface	-
<b>v</b>	velocity	$m s^{-1}$
<b>v<sub>c</sub></b>	velocity of the contact line	$m s^{-1}$
<b>v<sub>s</sub></b>	velocity of the solid boundary	$m s^{-1}$
<b>w<sub>i</sub></b>	mesh velocity	$m s^{-1}$
<b>x<sub>c</sub></b>	location of the apparent contact line	m
<b>y<sup>k</sup></b>	current estimate of the flow field	-

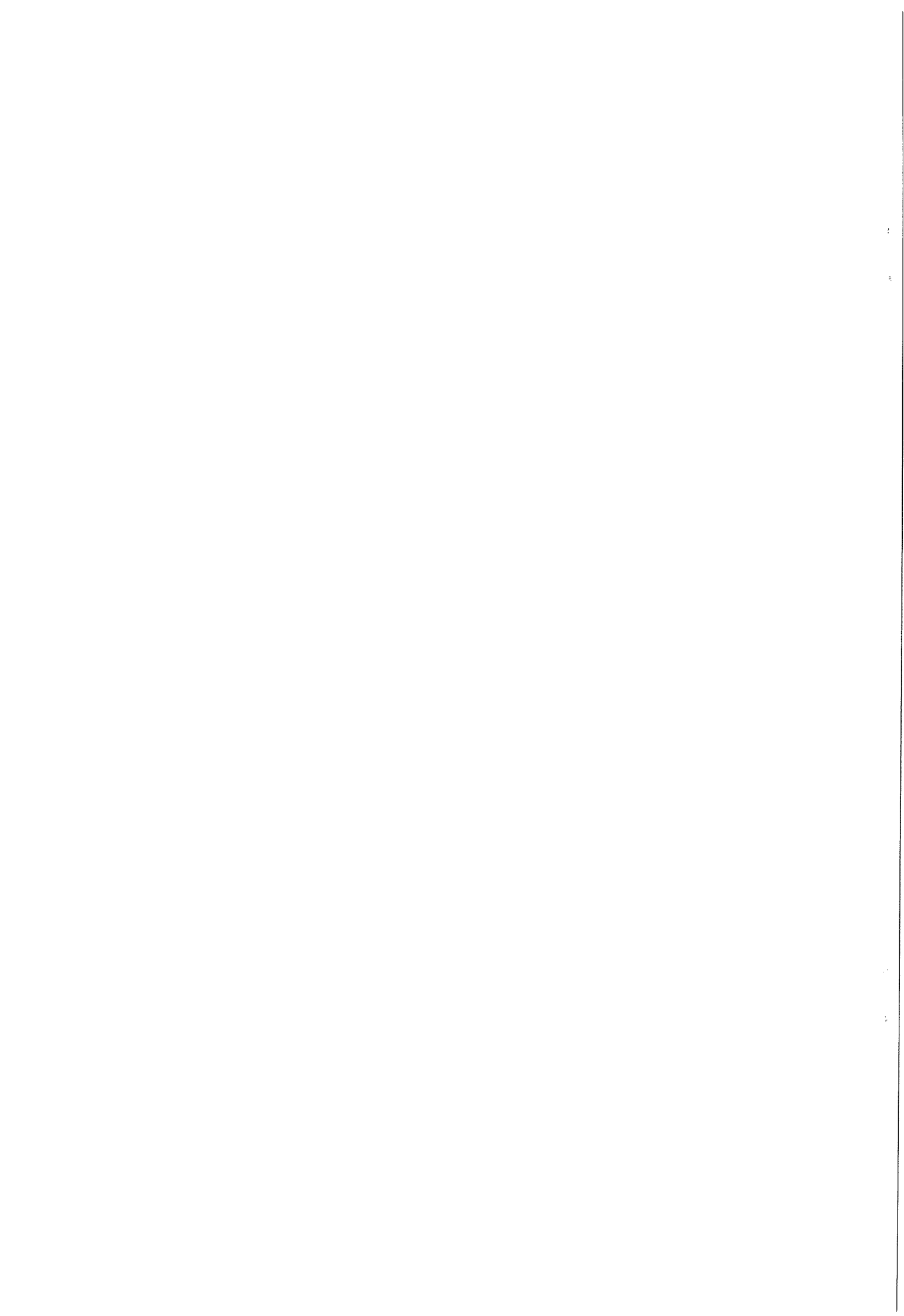
### *Dimensionless numbers*

<b>Ca</b>	Capillary number	-
<b>N<sub>p</sub></b>	property number	-
<b>Re</b>	Reynolds number	-
<b>Re<sub>L</sub><sup>crit</sup></b>	critical Reynolds number at the lower turning point	-
<b>Re<sub>S</sub><sup>crit</sup></b>	critical Reynolds number at which the separation angle no longer satisfies the Gibbs inequality condition	-
<b>Re<sub>U</sub><sup>crit</sup></b>	Reynolds number at the upper critical turning point	-
<b>St</b>	Stokes number	-
<b>We</b>	Weber number	-



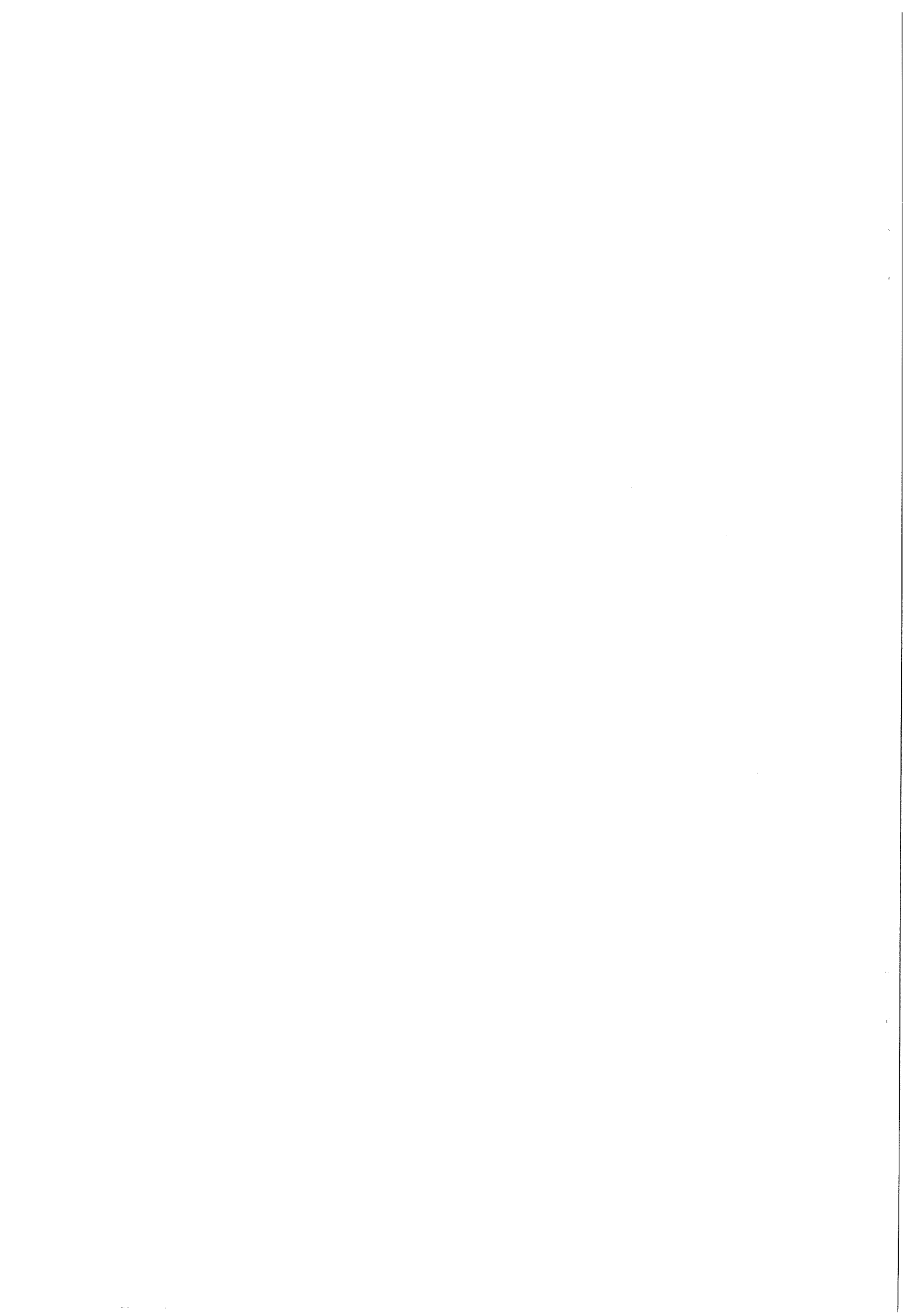
*Greek*

$\alpha$	angle of inclination of the die	°
$\alpha'$	angle of web inclination	°
$\beta$	slip coefficient	$\text{m}^2 \text{s kg}^{-1}$
$\delta_{\text{co}}$	final thickness of the coating	m
$\delta_{\text{cu}}$	ultimate thickness of the impinging curtain	m
$\delta_{\text{film}}$	final thickness of the film on the slide	m
$\delta_{\text{M}}$	thickness of the momentum boundary layer	m
$\delta_{\text{slot}}$	slot height of the die	m
$\delta_{\text{slot,E}}$	enlarged slot height of the die	m
$\Delta\tau$	(pseudo) time step	s
$\phi$	angle of projection of the gravity force	°
$\phi^i(\xi,\eta)$	Legendre polynomial basis function for velocity	-
$\phi^j(\xi,\eta)$	Legendre polynomial basis function for nodal position	-
$\gamma$	cut-back angle	°
$\Gamma$	pressure drop per meter length	$\text{kg m}^{-2} \text{s}^{-2}$
$\eta$	dynamic viscosity	$\text{kg m}^{-1} \text{s}^{-1}$
$\eta$	local coordinate for iso-parametric mapping	-
$\eta$	dimensionless co-ordinate in the similarity velocity profile	-
$\varphi$	the angle between the normal to the wetting line and the overall direction of wetting	°
$\varphi(\eta)$	similarity velocity profile	-
$\kappa_{\text{s}}$	the frequency of molecular displacements at equilibrium when retarded only by surface forces	$\text{s}^{-1}$
$\lambda$	average distance between two adsorption sites	m
$\nu$	kinematic viscosity	$\text{m}^2 \text{s}^{-1}$
$\theta$	apparent contact angle	°
$\theta'$	Mach angle	°
$\theta_0$	static contact angle	°
$\theta_{\text{C}}$	the predicted apparent contact angle	°
$\theta_{\text{S}}$	static separation angle	°
$\rho$	density	$\text{kg m}^{-3}$
$\sigma$	surface tension of a liquid against air	$\text{kg s}^{-2}$
$\nu_i$	molecular flow volume of phase i	$\text{m}^3$
$\omega$	velocity ratio: $V/U \sin(\alpha')$	-
$\xi$	local coordinate for iso-parametric mapping	-
$\psi^k(\xi,\eta)$	Legendre polynomial basis function for pressure	-



## 10. References

- Ade, F., *Gleitflächenbeschichtungsvorrichtung*, Deutsche Offenlegungsschrift, 25 21 955, 1976.
- Bird, R.B., Stewart, W.E. and Lightfoot, E.N., *Transport Phenomena*, John Wiley & Sons, New York, 1960, p. 75 and 79.
- Blake, T.D., Clarke, A. and Ruschak, K.J., Hydrodynamic Assist of Dynamic Wetting, *AIChE J.*, 1994, 40 (2), 229-242.
- Blake, T.D., Dynamic contact angles and wetting kinetics, in 'Wettability', (Ed. J. Berg), Marcel Dekker, New York, 1993.
- Brown, D.R., A study of the behaviour of a thin sheet of moving liquid, *J. Fluid Mech.*, 1961, **10**, 297-305.
- Chang, P.W., Patten, T.W. and Finlayson, B.A., Collocation and Galerkin finite element methods for viscoelastic fluid flow - II. Die swell problems with a free surface, *Comp. Fluids*, **7**, 285.
- Cherry, B.W. and Holmes, C.M., Kinetics of wetting of surfaces by polymers, *J. Colloid Interface Sci.*, 1969, **29**, 174.
- Cox, R.G., *J. Fluid Mech.*, 1986, **168**, 169.
- Do, D.V. and Christodoulou, K.N., Multilayer curtain coating flows: stability and sensitivity to small disturbances, paper read at AIChE Spring National Meeting, New Orleans, LA., 1992.
- Durbin, P.A., *J. Fluid Mech.*, 1988, **197**, 157.
- Finnicum, D.S., Weinstein, S.J. and Ruschak, K.J., The effect of applied pressure on the shape of a two-dimensional liquid curtain falling under the influence of gravity, *J. Fluid Mech.*, 1993, **255**, 647-665.
- Gibbs, J.W., *The Scientific Papers of J. Willard Gibbs Vol. I, Thermodynamics*, Longmans Green & Co., New York, 1906; Reprint, New York, 1961.
- Glasstone, S., Laidler, K.J. and Eyring, H.J., *The Theory of Rate Processes*, McGraw-Hill, New York, 1941.
- Grald, E.W.G., private communications on free-surface simulations, 1997.
- Greiller, J.F., *Method for Making Photographic Elements*, U.S. Patent 3,632,374, 1972.
- Gresho, P.M., Some current CFD issues relevant to the incompressible Navier-Stokes equations, *Comput. Meth. Appl. Mech. Eng.*, 1991, **87**, 201-252.
- Gutoff, E.B. and Kendrick, C.E., *AIChE J.*, 1982, **28**, 459.
- Hansen, R.J. and Toong, T.Y., Dynamic contact angle and its relationship to forces of hydrodynamic origin, *J. Colloid Interface Sci.*, 1971, **37**, 196-207.
- Ho, L.-W. and Patera, A.T., A Legendre spectral element method for simulation of unsteady incompressible free-surface flows, *Comput. Meth. Appl. Mech. Eng.*, 1990, **80**, 355-366.



- Hughes, D.J., *Method for Simultaneously Applying a Plurality of Coated Layers by Forming a Stable Multilayer Free-Falling Vertical Curtain*, U.S. Patent 3,508,947, 1970.
- Huh, C. and Mason, S.G., *J. Fluid Mech.*, 1977, **81**, 401.
- Huh, C. and Scriven, L.E., Hydrodynamic model of steady movement of a solid/liquid/fluid contact line, *J. Coll. Interf. Sci.*, 1971, **35**, 85.
- Hunter, J.H., *Foundations of Colloid Science*, Clarendon Press, Oxford, 1987, p. 309
- Isaacson, E. and Keller, H.B., *Analysis of Numerical Methods*, Wiley, New York, 1966.
- Kinzelmann, J., *Method and Apparatus for Flow Coating Objects*, U.S. Patent 3,205,089, 1965.
- Kistler, S.F. and Scriven, L.E., Coating flow theory by finite-element and asymptotic analysis of the Navier-Stokes system, *Int. J. Numer. Meth. Fluids*, 1984, **4**, 207-229.
- Kistler, S.F. and Scriven, L.E., Coating flow theory, *Int. J. Numer. Meth. Fluids*, 1983.
- Kistler, S.F., in '*Analysis of Polymer Processing*', (Eds: J.R.A. Pearson and S.M. Kistler), S.F., *The Fluid Mechanics of Curtain Coating and Related Viscous Free Surface Flows with Contact Lines*, Ph.D. Thesis, University of Minnesota, 1984, p. 206-217 and p. 348-349.
- Lowndes, J., The numerical simulation of the steady movement of a fluid meniscus in a capillary tube, *J. Fluid Mech.*, 1980, **101**, 631.
- Mohanty, K.K., *Fluid in Porous Media: Two-Phase Distribution and Flow*, Ph.D. Thesis, University of Minnesota, 1981.
- Navier, C.L.M.H., Mémoire sur les lois du mouvement des fluides, *Mém. Acad. R. Sci. Inst. Fr.*, **6**, 389.
- Neogi, P. and Miller, C.A., *J. Coll. Inter. Sci.*, 1982, **86**, 525.
- Ogawa, S., and Scriven, L.E., An analysis of curtain coating flow, *AIChE J.*, 1994.
- Padday, J.F., *Multiple Coating Apparatus*, U.S. Patent 3,005,440, 1961.
- Palmer, H.J., in '*Liquid Film Coating*', (Eds.: S.F. Kistler and P.M. Schweizer), Chapman & Hall, London, 1997, p. 34 and p.37.
- Pearson, J.R.A., in '*Analysis of Polymer Processing*', (Eds: J.R.A. Pearson and S.M. Raux), Raux, R., Appareil de Revêtement par Rideau Liquide, Brevet d'Invention 833.851, Royaume de Belgique, 1976.
- Reiner, M., The teapot effect, *Physics Today*, 1956, **9**, 16.
- Richardson), Applied Science Publishers, London, 1983, p.6 and p. 261-269.
- Ruschak, K.J., A method for incorporating free boundaries with surface tension in finite element fluid flow simulators, *Int. J. Numer. Meth. Eng.*, 1980, **15**, 639-648.
- Schweizer, P.M., Optimization of coating processes in '*Liquid Film Coating*', (Eds.: S.F. Kistler and P.M. Schweizer), Chapman & Hall, London, 1997, p. 749.



- 
- Silliman, W.J. and Scriven, L.E., Separating flow near a static contact line: slip at a wall and shape of a free surface, *J. Comp. Phys.*, 1980, **34**, 287.
- Stokes, G.C., On the effect of the internal friction of fluids on the motion of pendulums, *Trans. Cambridge Phil. Soc.*, **9**, 8.
- Tanner, L.H., The spreading of silicone oil drops on horizontal surfaces, *J. Phys. D: Appl.*, 1979, **12**, 1473-1484.
- Thompson, J.F., Warsi, U.A. and Mastin, C.W., Boundary-fitted coordinate systems for numerical solution of partial differential equations -a review, *J. Comput. Phys.*, 1982, **47**, 1-108.
- Voinov, O.V., Hydrodynamics of wetting, *Fluid Dynamics*, 1976, **11**, 714-721.
- Weinstein, S.J., in '*Liquid Film Coating*', (Eds.: S.F. Kistler and P.M. Schweizer), Chapman & Hall, London, 1997, p. 20.
- Willis, S., The development of Poiseuille flow, *J. Fluid Mech.*, 1969, **52**, 639.
- Zvan, G.R., Douglas, L.J., Kistler, S.F., AIChE Spring National Meeting, New Orleans, LA, 1992.

